Exploring Charge Transport Mechanisms and Conduction Limits in Rubrene Single Crystals

A DISSERTATION
SUBMITTED TO THE FACULTY OF
UNIVERSITY OF MINNESOTA
BY

Xinglong Ren

IN PARTIAL FULFILLMENT OF THE REQUIREMENTS
FOR THE DEGREE OF
DOCTOR OF PHILOSOPHY

Advisor: C. Daniel Frisbie

December, 2018

Acknowledgement

First, I would like to thank my advisor Prof. Dan Frisbie for his continuous guidance and support during my PhD research. From Dan, I learned not only about how to understand the physical pictures behind our experimental results, but also about how to present the scientific work in a compact, clear, and effective way. Dan is a very knowledgeable person and has broad research interests. As a member in the Frisbie group, I have the chance to get exposed to different fields in addition to my own research areas, from very fundamental charge transport processes in molecular junctions to application-oriented printed electronics. It is a great honor for me to have Dan as my advisor. Working with him in the last five years actually shaped my taste of science.

I also would like to thank all my collaborators (at Minnesota and outside Minnesota) who have helped me to finish this thesis: Prof. Chris Leighton, for serving as my "unofficial" co-advisor and for his significant contribution to interpreting the experimental data when I started to perform low temperature transport measurements; Jeff Walter and Koustav Ganguly, for their help in the Hall effect measurements and resistance–temperature measurements; Prof. Bharat Jalan, for serving on my committee and for giving me access to his lab; Prof. Paul Ruden, for serving on my committee and for his previous work on developing charge transport models in rubrene; Prof. Chris Douglas, Matt Bruzek, Katie McGarry, and Zhuoran Zhang, for synthesizing and providing the source materials; Prof. James Johns and Aaron Schulzetenberg, for performing the low-wavenumber Raman spectroscopy; Prof. Alberto Salleo and David Hanifi (Stanford), for analyzing the band tail states of my crystals by photothermal deflection spectroscopy; Prof Alessandro Troisi (Liverpool) and Dr. Simone Fratini (CNRS Grenoble), for developing the dynamic disorder model and providing theoretical support for our isotope effect experiments.

I am indebted to my lab mates for their direct and indirect contributions. Wei Xie and Elliot Schmidt are the predecessors and they taught me almost everything about organic crystals and electrolyte gating when I started as a first-year graduate student. Yanfei Wu, Chang-Hyun Kim, and Boxin Tang helped me a lot by sharing their expertise in various materials characterization techniques. Abel Demissie, Scott White, Motao Cao, Fazel Zare Bidoky, Tao He, and Zuoti Xie deserve special credit for their technical help whenever it was needed. Our lab safety officers Chris Smith, Davood Taherinia, Krystopher Jochem, and Yan Wang made great efforts in lab safety. I also would like to express my gratitude to all the previous and current Frisbie group members (including but not limited to): Ankit Mahajan, Vina Faramarzi, Stuart Oram, Hong Chul Moon, Geoff Rojas, Woo Jin Hyun, Jingjing Qin, Donghoon Song, Mathew Thomas, and Quyen Van Nguyen.

I acknowledge the help from the scientists/engineers in the Minnesota Nano Center and the Characterization Facility, and the help from the staff in the Department of Chemical Engineering and Materials Science. Prof. Russ Holmes also helped me a lot and deserves special thanks for his recommendation.

Last but not least, thank all my friends, especially my long-term roommates Yutao Tao and Hongshi Li, for making my stay at Minnesota memorable. It is so enjoyable to meet and communicate with talented people like you.

Abstract

This dissertation focuses on fundamental research on the frontier of organic electronics, aiming to find answers to some long-standing puzzles related to electrical conduction in the benchmark single crystal organic semiconductor known as rubrene. Emphasis is on determining the intrinsic charge transport mechanism in rubrene single crystals, as the crystalline order in these samples facilitates better understanding of fundamental structure-property relationships. To further explore the conduction limits in rubrene single crystals, high densities of charge carriers are injected using the liquid-gating technique, and intriguing and unusual physical phenomena, such as negative transconductance and cooling-rate-dependent charge transport, have been observed.

Chapters 1-4 summarize the background information for this dissertation. Chapter 5 focuses on the isotope effect on field-effect mobility in rubrene single crystals to determine the best theoretical model for charge transport in high mobility organic semiconductors. Chapter 6 explains why very few organic semiconductors exhibit intrinsic, band-like transport by revealing correlated electronic and structural disorder using scanning Kelvin probe microscopy. Chapter 7 focuses on the use of dipolar liquid to accumulate charge at rubrene crystal surfaces while maintaining the high mobility. Chapter 8 explores charge transport phenomena near the maximum conductivity of rubrene single crystals and proposes the limiting factors for charge transport. Overall, this work helps to better understand intrinsic charge transport mechanisms and conduction limits in high mobility organic semiconductors.

Table of Contents

List of Tables

List of Figures

Chapter 1 Introduction

1.1 Motivation for thesis

In the past few decades, silicon-based conventional semiconductor devices have revolutionized the world, becoming the foundation of the hundreds-of-billion-dollar modern electronics industry. What makes semiconductors unique is that the charge carrier densities in semiconductors can be tuned easily by chemical doping or by application of an external electric field. Changes in charge density correspond to changes in the conductivity of the material, which can be controlled over a wide range, from insulating to conducting. This property allows for creation of a circuit component called a transistor, which can act as an “OFF” or “ON” switch when the semiconductor is made insulating or conducting, respectively. Therefore, basic functions required in electrical circuits, such as switching, can be achieved. Despite the great technological success, silicon-based electronics is not omnipotent. Many applications require low-cost large-area fabrication of electronic devices and circuits, and silicon is not the best choice in those cases.

Compared with their inorganic counterparts, organic semiconductors, which are solids consisting of carbon-based molecules, are relatively new. The ground-breaking achievements in the area of electrical conduction in organic solids lead to the Nobel Prize in Chemistry in 2000.[1] Due to comparatively lower mobility (the key parameter describing how fast the charge carriers can move in an electric field) than crystalline inorganic semiconductors, organics cannot currently compete in applications requiring high switching speeds such as processor chips. Organic semiconductors do, however, have unique advantages over inorganic semiconductors including solution-processability,

mechanical flexibility, and multi-colored electroluminescence, resulting in the commercial success of organic-based products such as organic light-emitting diode displays.[2–4]

Despite progress in practical device-oriented applications, there is still much we do not know about the nature of electrical conduction in organic semiconductors (i.e., how charge transport happens). The interaction between organic molecules (weak van der Waals bond) is fundamentally different from the counterpart in inorganic semiconductors (strong covalent bond), which leads to lower charge carrier mobility and different conduction mechanisms. As a result, most of the theories for inorganic semiconductors are no longer valid for organics. What makes this situation even more difficult is that current commercial products based on organic semiconductors usually use an amorphous or polycrystalline form of the material rather than the highly ordered, near-perfect single crystalline form. Amorphous and polycrystalline materials suffer from a huge amount of structural disorder. These imperfections not only lead to low carrier mobility but also make it difficult to study the intrinsic electronic properties; therefore, a better platform is needed.

Thanks to their high purity and ordered structure, single crystals of organic small molecules are ideal to investigate intrinsic properties of organic semiconductors.[5–7] Many "hidden" physical phenomena in organic semiconductors can only be observed in crystals. For instance, single crystals of rubrene, the benchmark organic semiconductor, have a room temperature mobility over 10 $cm^2V^{-1}s^{-1}$, which is significantly larger than in thin films (< 0.01 $cm^2V^{-1}s^{-1}$) and even higher than the mobility of widely used amorphous silicon (~1 $cm^2V^{-1}s^{-1}$).[8] Other physical phenomena, such as the Hall effect, which was thought to only exist in inorganic semiconductors with very high mobility, have also been observed in

rubrene crystals.[9] However, challenges still remain in unifying intrinsic charge transport mechanism for organic semiconductors from experimental and theoretical perspectives.[10]

In addition to the intrinsic charge transport mechanism, another significant difference between inorganic and organic semiconductors is their dielectric constant. Organic semiconductors usually have small dielectric constant, which means the electric field decays much slower over distance. That is, the electrostatic interaction in organic semiconductors is more long-range compared with the interaction in inorganic semiconductors. One of the most well-known phenomena resulting from this effect is the formation of excitons in organic photovoltaics due to the strong binding between photogenerated electrons and holes. The small dielectric constants in organic semiconductors also affect charge transport significantly, especially when charge transport occurs at the surfaces/interfaces. Due to the weakly screened electric field, the charge transport can be limited by external electronic disorder from the surroundings, so even a perfect organic single crystal may not exhibit intrinsic properties. For example, the field-effect mobility of rubrene single crystals is significantly reduced when some oxides, such as Ta_2O_5, are used as the dielectric layer.[11] The influence of external electronic disorder is more noticeable when the charge density is high, and it has to be taken into consideration when doing charge transport experiments.

In this thesis, two fundamental aspects of charge transport in organic semiconductors are explored. First, we have carried out electrical and structural characterization on rubrene-based single crystals in order to better understand the intrinsic charge transport mechanism in organic semiconductors. We have found that the best model describing charge transport in high mobility organic semiconductors is neither the band transport

model (the most widely used one for charge transport in inorganic semiconductors) nor hopping-based model (mostly used for charge transport in low mobility systems), but is a recently developed, intermediate one called dynamic disorder (or transient localization) model. We have also gained some insights in explaining why many organic crystals with promising electronic structures do not perform well in transport experiments. Second, we have utilized liquid dielectrics such as dipolar liquids and ionic liquids to inject more charge in organic semiconductors and study new phenomena in the high charge density regime. Anomalous phenomena including field-induced memory effect and cooling-rate-dependent charge transport, which do not exist in regular devices, have been observed in rubrene crystals with such liquid dielectrics. Our observations support that charge transport near the organic/dielectric interface is greatly affected by the dielectric environment. All these works in this thesis will not only provide an important benchmark for ongoing efforts to study charge transport in organic semiconductors, but also open the doors to new opportunities for exploring novel field-effect transport phenomena in organic crystals.

1.2 Overview of thesis

Chapter 2 introduces the basic aspects of organic semiconductors and field-effect transistors (FETs). Both charge transport physics and device fabrication/characterization are included. Special focus is on single crystal organic field-effect transistors (OFETs) and charge transport studies related to them, since single crystal OFETs are believed to be a good platform to study intrinsic transport properties.

Chapter 3 introduces the basic aspects of electrolyte gating. This chapter discusses working principles of electrolyte gating, electrolyte materials, device characterization, and recent charge transport studies in electrolyte-gated transistors (EGTs).

Chapter 4 summarizes the experimental methods used in this thesis, including growth of organic crystals, structural characterization of organic crystals, device fabrication, and different electrical characterization techniques.

Chapter 5 summarizes work done to better understand intrinsic charge transport in the benchmark organic semiconductor, rubrene single crystals, by studying the isotope effect on field-effect mobility. An isotopically substituted rubrene molecule, ^{13}C-rubrene (all the carbon atoms are ^{13}C), was synthesized and characterized. The mobility of transistors based on ^{13}C-rubrene crystals is 13% lower than the mobility of native rubrene crystals. The observed negative isotope effect on mobility suggests that dynamic disorder model is the best model describing charge transport in high mobility organic semiconductors. This work has been published as *X. Ren, M. J. Bruzek, D. A. Hanifi, A. Schulzetenberg, Y. Wu, C. Kim, Z. Zhang, J. E. Johns, A. Salleo, S. Fratini, A. Troisi, C. J. Douglas, and C. D. Frisbie, "Negative Isotope Effect on Field-Effect Hole Transport in Fully Substituted ^{13}C-Rubrene", Advanced Electronic Materials, 2017, 3, 1700018*.

Chapter 6 summarizes work done to explain why many organic crystals with promising electronic structures do not perform as well as expected in transport experiments. A combination of different characterization techniques including scanning Kelvin probe microscopy, in-plane X-ray diffraction and chemical etching reveal that hidden electronic disorder exists in many organic crystals. Such electronic disorder is correlated with planar defects that are not detectable by commonly employed polarized light microscopy or standard out-of-plane X-ray diffraction. This work has been published as *Y. Wu, X. Ren, K. A. McGarry, M. J. Bruzek, C. J. Douglas, and C. D. Frisbie, "Scanning Kelvin Probe*

Microscopy Reveals Planar Defects Are Sources of Electronic Disorder in Organic Semiconductor Crystals", Advanced Electronic Materials, 2017, 3, 1700117.

Chapter 7 summarizes work done to investigate charge transport in rubrene crystals gated with a dipolar liquid called perfluoropolyether (PFPE). In particular, the influence of dipoles in PFPE on the charge carrier accumulation and transport at the rubrene/PFPE interface is explored. Large hysteresis in transistor transfer curves and peaks in the gate displacement current curves are observed and interpreted in terms of the dipolar response of PFPE to the gate electric field. This work has been published as *X. Ren, E. Schmidt, J. Walter, K. Ganguly, C. Leighton, and C. D. Frisbie, "Rubrene Single-Crystal Transistors with Perfluoropolyether Liquid Dielectric: Exploiting Free Dipoles to Induce Charge Carriers at Organic Surfaces", The Journal of Physical Chemistry C, 2017, 121, 6540*.

Chapter 8 summarizes work done to explore the conduction limit of electrolyte-gated rubrene crystals by performing detailed wide-range resistance−temperature measurements at multiple gate voltages. In the anomalous negative transconductance regime where the device becomes more insulating with higher charge density, distinctly cooling-rate-dependent transport is detected for the first time. Two possible sources of electronic disorder at the rubrene/electrolyte interface are proposed: (1) cooling-rate-dependent structural order in the ionic liquid and (2) the intriguing possibility of a gate-induced glassy short-range charge-ordered state in rubrene. This work has been published as *X. Ren, C. D. Frisbie, and C. Leighton, "Anomalous Cooling-Rate-Dependent Charge Transport in Electrolyte-Gated Rubrene Crystals", The Journal of Physical Chemistry Letters, 2018, 9, 4828*.

Chapter 9 proposes potential directions for future research based on the above findings.

Chapter 2 Organic Semiconductors and Organic Field-Effect Transistors

Organic semiconductors are conjugated small molecules or polymers with delocalized π-orbitals. In the solid state, these molecules are bonded together by weak van der Waals forces, which leads to their different mechanical, optical and electronic properties than inorganic semiconductors. Features of organic semiconductors, such as weak intermolecular electronic coupling and strong charge-phonon interaction, significantly affect charge transport physics in organic semiconductors. This chapter will focus on basic aspects of charge transport in organic materials, the techniques for charge transport study, and the benchmark organic semiconductor materials.

2.1 Charge transport in organic semiconductors

2.1.1 Delocalized molecular orbitals and intermolecular bonding

Organic semiconductors are made of individual carbon-based conjugated molecules. Those conjugated molecules, usually showing sp^2 hybridization, have regions of linearly overlapped sp^2 orbitals, which form the strong σ bonds that hold the neighboring atoms together. The superposition of the remaining p_z orbitals leads to the formation of delocalized π bonds over the entire molecule, which makes intramolecular charge transport feasible. Benzene, which has a 6-atom carbon ring, is probably the most famous conjugated molecule. **Figure 2.1a** shows the localized σ bonds (left), and delocalized π orbitals (right) of a benzene molecule. The delocalized orbitals extend all the way round the benzene ring and the π electrons are shared by all the 6 carbon atoms within the molecule.

Based on the linear combination of atomic orbitals (LCAO) theory, the molecular energy levels of the bonding state and anti-bonding state can be calculated. The bonding state is energetically favored and serves as the ground state. In organic molecules, the bonding and anti-bonding states correspond to the highest occupied molecular orbital (HOMO) and lowest unoccupied molecular orbital (LUMO), respectively. The energy difference between HOMO and LUMO is called the band gap, which is usually in the range of 2-3 eV for organic semiconductors. In real organic semiconductors where numbers of molecules are bonded together, however, the energy levels become different than those in an isolated molecule. When two molecules are bonded together, the HOMO and LUMO levels will split due to the intermolecular interaction; when the number of molecules increases, more energy levels are split and the energy difference between nearby levels becomes smaller, and finally the HOMO and LUMO bands with continuous energy levels are created (**Figure 2.1b**).

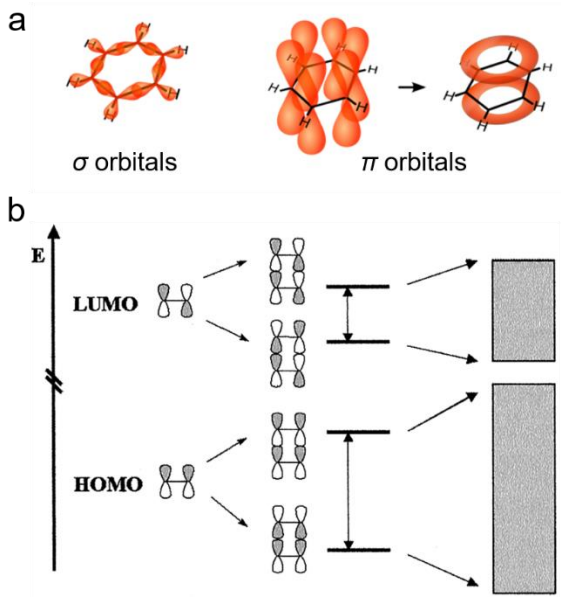

Figure 2.1 (a) Schematics of σ and π orbitals in a benzene molecule.[12] (b) Formation of HOMO and LUMO levels.[13]

2.1.2 Charge transfer and charge-phonon interaction

In addition to charge delocalization at the molecular level, another essential process for charge transport in organic semiconductors is intermolecular charge transfer, which is achieved by the overlap of neighboring π orbitals and the formation of the HOMO and LUMO bands. Generally speaking, the rate of charge transfer is mostly determined by the width of the HOMO and LUMO bands. A larger bandwidth represents more charge delocalization. Covalently bonded inorganic semiconductors such as Si have bandwidths on the order of 10 eV, while van der Waals bonded organic semiconductors usually have bandwidths smaller than 1 eV. The small bandwidth is one of the major factors that leads to the relatively low carrier mobility in organic semiconductors.

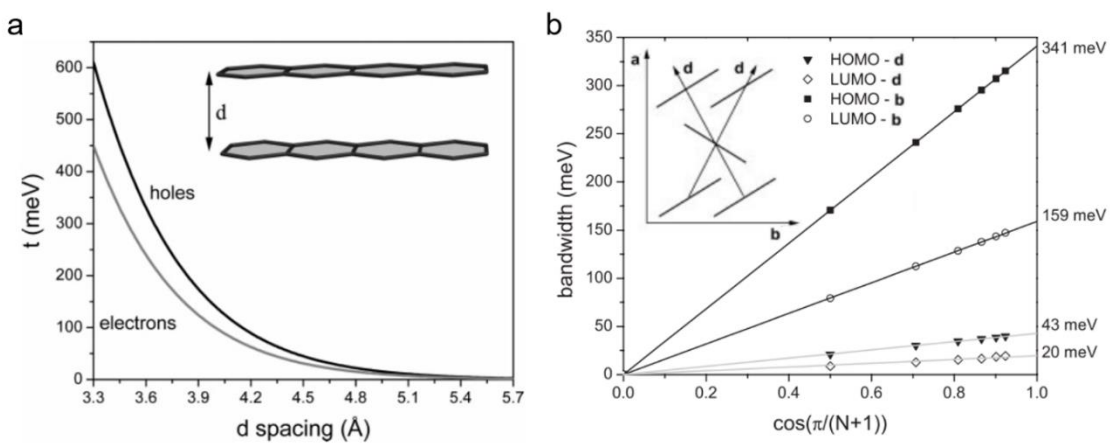

Figure 2.2 (a) Transfer integrals of two tetracene molecules as a function of intermolecular spacing.[10] (b) Transfer integrals of rubrene crystals along different crystallographic directions.[14]

A key parameter describing the degree of intermolecular electronic coupling is the intermolecular transfer integral (t), which is proportional to the bandwidth. Microscopically, the magnitude of transfer integral is determined by the degree of π-π orbital overlap. It is already known that the transfer integral decreases with increasing π-stacking distance (**Figure 2.2a**).[10] Therefore, smaller π-stacking distances are preferred

when designing high mobility organic semiconductors. The transfer integral difference along different crystallographic directions is also the main origin of charge transport anisotropy in organic semiconductors. For example, due to the anisotropic crystal structure of rubrene, within the π-stacking plane, the transfer integral along the *b*-axis is the largest and hence highest mobility is observed along the *b*-axis (**Figure 2.2b**).[14]

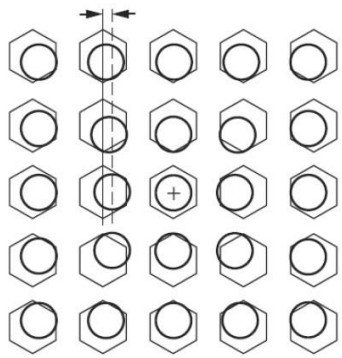

Figure 2.3 Formation of a polaron caused by introducing a positive charge into the lattice.[15]

A second important parameter for charge transport is called the reorganization energy (λ), which describes the strength of charge-phonon interaction. In organic semiconductors, the charge-phonon interaction usually involves the formation of a quasiparticle called a polaron.[16] Polarons form when an extra charge is introduced into the lattice and the charge polarizes the electron cloud on the surrounding molecules (**Figure 2.3**). A lattice distortion is created due to the attraction between the charge and the polarized surroundings, and the polarization travels together with the charge.[16–20] The timescale of polarization is related to the frequency of lattice vibration, and is on the order of 10^{-14} s. If this characteristic timescale is longer than the charge residence time (the average time that a charge stays on a molecule), the movement of the charge is fast enough that the influence of lattice polarization can be ignored; if it is comparable to or shorter than the charge residence time,

the molecules have long enough time to relax to new equilibrium positions and the polaron has long enough time to form. Once the polaron is formed, the energy levels of the charged molecule become different from those of a neutral molecule. For inorganic semiconductors, due to the high mobility, the charge residency time is often much smaller than the time required for polaron formation. For organic semiconductors with relatively low mobility, however, the influence of polarons on charge transport cannot be ignored.

The most famous theory for intermolecular charge transfer is probably the semiclassical Marcus theory.[21,22] In this theory, the charge transfer rate k_{ET}, is expressed as:

$$k_{ET} = \frac{4\pi^2}{h}\frac{t^2}{\sqrt{4\pi\lambda k_B T}}\exp\left(-\frac{\lambda}{4k_B T}\right) \tag{2.1}$$

Where h and k_B are the Planck and Boltzmann constants, and T is the temperature. Based on Equation (2.1), it is clear that to achieve faster charge transfer, larger t (larger degree of charge delocalization) and smaller λ (weaker charge-phonon interaction) are required.

2.1.3 Band transport and hopping transport

The two most commonly used models for charge transport in semiconductors are band transport and hopping transport. In solid state physics, band transport has been well established in highly crystalline inorganic semiconductors exhibiting long range periodic potentials such as Si or GaAs. In this model, the charge carriers are treated as delocalized wavefunctions propagating in the bands and charge transport is forbidden in the band gap. The simplest physical picture describing band transport is the classical Drude model, in which the charge moves under an applied electric field and is scattered elastically due to the existence of impurity atoms and lattice vibrations (**Figure 2.4a**). The speed of the charge travelling through the material scales linearly with the applied electric field (E), but

also depends on how often the scattering occurs. The carrier's drift velocity (v) can be written as $v = \mu E$, where μ is called carrier mobility. Mobility is the key parameter describing how fast a charge can move and influencing the actual device performance. In the Drude model, it is expressed as $\mu = e\tau/m^*$, where e is the elementary charge, τ is the average time between scattering, and m^* is the effective mass of the charge carrier.

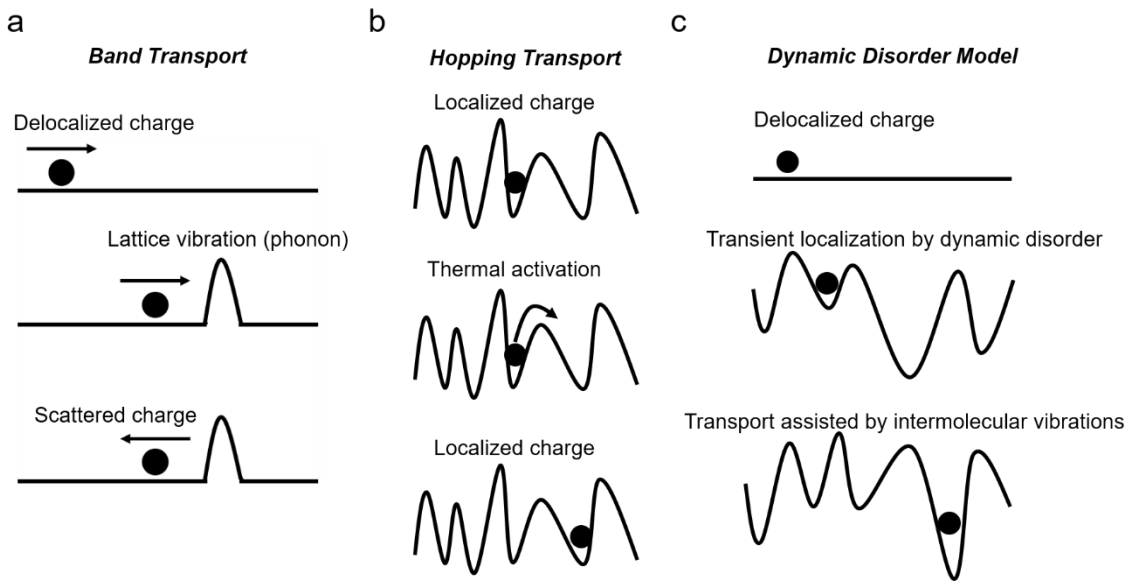

Figure 2.4 Schematics for (a) band transport, (b) hopping transport, and (c) dynamic disorder model. Note that the potential profile in (c) is not static.

The temperature dependence of mobility can provide valuable information about the nature of transport. In band transport, mobility decreases with increasing temperature as $\mu \propto T^{-n}$, because the charge-phonon interaction is stronger at higher temperature and therefore more scattering events occur. The temperature exponent n is a positive number, but the value of n depends on the type of scattering event. For example, acoustic phonon scattering gives $n = 1.5$. In addition, different combinations of scattering events can exist in different materials, so n is also material-dependent.

Different from the band transport model, the hopping transport model depicts charge transport through a series of localized electronic states, which is often the case for amorphous materials and for most organic semiconductors where the intermolecular bonding interaction is weak. In this model, the charge carriers are no longer treated as delocalized wavefunctions, but as localized particles on individual sites (**Figure 2.4b**). If the localization is strong, the charge can only hop to the nearest states, and this is called the nearest neighbor hopping or Miller-Abraham hopping.[23] Hopping is a thermally assisted process since the potential barrier between neighboring sites needs to be overcome, so the hopping conductivity (and mobility) follows an Arrhenius-type temperature dependence $\sigma \propto \exp(-E/k_BT)$. If the localization is not so strong and the wavefunction overlap is not limited to the nearest neighbors, the charge can hop over a relatively long distance, which is called variable range hopping (VRH). It is worth noting that the temperature dependence of VRH mobility is determined by the details of trap density of states (DOS). For Mott VRH where the DOS distribution is constant, the temperature dependence is $\sigma \propto \exp(-(T_0/T)^{-0.25})$;[24] for Efros-Shklovskii VRH where a soft Coulomb gap is introduced near the Fermi level at low temperatures, the temperature dependence is modified to $\sigma \propto \exp(-(T_0/T)^{-0.5})$.[25]

2.1.4 Dynamic disorder (transient localization) model

The weak van der Waals bonding and low mobility of organic semiconductors indicate that charge transport in organic semiconductors is not dominated by the same mechanism in inorganic semiconductors. In the early stages of organic semiconductor research when the mobility was found to be very low (< 1 $cm^2V^{-1}s^{-1}$), band transport in those materials was thought to be impossible. Therefore, theoretical models based on the molecular

characteristics instead of the band characteristics were developed. One example is the famous Marcus model for hopping transport, which is still currently used by many researchers, though some of its critical assumptions are no longer valid in the state-of-the-art high mobility organic semiconductors.[13,26] As mentioned in the earlier section, the feature of band transport is decreasing mobility with increasing temperature. Such a temperature dependence has been observed in highly ordered organic single crystals since the pioneering time-of-flight (TOF) measurement by Karl and coworkers.[27] In the last decade, similar phenomena have also been observed in several high mobility organic single crystal FETs.[8,28–37] However, one can estimate the carrier mean free path in the best organic semiconductor (rubrene single crystals) from the mobility (~ 10 $cm^2V^{-1}s^{-1}$), and the result is ~ 1 nm, which is on the same order of the lattice parameters and much smaller than the carrier mean free path in inorganic semiconductors (> 10 nm).[9] Clearly, charge transport in organic crystals is not as "band-like" as that in inorganic semiconductors.

The difficulty in developing a universal model for charge transport in high mobility organic semiconductors mainly comes from the fact that several important interactions have comparable energy scales. In particular, the transfer integral t and the reorganization energy λ are both ~ 100 meV. This intermediate condition fulfills the requirements of neither hopping nor band transport. Recently, it was found that thermal intermolecular vibrations can be very large due to the weak van der Waals bonding and the large molecular mass, and such vibrations can modify the transfer integral significantly.[38] Based on this phenomenon, the dynamic disorder model was developed by Troisi, Fratini and coworkers, and it provides a consistent picture of charge transport in high mobility organic semiconductors.[39–44]

The basic assumption of the dynamic disorder model is that the electronic wavefunction is transiently localized due to thermal vibrations (**Figure 2.4c**). For this reason, this model is also called transient localization. The typical time scale of localization is similar to the time scale of intermolecular vibrations, so the transfer integral is predominantly modulated by the low frequency intermolecular modes. In this scenario, the carrier mobility can be expressed as:[44]

$$\mu = \frac{e}{k_B T} l_{loc}^2 \omega \tag{2.2}$$

Here, ω is the intermolecular vibration frequency and ω^{-1} can be viewed as the characteristic time that charge is transiently localized due to the lattice dynamics, l_{loc} is the length that charge can spread within the characteristic time ω^{-1} and is limited by the dynamic disorder as well as the transfer integral. Higher temperatures lead to higher degrees of dynamic disorder, reducing the transfer integral and the localization length. As a result, a lower mobility is expected when the temperature increases, and band-like transport is predicted by this model.

2.2 Organic field-effect transistors (OFETs)

2.2.1 Device structure and operating mechanism

One of the most widely-used experimental platforms for studying charge transport is the FET. A FET is composed of a semiconducting layer, an insulating dielectric layer, and three electrodes, namely, the source, the drain and the gate, and these components can be stacked in different orders (**Figure 2.5**). For an OFET, the semiconducting layer is made of an organic semiconductor, which could be a solution- or vapor-processed thin film or a single crystal. Unlike conventional Si-based metal-oxide-semiconductor FETs (MOSFETs), most OFETs operate in the accumulation regime instead of the inversion

regime. There is no depletion region to isolate the device, and the low intrinsic conductivity of the organic semiconductor leads to the low off-current.

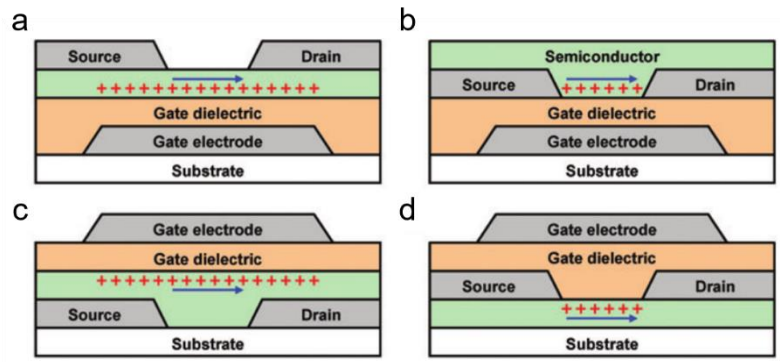

Figure 2.5 Different architectures of FETs: (a) bottom-gate, top-contact, (b) bottom-gate, bottom-contact, (c) top-gate, bottom-contact, (d) top-gate, top-contact.[45]

A FET behaves like a valve, which controls the magnitude of the current flow through it. Such a function is achieved by applying a voltage to the gate electrode, a process called gating. When a gate voltage (V_G) is applied, charge carrier accumulation occurs at the semiconductor/dielectric interface, and the application of a drain voltage (V_D) makes the current flow from source to drain. Therefore, the device performance is mainly affected by two processes, charge accumulation and injection.

Depending on the polarity of V_G, either holes (p-type) or electrons (n-type) may accumulate at the semiconductor/dielectric interface. A schematic of charge accumulation is shown in **Figure 2.6a**. At the gate-insulator-semiconductor junction, the Fermi levels of all the materials are equal across the junction when no V_G is applied. For a p-type OFET, when a negative V_G is applied, the Fermi level of the gate metal is shifted according to the magnitude of applied potential. the Fermi level of the semiconductor is still fixed, but the HOMO/LUMO levels of the semiconductor near the semiconductor/dielectric interface

start to bend upwards. As a result of band bending, the HOMO level near the interface becomes closer to the Fermi level and hole accumulation is favored. Changing the magnitude of V_G will change the degree of band bending and hence the density of accumulated charge carriers (holes). For an n-type OFET, a similar process happens when a positive V_G is applied. The hole density (p, in unit of cm^{-2}) is modulated by V_G as $p = C_iV_G/e$, where C_i is the specific capacitance of the dielectric. In commonly used solid dielectric materials, C_i is determined by the thickness d and the dielectric constant ε_r.

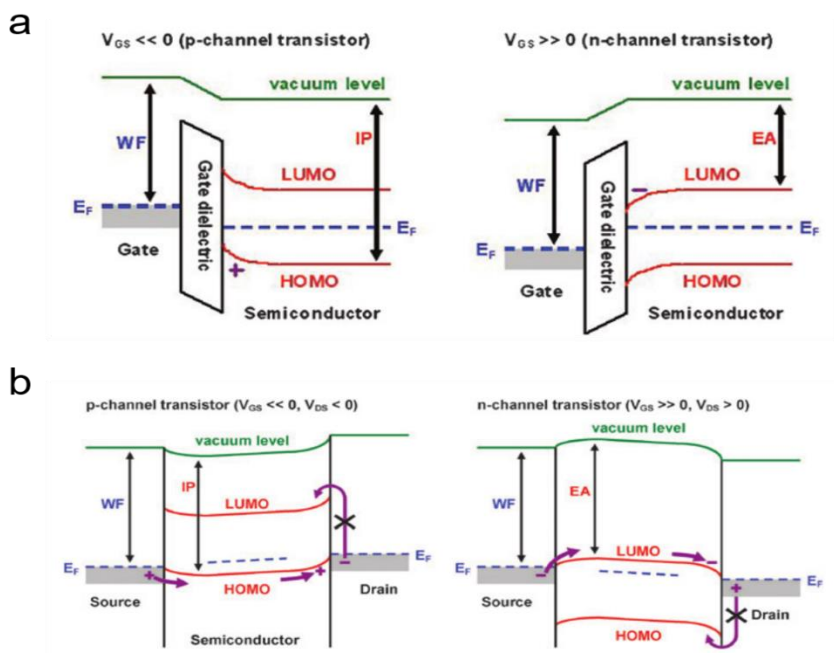

Figure 2.6 (a) Energy-level diagrams across the semiconductor/dielectric interface, showing hole (electron) accumulation for negative (positive) V_G. (b) Energy-level diagrams along the channel, showing the transport of holes (electrons) from the source to the drain under negative (positive) V_D.[45]

When negative V_G and V_D are applied, holes are injected from the source, flowing in the HOMO band across the channel, and are extracted from the drain (**Figure 2.6b)**. The magnitude of the source-drain current (I_D) is not only controlled by accumulated charge density, but also by the magnitude of V_D. It is worth noting that, however, the workfunction

of source/drain contacts plays an important role in charge injection. For p-type OFETs, high-workfunction metals such as Au or Pt are preferred, because large Schottky barriers for hole injection would form at the metal/semiconductor interface and impede the p-type conduction if low-workfunction metals were used.[46] Similarly, low-workfunction metals are beneficial for electron injection. In some cases, both holes and electrons can be injected and transported in the same device, which is called ambipolar transport.[47]

2.2.2 Electrical characterization

The performance of OFETs is usually characterized by measuring transfer curves (I_D-V_G at constant V_D) and output curves (I_D-V_D at constant V_G). The gradual channel approximation still holds in OFETs, which means all the principles for conventional inorganic FETs are still valid. The detailed derivation of I_D can be found in several references and the general expression for I_D is:[48]

$$I_D = \frac{W}{L}\mu C_i V_D[(V_G - V_{TH}) - \frac{V_D}{2}] \tag{2.3}$$

where W and L are the channel width and length, V_{TH} is the threshold voltage which physically represents the transition from off-state to on-state. If the applied V_D is small ($V_D << V_G - V_{TH}$), the device is in the linear regime, and the expression of I_D can be reduced to:

$$I_D = \frac{W}{L}\mu C_i V_D(V_G - V_{TH}) \tag{2.4}$$

Equation (2.4) is effectively another form of the definition of conductivity $\sigma = \mu pe = \frac{L}{W}\frac{\partial I_D}{\partial V_D}$, where $pe = C_i(V_G - V_{TH})$. Based on Equation (2.4), the mobility can be extracted from the slope of the transfer curve:

$$\mu = \frac{\partial I_D}{\partial V_G}\frac{L}{WC_iV_D} \tag{2.5}$$

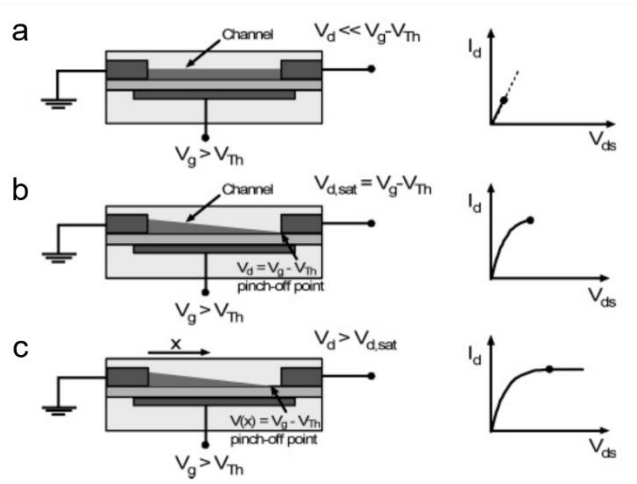

Figure 2.7 Illustrations of operating regimes of FETs: (a) linear regime, (b) onset of saturation regime at pinch-off, (c) saturation regime.[47]

For a drain voltage that is large enough ($V_D > V_G - V_{TH}$), the device operates in the saturation regime. Here the gradual channel approximation breaks down, because the lateral potential drop becomes comparable to the longitudinal potential drop (**Figure 2.7**). The carrier distribution is no longer uniform across the channel. In the pinch-off region near the drain electrode, the charge carrier density falls to zero. At this stage, further increase of V_D will not increase I_D, but only expand the pinch-off region. The real potential drop across the channel is $V_G - V_{TH}$, and Equation (2.3) becomes:

$$I_D = \frac{W}{2L}\mu C_i (V_G - V_{TH})^2 \tag{2.6}$$

The saturation mobility can be extracted from the slope of $\sqrt{I_D}$ versus V_G:

$$\mu = \left(\frac{\partial\sqrt{I_D}}{\partial V_G}\right)^2 \frac{2L}{WC_i} \tag{2.7}$$

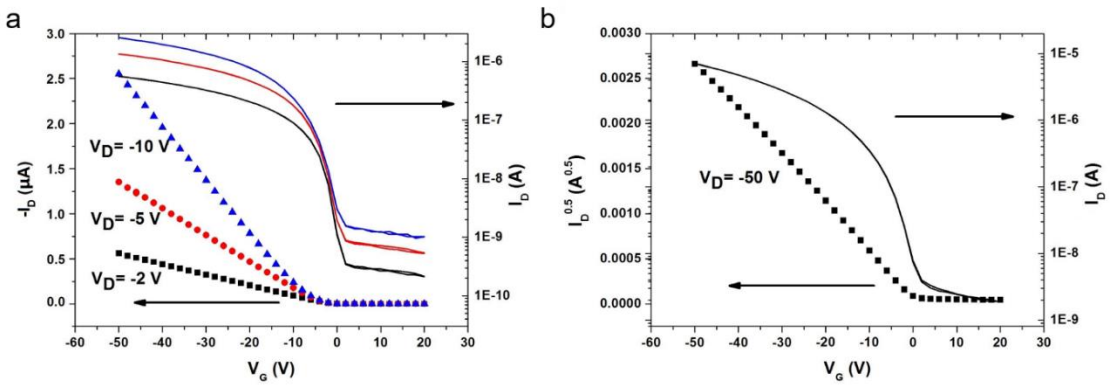

Figure 2.8 Textbook-like transfer curves of a rubrene single crystal OFET in (a) linear regime and (b) saturation regime.

Carrier mobility is the key parameters for evaluating the performance of OFETs. However, great care has to be taken when extracting mobility from a real device. The mobility is assumed to be V_G-independent during the derivation of equations in this section, which works well in some good devices (see **Figure 2.8** as an example) but is not always true in real experiments due to the existence of non-idealities including contact resistance and traps. Reliable extraction of mobility is therefore critical for organic semiconductor research and will be discussed in the next section.

2.2.3 Reliable extraction of carrier mobility

In real OFETs, there are always some non-idealities. The most commonly observed ones are the non-linearities in transfer curves (**Figure 2.9**).[49] In many OFETs, especially those based on high mobility polymer semiconductors, the so-called "double-slope" phenomenon widely exists, where the apparent mobility is high at low V_G but low at high V_G. According to Uemura *et al.*[50] and Bittle *et al.*,[51] this is due to the fact that the contact resistance dominates the overall resistance at low V_G and decreases very fast with increasing V_G. The high slope at low V_G is just an artifact due to the V_G-modulated rapid decrease of contact resistance. Unfortunately, many researchers simply report the mobility

value extracted from the highest-slope region. As a result, overestimation of mobility widely exists and may misguide future research directions of the field.[52–54]

In addition to contact resistance, another important source of error is charge-density-dependent mobility.[55] This phenomenon widely exists in organic semiconductor thin films where a high degree of extrinsic disorder exists. Trapping of charge carriers in the band tail states results in larger mobility at larger V_G, since the Fermi level is closer to the band edge when the charge density is higher. In this case, the mobility should be calculated from the linear regime, in which the carrier distribution across the channel is uniform. In many publications, however, only saturation mobilities are reported. The carrier density in the saturation regime varies significantly from source (maximum) to drain (zero), so saturation mobility is less reliable.

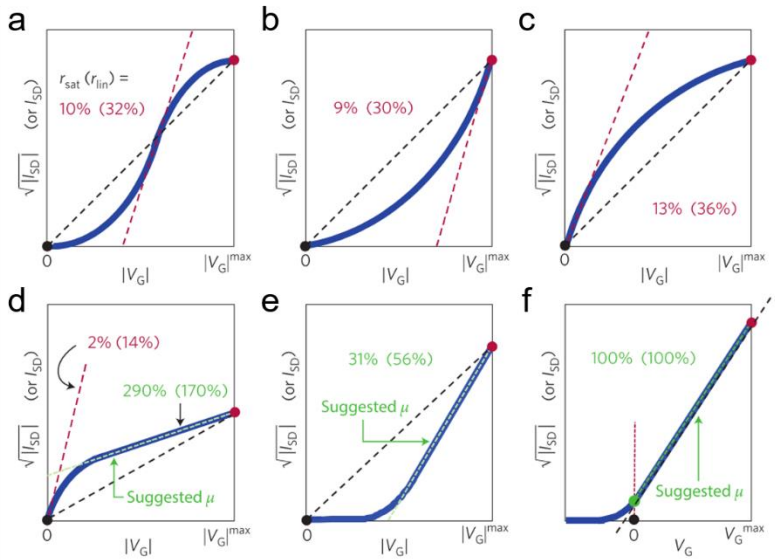

Figure 2.9 Commonly observed non-linearities in OFET transfer curves: (a) S-shaped curve, (b) super-linear curve, (c) sub-linear curve, (d) double-sloped curve, (e) linear curve with a large threshold voltage, (f) ideal transfer curve.

In order to accurately extract carrier mobility from an OFET, in a recent commentary, Choi *et al.* suggested that one should pay attention to several guidelines to avoid common

pitfalls.[49] These guidelines are: (1) check the linearity of transfer curves; (2) extract mobility from the linear regime; (3) extract contact resistance; (4) characterize hysteresis and sweep-rate dependence; (5) avoid applying large V_D when measuring OFETs with small channels; (6) perform Hall measurements on claimed high-mobility devices. They also introduced a parameter called the reliability factor so that the reliability of claimed mobility can be evaluated properly.

Based on the paragraphs above, two methods are found to yield reliable values of mobility. The first one is gated 4-probe measurement in the linear regime, which is a slightly modified version of a standard transfer curve measurement.[56] In the 4-probe geometry, 2 voltage-sensing probes are inserted between the source and drain to measure the real potential drop within the channel (**Figure 2.10a**). In this configuration, the potential drop is linear across the channel, so the channel sheet resistance (R_{ch}), the contact resistance (R_c), and the contact-corrected 4-probe mobility (μ_{4p}) are given by:

$$R_{ch} = \frac{W}{\Delta L}\frac{\Delta V}{I_D} \tag{2.8}$$

$$R_c = \frac{V_D}{I_D} - \frac{\Delta L}{L}\frac{\Delta V}{I_D} \tag{2.9}$$

$$\mu_{4p} = \frac{\Delta L}{WC_i}\frac{\partial \frac{I_D}{\Delta V}}{\partial V_G} \tag{2.10}$$

where ΔL and ΔV are, respectively, the distance and the potential difference between the two reference probes. In high quality OFETs, μ_{4p} is usually independent of V_G, indicating the good reliability of the extract mobility value. Details of gated 4-probe measurement can be found in several references.[56,57]

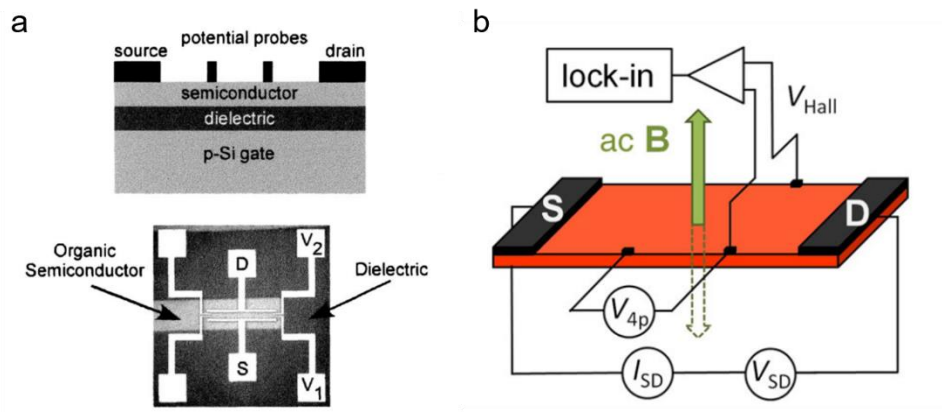

Figure 2.10 Device geometries for (a) gated 4-probe measurement,[56] and (b) Hall effect measurement.[58]

If a high mobility is claimed in an OFET, Hall measurement is highly favored to confirm the reliability of the mobility, because stronger charge delocalization is indicated by high mobility and Hall measurement provides information about diffusive, band-like transport through delocalized states. The typical geometry for Hall measurement is called the Hall-bar geometry, in which 2 voltage-sensing probes are inserted between the source and drain on opposite sides of the channel (**Figure 2.10b**). During a typical Hall measurement, a constant V_D (or I_D) is applied and the transverse Hall voltage (V_{xy}) is measurement while sweeping a magnetic field perpendicular to the channel. The relationship between the Hall resistance (R_{xy}, defined as $R_{xy} = V_{xy} / I_D$) and the magnetic flux density (B) is usually plotted. The slope of R_{xy}-B is the Hall coefficient R_H, which is related to the hole (or electron) density p_{Hall} (or n_{Hall}) as $R_H = 1/ep_{Hall}$. The Hall mobility (μ_{Hall}) can be calculated using

$$\mu_{\text{Hall}} = \frac{\sigma}{ep_{\text{Hall}}} = \frac{R_{xy}}{BR_{xx}}\frac{\Delta L}{W} \tag{2.11}$$

where Rxx is defined as $Rxx = \Delta V/I_D$. It is worth noting that hall effect has only been observed in very few organic semiconductors.[9,30,32,59–62] However, tens or hundreds of organic semiconductors are claimed to exhibit mobilities over 1 $cm^2V^{-1}s^{-1}$. Obviously, most of the reported mobility values are overestimated.

2.3 Organic semiconductor single crystals

Unlike amorphous or polycrystalline thin films of organic semiconductors where lots of extrinsic defects such as impurities or structural disorder exist, organic semiconductor single crystals with highly ordered structure provide an ideal testbed for intrinsic charge transport studies. Charge transport in OFETs based on organic semiconductor single crystals has emerged as an active research area since early 2000s, and many physical phenomena observed in those organic crystals have never been reported in conventional thin film OFETs.

2.3.1 Crystal growth

Growth of high quality crystals is the prerequisite for investigating charge transport in organic crystals. Generally speaking, many methods developed for inorganic crystal growth can still be applied to grow organic crystals. The growth methods can be divided into 3 major categories: melt growth, solution growth, and vapor growth.[63]

Melt growth methods, including zone refining,[64] the Bridgman method,[65] and the Czochralski method,[66] have been widely used to grow high quality inorganic crystals such as Si (**Figure 2.11**). In a typical zone refining growth, only a small part of the material (sealed in an ampoule) is molten and the heating zone moves slowly across the whole ampoule. As the heating zone moves, impurities that are more soluble in liquid phase accumulate at the end of the crystals and high-quality crystals are obtained in the middle part. Other methods such as the Bridgman and the Czochralski methods require the usage of seed crystals as the starting point of large crystal growth. During the Bridgman growth, the whole ingot of source materials is melted, and crystallization occurs on the seed as the ingot moves across the temperature gradient. During the Czochralski process, the seed

crystal is pulled out of the melt to get a large crystal. However, melt growth can only be used to grow organic molecular crystals which have low vapor pressure and are stable at high temperatures. These conditions are hard to meet, so only a few organic molecules, including naphthalene[67] and anthracene,[68] have been grown from the melt.

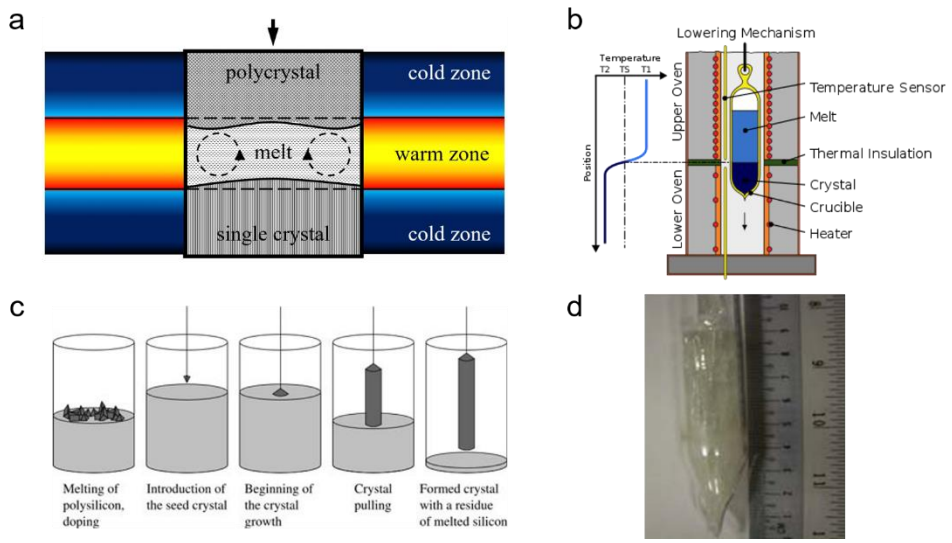

Figure 2.11 (a) Zone refining process.[69] (b) Bridgman method.[70] (c) Czochralski method.[71] (d) An anthracene crystal grown by zone refining.[68]

Solution-based methods are perhaps the simplest ones to grow organic crystals if the organic molecules are soluble in certain solvents. The prerequisite for crystallization is to prepare supersaturated solutions of organic molecules, which can be achieved by slow evaporation of solvents, slow change of temperature, and introduction of poor solvents. For instance, if the supersaturated solution is not sealed, the crystal nuclei spontaneously form and grow into large crystals as the solvent slowly evaporates. For some materials with highly temperature-dependent solubility, similar crystal nucleation and growth can be induced by changing the temperature across the saturation point. If the solubility of the material is high in one solvent but low in another solvent, diffusion of poor solvent into

good solvent leads to crystal nucleation and growth. The diffusion can be achieved by either the evaporation or the direct injection of poor solvent.

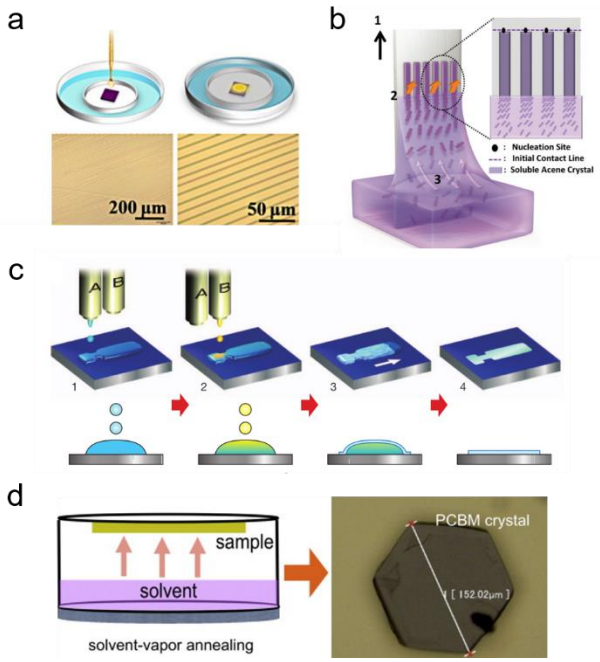

Figure 2.12 (a) TTF crystals grown by drop-casting.[72] (b) TIPS-pentacene crystals grown by dip-coating.[73] (c) C8-BTBT crystals grown by solvent-exchange.[74] (d) PCBM crystals grown by solvent-vapor diffusion.[75]

Various solution-processible techniques have been applied to grow bulk crystals or single-crystalline films, including but not limited to drop-casting, dip-coating, solvent-exchange, and vapor-diffusion (**Figure 2.12**). Recent advances in solution-processed organic semiconductors include growth of large area crystalline thin films,[76] large area patterning of organic transistor arrays,[30] tuning the lattice strain and intermolecular spacing by solution shearing.[77] In terms of device applications, solution-based techniques are advantageous due to the low-cost, high-efficiency nature. They do have drawbacks, however. Trapping of solvent molecules in the solution-grown crystals is inevitable, which causes more extrinsic electronic disorder. As a result, solution-grown crystals are not suitable for intrinsic charge transport study.

Many organic molecules have low sublimation temperatures (lower than their melting points), which makes vapor growth widely applicable in many materials. The physical vapor transport (PVT) method, developed by Kloc *et al.*, is probably the most common technique to grow high quality freestanding crystals for device applications.[78,79] In this experimental setup, the source material is placed in the high temperature region of a closed growth tube to vaporize. The organic vapor is then carried to the low temperature region by a flow of inert gas (Ar, N_2) and crystallization occurs on the sidewall of the growth tube (**Figure 2.13a**). PVT can also be used to purify the source material, because impurities are deposited at regions with different temperatures due to different molecular weights. Currently, most of the high performance organic semiconductor crystals exhibiting band-like behavior, including the benchmark rubrene crystals, are grown by PVT. In addition to growing freestanding crystals, PVT can also be used to grow crystals directly on target substrates such as hBN.[80] The PVT growth parameters, such as temperature gradient, gas flow rate, and type of carrier gas, affect the size, morphology, or even the polymorphism of the crystals finally obtained.

Several other vapor growth methods have also been developed. One example is the traditional physical vapor deposition (PVD) technique (**Figure 2.13b**). Although PVD is mainly used to deposit continuous thin films, after optimizing the process, it is possible to grow some organic crystals by PVD.[81] Usually crystal substrates or crystal seeds are required to enable epitaxial growth of target crystals. The main disadvantage is that PVD-grown crystals are usually small (~10 μm) and device fabrication can be very challenging. Another example is vapor-Bridgman method, in which the vapor of the material instead of the melt is used to grow single crystals. This method can be used to grow organic crystals

with low stability near the melting point by keeping the heating zone above the sublimation point but below the melting point. Large crystals can be grown by vapor-Bridgman method, but the impurity level can be high because of the simultaneous sublimation of impurities.[82]

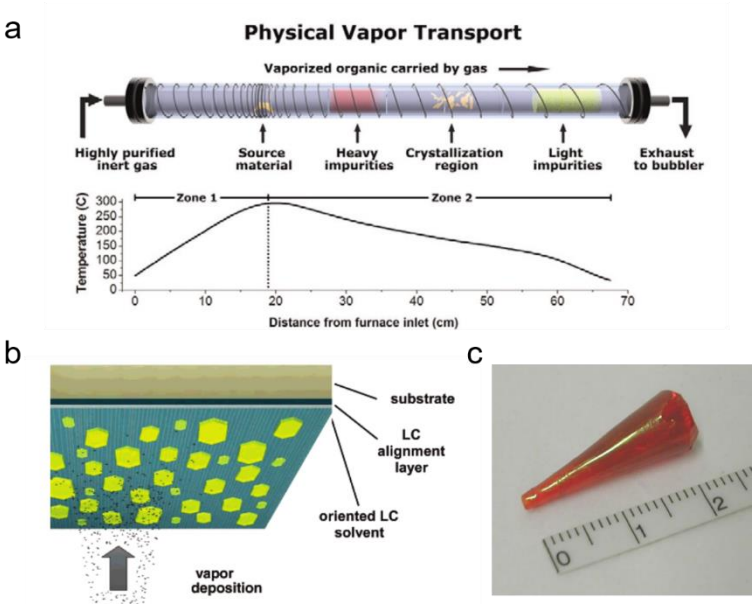

Figure 2.13 (a) Physical vapor transport growth of organic crystals. The temperature profile along the growth tube is also shown.[83] (b) Physical vapor deposition growth with the help of a liquid crystal aligning layer.[81] (c) A tetracene crystal grown by vapor-Bridgman method.[82]

2.3.2 Device fabrication

Optimizing device fabrication is critical to reproducibly obtain high performance single crystal OFETs. In order to measure the intrinsic properties of crystals, the metal/semiconductor contacts and the semiconductor/dielectric interface must have high quality. In the early stage of single crystal OFET research, people found that it is very difficult to deposit conventional oxide dielectric materials onto the surfaces of organic crystals due to the fragile nature of organic crystals. This problem was first solved by Podzorov *et al*., who introduced the CVD-deposited parylene as the dielectric layer of rubrene FETs (**Figure 2.14a**).[84] CVD deposition of parylene occurs at room temperature,

so a conformal, defect-free layer can be coated on rubrene crystals under mild conditions. Recently, it was found that spin-coating a thin layer of a fluorinated polymer called Cytop on rubrene crystals before parylene deposition can improve the device performance due to reduced interfacial trap density.[85] In addition to CVD deposition of parylene, another simple method called vacuum lamination was developed by Yi *et al.*, in which a freestanding plastic thin film is pressed on the crystal surface by vacuum and serves as the dielectric layer (**Figure 2.14b**).[86] The vacuum lamination process is reversible, making it advantageous for comparing the properties of the same crystal under different conditions.

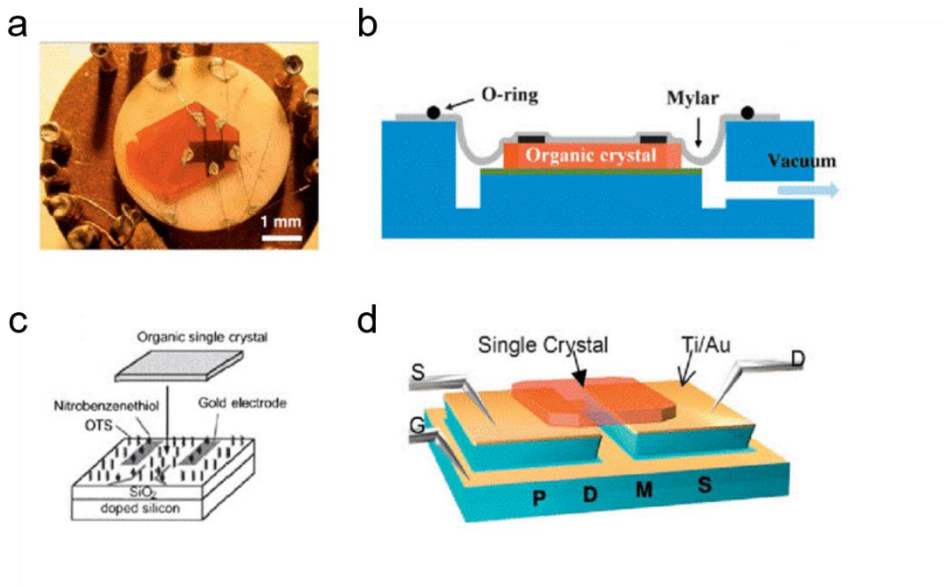

Figure 2.14 (a) A freestanding rubrene FET with CVD-coated parylene dielectric.[5] (b) Single crystal OFET with a vacuum-laminated plastic film as the dielectric layer.[86] (c) Single crystal OFET fabricated on OTS-treated SiO_2 substrate by flip-crystal method.[87] (d) Air-gap single crystal OFET fabricated on flexible PDMS substrate.[88]

Instead of building the device on a crystal, an alternative approach is to laminate the crystal on a prepatterned substrate with metal contacts. This "flip-crystal" method (**Figure 2.14c**) was developed by de Boer *et al.*[89] and Takeya *et al.*,[87] which involves manually aligning a fresh, thin crystal between the source/drain electrodes on the substrate. The

crystal adheres to the substrate by the electrostatic force. It was found that if the crystal is thin enough (~ 1 μm), it can stick to almost any smooth surface firmly. Single crystal OFETs with different dielectric materials, including oxides (SiO_2, Al_2O_3, Ta_2O_5…) and polymers (PS, PMMA, cytop), have been fabricating using this technique.

When a solid dielectric is used to fabricate OFETs, the interfacial electronic disorder including the dipolar disorder from the dielectric layer always exists, which limits the device performance. Studying the intrinsic properties of organic crystals requires the fabrication of air-gap transistors (**Figure 2.14d**), in which the dielectric material is air.[88] To fabricate air-gap transistors, the desired patterns are defined on a silicon wafer by photolithography. The wafer is then put in a clean petri-dish and polydimethylsiloxane (PDMS) pre-polymer is mixed with curing agent and poured into the petri-dish. After it is degassed and baked, the PDMS stamp is peeled off. Finally, Cr/Au contacts are formed by electron-beam evaporation. The fabrication of an air-gap transistor is finished by simply laminating the crystal over the source and drain electrodes.

The air-gap geometry has two major advantages. First, a good interface is formed between the semiconductor layer and the dielectric layer (air) by minimizing the density of interfacial defects. Second, the mechanical flexibility of PDMS substrate allows for lamination of relatively thick crystals, which is impossible for rigid substrates like Si. Thick crystals are more mechanically robust, which is critical for surviving low-temperature measurements where the strain is large due to thermal expansion mismatch. In addition, thick crystals can be reversibly removed and laminated onto PDMS, making multiple measurements on the same crystal possible.

2.3.3 Charge transport in single crystal OFETs

Organic single crystals are different from inorganic ones due to the weak van der Waals bonding, and are different from organic thin films due to the highly ordered structure and low impurity level. As a result, they have some unique features in terms of charge transport. Charge transport phenomena in rubrene single crystals, the benchmark organic semiconductor, are discussed in this section as examples.

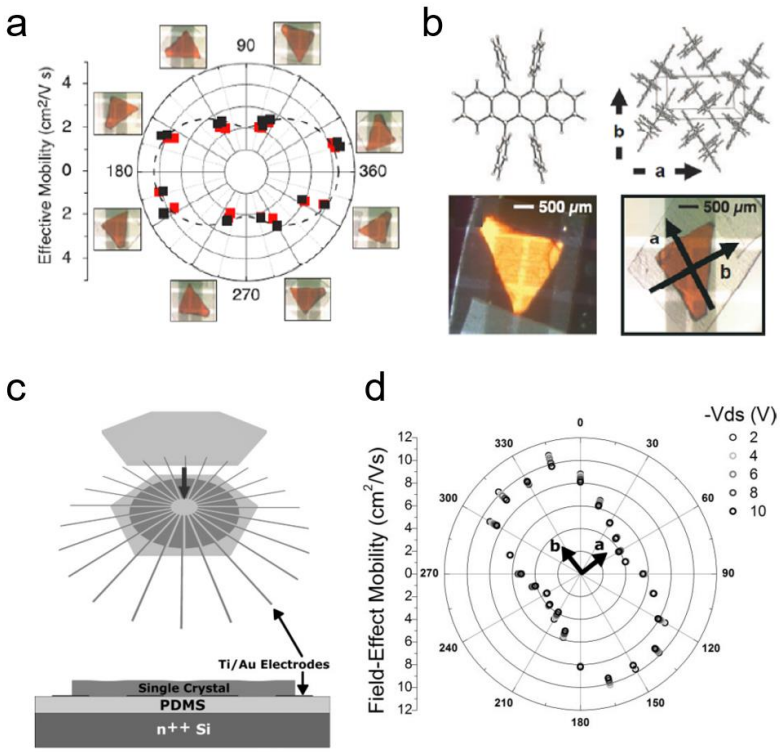

Figure 2.15 (a) Mobility anisotropy in a rubrene single crystal measured by multiple re-lamination. (b) Molecular packing and optical image of rubrene crystals.[90] (c) Device structure with the fan-shaped electrode pattern. (d) Mobility anisotropy measured using the fan-shaped electrode pattern.[91]

The crystal structures of organic crystals usually have low degree of symmetry, leading to anisotropic mobility along different crystallographic directions. Rubrene single crystals have the herringbone-type molecular packing in the π-stacking plane (**Figure 2.15b**). It is clear that the π-stacking direction is along the *b*-axis. As a result, mobility along the *b*-axis

should be much larger than that along other directions due to the stronger π-π overlap. This is exactly what people obtained from experiments. Sundar *et al.* reported the first measurement of mobility anisotropy in rubrene by re-laminating the same rubrene crystal over the source/drain contacts with different orientations.[90] As shown in **Figure 2.15a**, the mobility along the *b*-axis is 3-4 times higher than the mobility along the perpendicular direction. Reese *et al.* designed a fan-shaped electrode pattern to avoid multiple re-lamination of the same crystal, and observed similar results (**Figures 2.15c-d**).[91] Intriguingly, the shape of the crystal is also correlated with the anisotropic bonding. Rubrene single crystals are usually lath-like with a long *b*-axis, which is the π-stacking direction with the strongest intermolecular bonding.

To investigate the nature of charge transport, it is necessary to measure the transfer curves of the same device at different temperatures. As discussed in Chapter 2.1.4, in some highly ordered organic crystals including rubrene, increasing mobility with decreasing temperature (band-like transport) has been observed. The first experimental observation of band-like transport in rubrene air-gap transistors was given by Podzorov *et al.*.[8] As shown in **Figure 2.16a**, the FET mobility of rubrene increases upon cooling. Importantly, although the mobility along the *a*-axis is much smaller, it still shows band-like behavior. Such band-like behavior only exists within a finite temperature range. After a critical temperature, the mobility starts to decrease with decreasing temperature and this regime becomes trap-dominated, because in real crystals there is always some extrinsic disorder. In different samples, the critical transition temperatures may be different due to the different degrees of extrinsic disorder. Remarkably, in some rubrene devices, band-like transport persists at temperature lower than 100 K.[36,37]

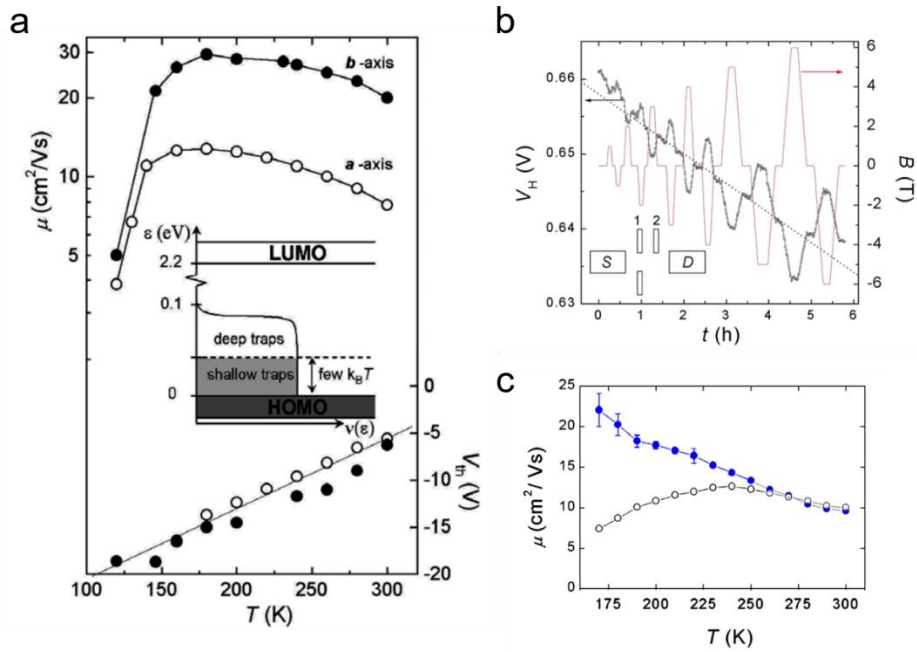

Figure 2.16 (a) Temperature dependence of field-effect mobility and threshold voltage of a rubrene air-gap transistor.[8] (b) Hall voltage and magnetic flux density as a function of time in a rubrene air-gap transistor. (c) Temperature dependence of Hall mobility (blue) and field-effect mobility (black) of the same device shown in (b).[9]

A straightforward explanation of the transition from band-like to hopping transport is given by the multiple trap and release model (MTR).[92] In this model, the impact of shallow traps near the band edge on charge transport are also taken into consideration. Once the carrier is captured by a shallow trap, it cannot move freely before it is activated. The effective mobility (μ_{eff}) is hence limited by the trapping time τ_{tr}:

$$\mu_{eff} = \mu_0 \frac{\tau}{\tau+\tau_{tr}} \tag{2.12}$$

where μ_0 is the intrinsic band-like mobility and τ is the time the carrier moving in the band. At high temperatures, trapped carriers can be easily activated by thermal energy k_BT, so $\tau_{tr} \ll \tau$ and the measured mobility is the intrinsic mobility. If the temperature is low enough that $\tau_{tr} \gg \tau$, the effective mobility becomes $\mu_0(\tau/\tau_{tr})$, which has a temperature dependence

of $\propto \exp(-E/k_BT)$. The low temperature mobility follows an Arrhenius behavior because charge transport is now limited by the thermal activation of charge carriers from traps.

Further evidence for band-like transport in rubrene is provided by the Hall effect measurements in rubrene single crystal transistors (**Figure 2.16b**).[9] Observation of the Hall effect reflects that charge carriers are diffusively transported through delocalized states, since the Hall effect is derived from the band model where only free carriers are involved. The Hall mobility also increases with decreasing temperature, again demonstrating the existence of band-like transport (**Figure 2.16c**). At low temperatures where the FET mobility starts to decrease, the Hall mobility becomes larger than the FET mobility as temperature decreases, indicating that the Hall mobility represents the intrinsic, trap-free mobility of the rubrene crystal. In some materials, coexistence of band-like carriers and hopping carriers leads to a partially delocalized transport, and the Hall effect may become underdeveloped (Hall mobility smaller than FET mobility). A model describing such a phenomenon was recently developed by Yi *et al.*.[85]

The choice of dielectric material is also very important for achieving band-like transport in rubrene. Actually, most of the observations of band-like transport in organic semiconductors are based on the air-gap geometry discussed in Chapter 2.3.2. The influence of dielectric constant on charge transport in rubrene single crystal FETs has been studied by Morpurgo and coworkers.[11,93] With increasing dielectric constant, the mobility decreases sharply from 15-20 $cm^2V^{-1}s^{-1}$ (air-gap, $\varepsilon_r = 1$) to ~1 $cm^2V^{-1}s^{-1}$ (Ta_2O_5, $\varepsilon_r = 25$) (**Figure 2.17a**).[11] Furthermore, the temperature dependence of mobility changes from band-like to thermally activated with increasing dielectric constant (**Figure 2.17b**).[93] This ε_r-dependent behavior is explained by the formation of Froelich polaron at the

rubrene/dielectric interface. The polarizability of the dielectric becomes stronger with increasing dielectric constant, resulting in stronger coupling between the charge and the surrounding polarization. The charge becomes localized due to the Froelich polaron, exhibiting lower mobility and thermally activated behavior. In addition to rubrene, similar ε_r-dependent behavior has also been observed in other materials such as PDIF-CN_2.[32]

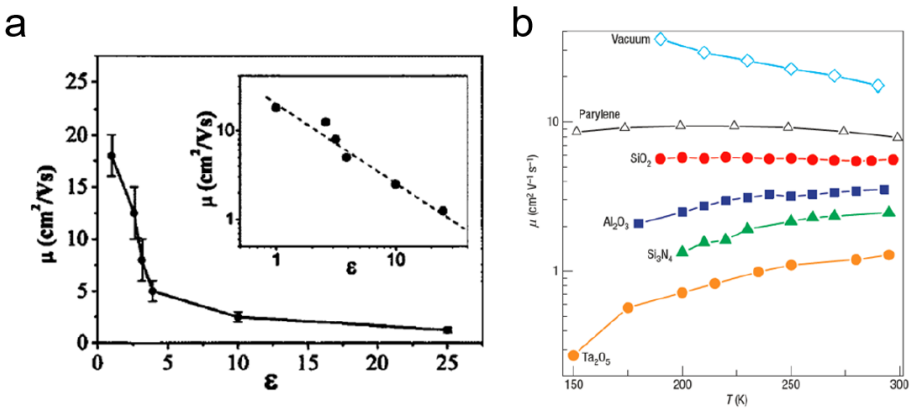

Figure 2.17 (a) Influence of dielectric constant on room temperature FET mobility of rubrene single crystals.[11] (b) Temperature-dependence of mobility for rubrene FETs with different dielectric materials.[93]

2.3.4 Molecules exhibiting delocalized, band-like transport

Figure 2.18 and **Table 2.1** summarize the chemical name, molecular structure, carrier type, room temperature mobility, and reference source of the molecules exhibiting delocalized, band-like transport. Only organic semiconductors which show clear band-like temperature dependence of mobility and nearly ideal transfer characteristics are considered as reliable candidates. Many reported high mobility organic semiconductors do not meet these requirements, and thus are not listed here.

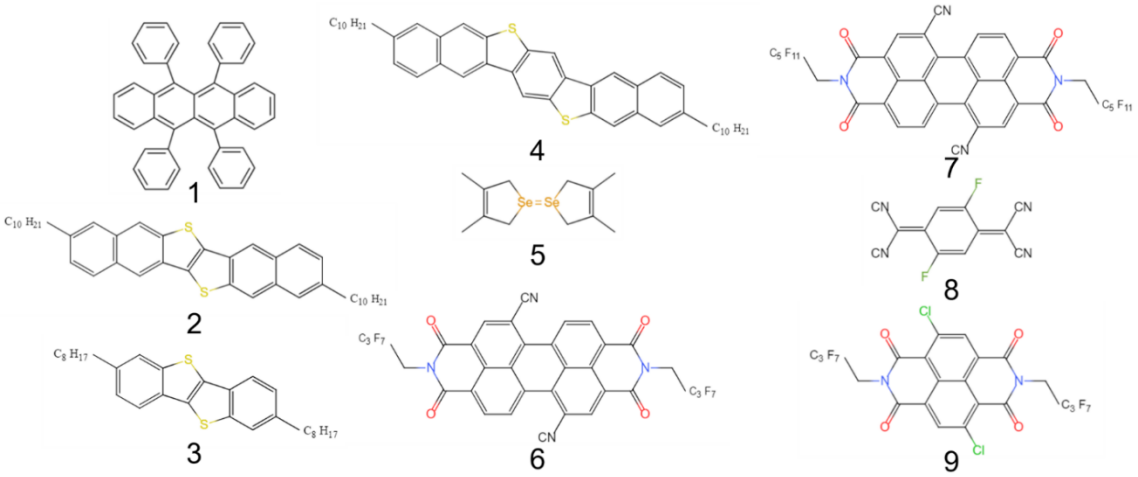

Figure 2.18 Molecular structures of organic crystals exhibiting delocalized, band-like transport.

	Name	Carrier type	Room temperature mobility ($cm^2V^{-1}s^{-1}$)	Reference
1	Rubrene	p-type	~15	many
2	C10-DNTT	p-type	~7	Adv. Mater. 2011, 23, 1626
3	C8-BTBT	p-type	~3	Adv. Mater. 2011, 23, 523
4	C10-DNBDT-NW	p-type	~10	Nat. Commun. 2016, 7, 11156
5	TMTSF	p-type	~4	Phys. Rev. B 2009, 80, 245305
6	PDIF-CN_2	n-type	~5	Adv. Mater. 2012, 24, 503
7	PDI5F	n-type	~3	Adv. Mater. 2014, 26, 1254
8	F_2-TCNQ	n-type	~6	Adv. Mater. 2015, 27, 2453
9	Cl_2-NDI	n-type	~2	Nat. Commun. 2018, 9, 2141

Table 2.1 Name, carrier type, room temperature mobility, and reference source of 9 different organic semiconductors exhibiting band-like transport.

Chapter 3 Electrolyte-Gated Transistors (EGTs)

In conventional FETs with solid dielectric materials (SiO_2, HfO_2…), the specific capacitance of the device is given by ($C_i = \varepsilon_r\varepsilon_0/d$, ε_0 is the vacuum permittivity), and the total charge density is written as p (or n) = $C_i(V_G - V_{TH})/e$. The maximum gate voltage one can apply is not infinite, since every dielectric material has its own breakdown field. Typically, the maximum charge density achieved by using solid dielectrics is on the order of 10^{12} cm^{-2}. To increase the maximum accumulated charge density, people have tried several different methods, including the use of ultrathin films such as self-assembled monolayers or employing high-ε_r oxides.[94,95] In the best cases, charge densities on the order of 10^{14} cm^{-2} can be achieved by using high-ε_r complex oxide ferroelectrics.[96] The fabrication process, however, can be tedious and material-dependent, and it is therefore difficult to obtain a universal platform for accumulating high charge density in different semiconductors. Recently, a technique called electrolyte gating, in which the injection of high charge densities (10^{13} to 10^{15} cm^{-2}) is allowed by using an electrolyte as the dielectric layer, has been developed and widely applied in field-effect transport experiments based on a variety of materials, including both inorganic and organic semiconductors. This chapter will review the working principles of electrolyte-gated transistors (EGTs) and the charge transport phenomena observed in these devices.

3.1 Concept of electrolyte gating

Electrolytes consist of mobile ions and they are ionically conducting but electronically insulating. To understand how an EGT works, the ions' response to the applied gate electric field needs to be considered. First, imagine a metal/electrolyte/metal capacitor (**Figure 3.1**).

When an electric field is applied, ions can respond to the electric field quickly and accumulate at the electrolyte/metal interfaces to form the so-called electrical double layers (EDLs). An EDL is two layers of opposite charge separated by a short distance of ~1 nm. In the simplest model, it can be viewed as a parallel plate capacitor. Since the thickness of the capacitor is very small and capacitance is inversely proportional to thickness, the capacitance of an individual EDL capacitor can be very huge. For a metal/electrolyte/metal capacitor, two EDLs are formed at the electrolyte/metal interfaces, and the bulk electrolyte is ideally charge neutral, because there is no driving force for ion migration after the formation of EDLs. The equivalent circuit of a metal/electrolyte/metal capacitor is two EDL capacitors in series, and the total capacitance is one half of the capacitance of the individual EDL capacitor. In addition, unlike the conventional dielectrics where the potential drops linearly across the dielectric layer, the total capacitance of an electrolyte layer does not depend on the thickness, since potential drop only occurs at the EDLs. Typically, capacitance values over 1 μF/cm^2 are obtained by electrolyte gating, which means charge densities over 10^{13} cm^{-2} can be easily achieved by applying a gate voltage of a few volts.

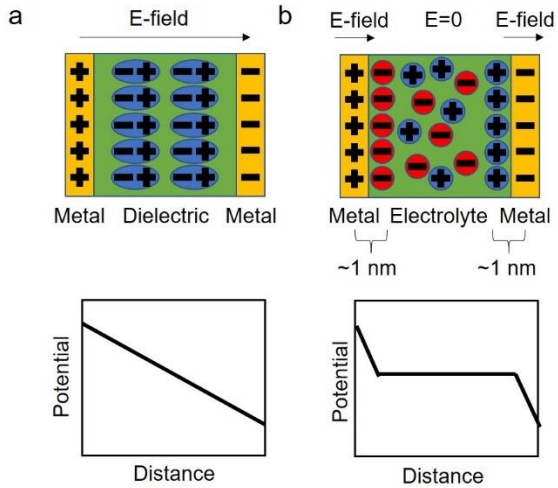

Figure 3.1 (a) Polarization of electron clouds in a solid dielectric under bias (top) and corresponding potential as a function of distance from interface (bottom). (b) Electrical double layer formation in an ionic liquid under bias (top) and corresponding potential as a function of distance from interface (bottom).

Depending on the nature of the semiconductor, EGTs can be divided into two categories: electrical double layer transistors (EDLTs) and electrochemical transistors (ECTs) (**Figure 3.2**).[97] In an EDLT, the semiconductor layer is not permeable to the ions in the electrolyte. Upon the application of V_G, the ions accumulate at both the electrolyte/semiconductor and the electrolyte/metal interfaces, resulting in charge accumulation in the semiconductor layer. The schematic of an EDLT is pretty similar to a metal/electrolyte/metal capacitor, except that the capacitance of the electrolyte/semiconductor EDL is typically smaller than the capacitance of the electrolyte/metal EDL. As a result, the total capacitance is limited by the former one. Semiconducting materials used in EDLTs are usually single crystals or epitaxial thin films. Ions cannot diffuse into the semiconductor layer during the operation of EDLTs due to the highly ordered structure and small intermolecular distance in those materials. If the applied voltage is greater than the electrochemical window of the electrolyte, however, dielectric breakdown happens and the EDLT is no longer working properly. To maximize the electrochemical window, sometimes the EDLT is characterized at low temperatures so that a larger charge density can be achieved.[98]

If the semiconductor layer becomes permeable to the ions in the electrolyte, the EGTs are called ECTs. In this case, the EDL is still created at the electrolyte/metal interface; however, on the electrolyte/semiconductor side, ions can diffuse into the semiconductor layer to induce charge when a gate voltage is applied. This process is called electrochemical doping and has been observed in many polymer semiconductors in contact with electrolytes

due to the permeable nature of polymer films. The operation of ECTs is mainly described in terms of gate-tunable electrochemical doping and de-doping of the semiconductor layer. It is worth noting that in addition to the accumulation mode, some ECTs work in the depletion mode. One example is the ECT based on PEDOT:PSS, an intrinsically conducting polymer.[99] When a positive V_G is applied, cations diffuse into and de-dope the semiconductor layer, leading to the decrease of channel conductivity and eventually turning off the device.

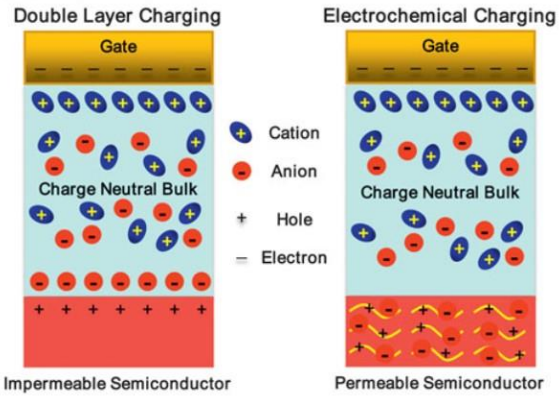

Figure 3.2 Charge accumulation mechanisms in EGTs: double layer electrostatic charging (left) and electrochemical charging (right).[97]

Charge accumulation in EDLTs is considered as 2D, while charge accumulation in ECTs is believed to be 3D. 3D electrochemical doping in ECTs usually causes structural changes such as swelling of the semiconductor layer, which has been experimentally observed using X-ray diffraction.[100] Therefore, for a long time, people believe that EDLTs are better for fundamental charge transport studies since the original structures of semiconductors are not disrupted. Recently, breakthroughs in ECTs based on inorganic crystalline thin films have demonstrated that ECTs are also useful for tuning electronic phase transitions in some cases. For example, gate-tunable oxidation and reduction results in the insulator-metal

transition in VO_2;[101] gate-induced Li^+ intercalation into several 2D materials including $MoTe_2$ leads to the observation of superconductivity.[102]

3.2 Electrolyte materials

The electrolytes used in ECTs in the early stages were *liquid solutions of small ions* such as Li^+, K^+, Cl^-, ClO_4^- (**Figure 3.3a**). Application of liquid electrolytes in organic ECTs was pioneered by Wrighton and coworkers in 1980s.[103–108] By immersing a reference electrode serving as the gate into the liquid electrolyte, the conductivity of polymer semiconductors including polyaniline and poly(3-methylthiophene) can be reversibly tuned by electrochemical doping and de-doping. Similar techniques were later widely used to gate single-strand carbon-nanotube transistors.[109,110] The band bending at the semiconductor/electrolyte interface is strongly affected by the type and concentration of ions in the electrolyte solution, so liquid-electrolyte-gated transistors have been applied in the area of chemical and biological sensing.[111,112]

Obviously, the flowing nature of liquid electrolytes makes them non-ideal for practical applications. In addition to dissolving ions in aqueous or organic solvents, ions can also be dissolved in solvent-free polymers to form the so-called *polymer electrolytes*. One of the most famous polymer electrolytes is $LiClO_4$ dissolved in poly(ethylene oxide) (PEO) (**Figure 3.3b**).[113] The ionic motion is coupled with and boosted by the large-amplitude relaxation of PEO chains due to the low glass transition temperature of PEO (-60 ^oC), which leads to high ionic conductivity comparable to that in liquid electrolytes at room temperature. Polymer electrolytes can be easily fabricated by drop-casting or spin-coating from solutions. They were first used to gate carbon nanotube network transistors,[114] but soon become popular as dielectric materials in OFETs. For example, Panzer *et al.* utilized

$LiClO_4$/PEO to gate various organic semiconductors, including single crystals (e.g., rubrene),[115] small molecule thin films (e.g., pentacene),[116] and polymers (e.g., P3HT),[117] and obtained stable sub-3V device operation. Similar polymer electrolytes were also used in inorganic EDLTs, resulting in accumulation of charge densities over 10^{14} cm^{-2} and novel phenomena such as gate-induced superconductivity in STO.[118]

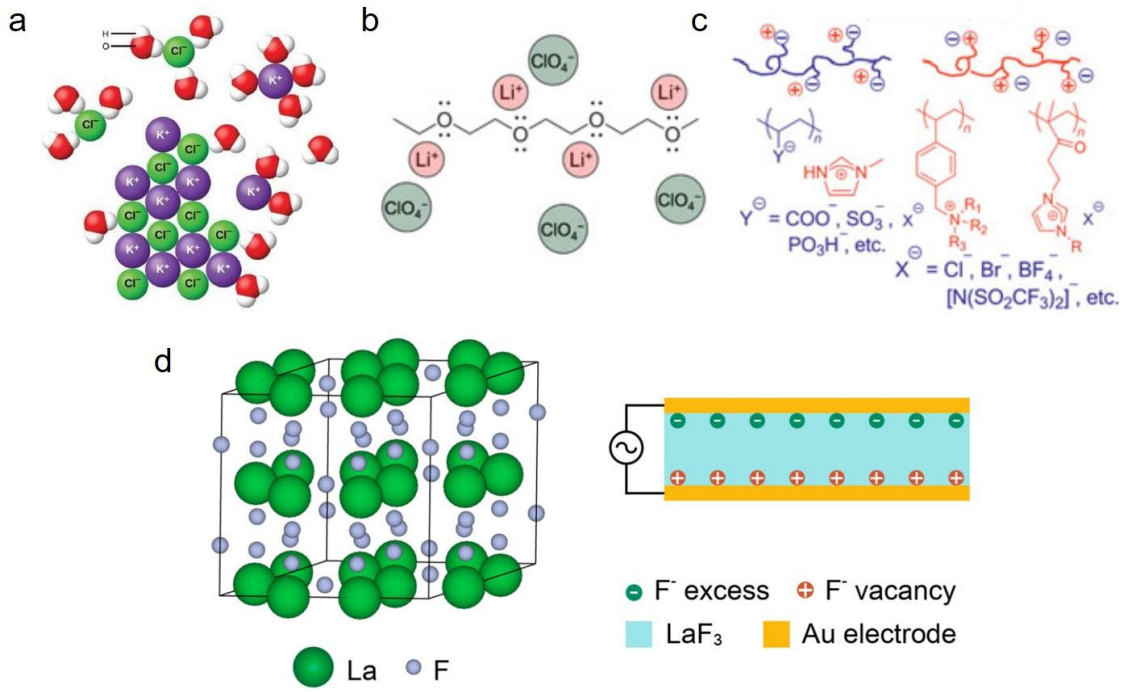

Figure 3.3 (a) Schematic of KCl dissolved in water.[119] (b) Schematic of Li^+ ion coordination with a PEO chain in $LiClO_4$/PEO.[97] (c) Chemical structures of several polyelectrolytes.[97] (d) Crystal structure of LaF_3 (left) and schematic of EDLs formation (right).[120]

Another class of widely used polymer electrolytes is known as *polyelectrolytes*, which consist of ionic polymer backbones and mobile counterions (**Figure 3.3c**). Since only one type of ions are mobile, it becomes possible to tune the operation mode (EDLT or ECT) of the EGT by properly choosing the polyelectrolyte. One example is poly(styrene sulfonic acid) (PSSH) introduced by Berggren and coworkers, which is a polyanionic proton

conductor (mobile H^+).[121] When PSSH is used to gate p-type polymer semiconductors such as P3HT, under negative V_G, the H^+ forms the EDL at the gate/electrolyte interface, and the PSS^- forms another EDL at the electrolyte/semiconductor interface without any electrochemistry doping due to the negligible diffusivity of polyanions. If PSSH is used to gate an n-type polymer semiconductor, however, under positive V_G, the H^+ can diffuse into the semiconductor layer and electrochemically dope the semiconductor.

Recently, a new type of solid electrolytes, *inorganic ion-conductive solids*, has been identified. In these electrolytes, ions are free to move within a solid framework composed of inorganic elements. The mobile ions can be either cations (e.g., Li^+ conducting glass ceramics) or anions (e.g., LaF_3) (**Figure 3.3d**).[120,122–124] The main advantage of inorganic ion-conductive solids is that they can be used as substrates for micro- or nano-fabrication processes, which is not possible for any other type of electrolytes. After transferring or growing semiconductors on top of the substrate, source/drain contacts can be patterned by standard lithography technique, and the backside of the substrate can be metalized to serve as the gate. Using this method, EDLTs based on graphene,[122,123] MoS_2[120] and FeSe[124] have been fabricated on different inorganic ion-conductive solid substrates.

Most solid electrolytes mentioned earlier in this chapter have relatively slow ionic mobilities, which means the timescale of EDL formation is large and the switching speed of the device is low. To achieve faster-switching EGTs, conventional inorganic ions are replaced by *ionic liquids* (ILs) with high ionic conductivities. ILs are solvent-free molten salts at room temperature due to the weak Coulomb forces between large ions. **Figure 3.4a** shows several commonly used ionic components.[125] The high ionic conductivity comes from the weak electrostatic interactions between the ions and from the high ionic

concentration. ILs also have negligible vapor pressure, suggesting that they are ideal for low-temperature charge transport measurements in vacuum. Furthermore, ILs are not very chemically reactive and have relatively larger electrochemical windows. The combination of all these features makes ILs probably the most widely used electrolyte for studying charge transport in EGTs based on both organic and inorganic materials. Besides, ILs are chemically designable as well, which provides the opportunity to study the structure-property relationship at the semiconductor/electrolyte interfaces.

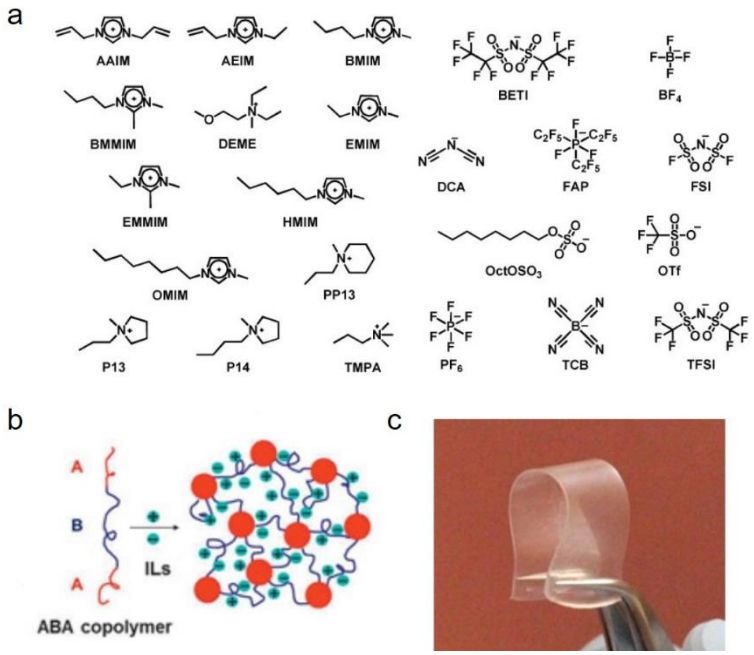

Figure 3.4 (a) Cations (left half) and anions (right half) of the commonly used ILs.[125] (b) Self-assembly of an ABA triblock copolymer in an ionic liquid to form an ion gel.[97] (c) Optical image of a freestanding film of mechanically robust ion gel (a mixture of IL [EMI][TFSI] and polymer P(VDF-HFP)).[126]

Despite their excellent electrical properties, the liquid nature of ILs limits their application in practical devices. To increase the mechanical rigidity without losing too much ionic conductivity, ILs are mixed with cross-linked block copolymers (~10 wt%) to form the solid electrolytes called *ion gels*.[127] Typically, ABA-type triblock copolymers with soluble B block and insoluble A blocks, such as PS-PMMA-PS, are used (**Figure**

3.4b). The properties of ion gels can be tuned by variations of block copolymers. For example, when mixing ILs with different polymers, the resulting ion gels can be printable,[128] freestanding (**Figure 3.4c**),[126] UV curable,[129] or even degradable.[130] Importantly, the polymers swollen in ILs do not limit the motion of the liquid molecules, which means high ionic conductivities of ILs are preserved. Using ion gels, high frequency operation at >10 kHz has been achieved in EGTs based on polymer semiconductor P3HT.[131]

3.3 Device fabrication and characterization

3.3.1 Fabrication of EGTs

In most EGTs, the semiconductor layer and the source/drain electrodes are fabricated first on an insulating substrate, then the electrolyte is applied on the substrate, covering the channel of the device (**Figure 3.5a**). To put ILs onto the device, people usually dip tools such as sharp needles or thin metal wires into the IL containers. Thanks to the surface tension, a small drop of IL stays at the end of the tool when taking the tool out of the container, and the IL drop can be quickly transferred onto the desired position. Application of other electrolytes such as ion gels is much easier. They can be printed directly onto the substrate by ink jet or aerosol jet printing techniques.[128,132] For certain ion gels that are mechanically robust enough, a "cut-and-stick" approach has been realized, in which the ion gel film is cut by a razor blade, then peeled off and transferred by a pair of tweezers (**Figure 3.4c**).[126]

One advantage of EGTs is that due to the thickness-independent capacitance of electrolytes, the gate electrode does not have to stay above or below the semiconducting channel (i.e., the side-gated geometry becomes possible).[128] Consequently, one no longer

needs to worry about how to precisely align a gate over the EGT channel, and the side-gated geometry becomes the most convenient device geometry for charge transport experiments when ILs are used as electrolytes (**Figure 3.5b**). For solid electrolytes including polymer electrolytes and ion gels, it is possible to deposit metal gates on top of the electrolytes by evaporation or printing to form the top-gated geometry. Regardless of the gate position, this "electrolyte-on-semiconductor" structure suffers from large parasitic capacitance due to the overlap of the electrolyte and the source/drain electrodes.[133] In many reports, the source/drain electrodes are covered with an insulating layer (PMMA, SiO_2…) by additional lithography steps, so only the semiconducting channel is exposed to the electrolyte.[118,133,134]

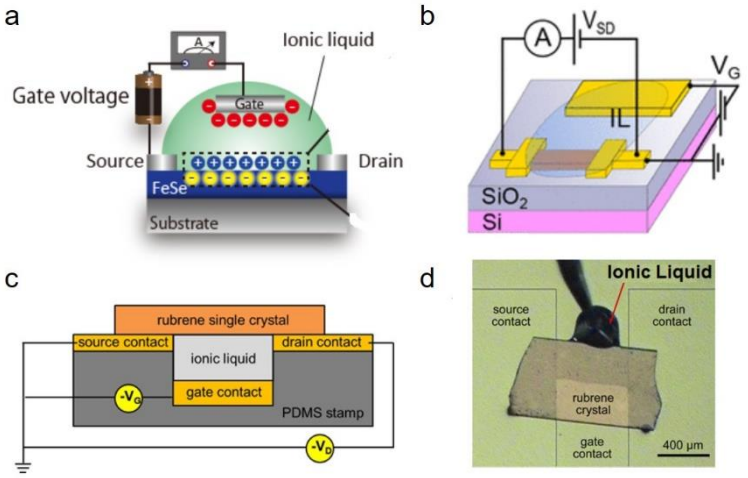

Figure 3.5 (a) Device architecture of a top-gated EGT.[135] (b) Device architecture of a side-gated EGT.[136] (c) Cross-sectional schematic of an IL-gated rubrene EGT.[137] (d) Top-view optical image of an IL-gated rubrene EGT.[138]

When performing electrolyte gating on single crystal OFETs, an alternative device geometry is usually adopted (**Figure 3.5c**).[138] This geometry is based on the air-gap geometry described in Chapter 2.3.2. After putting a drop of IL on the PDMS substrate, one can drag the IL drop to the edge of the crystal using a probe tip attached to a three-axis

micromanipulator. Owing to the capillary force, the air-gap is spontaneously filled with liquid once the liquid touches the crystal, and the air-gap transistor is converted into an EGT (**Figure 3.5d**). Using this method, comparisons of charge transport in the same crystal with and without the liquid electrolyte can be made. Another beneficial feature of this architecture is that the parasitic capacitance is minimized, since there is almost no contact between ILs and source/drain electrodes.

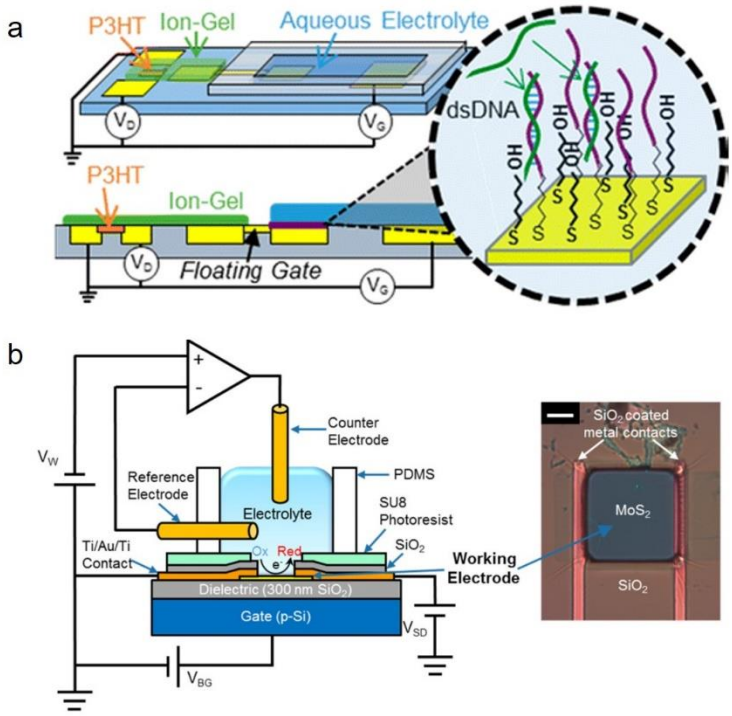

Figure 3.6 (a) The floating gate EGT geometry for detection of biomolecules.[139] (b) Dual-gated geometry for gate-modulated electrochemistry on surface of 2D semiconductor.[140]

The device geometries of EGTs discussed above can be slightly modified to integrate other functionalities. **Figure 3.6a** shows the use of side-gated EGTs as biosensors.[139] An extra floating gate, which is exposed to the solution of target molecules (DNA or proteins), is introduced into the EGT. When the target molecules bind to the floating gate, the EGT transducer can convert the binding event to an electrical signal, which is usually the shift of threshold voltage. Separating the binding chemistry from the working EGT channel

minimizing the contamination of the device. **Figure 3.6b** describes applying EGTs based on 2D materials in tuning the charge transfer process in electrochemistry.[140] Due to the ultrathin nature of 2D materials, the semiconducting channel can be gated from the bottom through oxide dielectric and from the top through electrolyte. Consequently, the band edges of 2D materials can be continuously tuned to get aligned with the target redox reactions, and the rate constant can be modified over orders of magnitude.

3.3.2 Extraction of charge density and mobility

In FETs with conventional dielectric materials, determination of charge density and mobility is straightforward. One only needs the dielectric constant and the thickness of the dielectric material to estimate the specific capacitance $C_i = \varepsilon_r\varepsilon_0/d$, and then calculate the charge density using $p = C_iV/e$. Simply plugging the charge density back into the *I-V* characteristics of the FET would give the mobility. For electrolytes, however, estimating charge density is not trivial and cannot be achieved using a simple formula. The capacitance of an electrolyte layer highly depends on both the operation frequency and the applied voltage. It is thus very important to extract charge density consistently and correctly. Otherwise, comparisons among experimental results from different devices and different groups become meaningless. Currently, four different methods have been used to determine charge density in EGTs: step-potential charging, AC impedance analysis, gate displacement current measurement, and Hall measurement.

Step-potential charging is the simplest way to estimate the equilibrium charge density in a static state. It involves changing the potential abruptly and measuring the charging (or discharging) current of the capacitor as a function of time (**Figure 3.7a**).[141] By integrating

charging current with respect to time, one can get the charge density if the area of capacitor (A) is known:

$$p = \frac{Q}{eA} = \frac{\int I \mathrm{d}t}{eA} \tag{3.1}$$

The decay of charging current is related to the RC time constant of the dielectric. For most electrolytes, the time constants are large, and the charging current should be measured over a long time (tens of minutes) until the current decays to a relatively flat plateau. The plateau is used as the integration baseline for charge density extraction, and physically represents the leakage current.

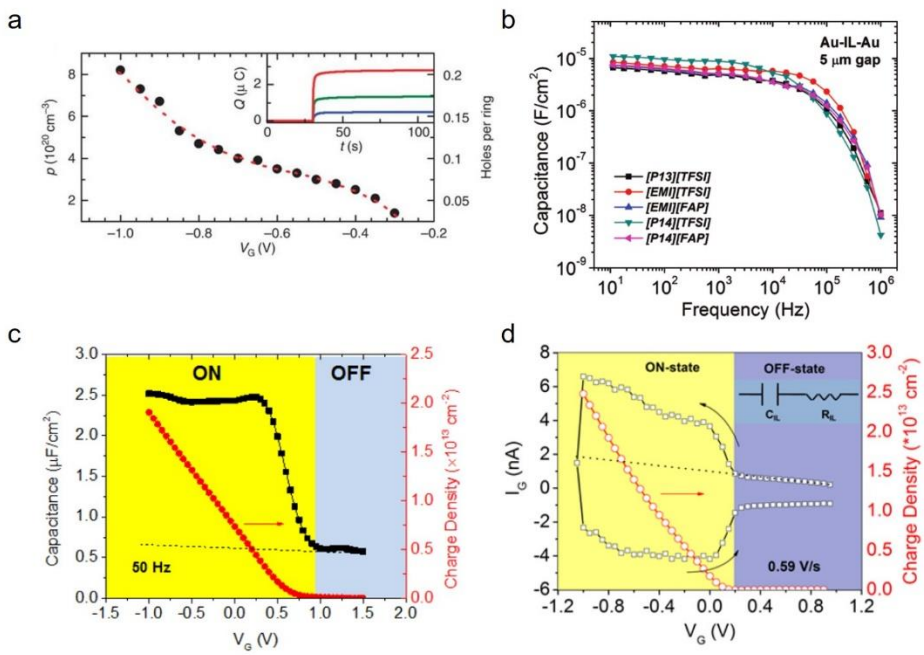

Figure 3.7 (a) Charge density of a P3HT EGT estimated from step-potential charging. Inset: integrated charge as a function of charging time.[141] (b) Typical capacitance-frequency (*C-f*) plots in the metal-electrolyte-metal structure for several ILs.[137] (c) A typical capacitance-voltage (*C-V*) plot and integrated charge density at 50 Hz in a rubrene EGT.[137] (d) A typical gate displacement current curve and integrated charge density in a rubrene EGT.[137]

AC impedance analysis is a powerful tool to assess the capacitance as a function of frequency (f) or voltage. In this experiment, a sine wave of oscillating voltage is

superimposed on a DC offset, the current response is evaluated, and the impedance is extracted. The total impedance (Z) contains a lot of information including the phase angle (ϕ), the resistance, and the capacitance. Typical C-f characteristics of ionic liquids are shown in **Figure 3.7b**.[137] The capacitance is large and weakly f-dependent at low frequencies but decreases at high frequencies. The roll off frequency of capacitance is related to the ionic mobility of the electrolyte and can be utilized to roughly estimate the time scale of EDL formation. If the electric field switches so quickly that the ions are pulled away before reaching the electrode surface, the EDLs cannot form. Therefore, only the low frequency capacitance represents the EDL capacitance. In a real EGT, C-V measurements can be performed at low frequency by grounding the source/drain contacts and apply voltages to the gate (**Figure 3.7c**).[137] Charge density is given by integrating specific capacitance versus gate voltage after subtracting the integration baseline:

$$p = \frac{\int C_i \mathrm{d}V_G}{e} \tag{3.2}$$

A V_G-dependent charge mobility is obtained by plugging p back into the transfer curves:

$$\mu = \frac{L}{W}\frac{I_D}{epV_D} \tag{3.3}$$

Gate displacement current measurement is a more rigorous approach, which has been extensively used to study the charge injection properties of OFETs with different dielectrics, including conventional solid dielectrics and electrolytes.[137,142,143] It is a quasi-static DC measurement and the gate sweep condition is similar to the condition when performing the transfer curve measurement on the same device. As a result, the charge density estimated from gate displacement current measurement is more reliable. In this method, the source/ drain electrodes are grounded, while the gate voltage is swept at

various rates and the gate displacement current is recorded. Technically, the gate displacement current can also be simultaneously measured along with the transfer curve, if the applied V_D is very small. The gate displacement current is related to the specific capacitance by:

$$I_G = \frac{dQ}{dt} \approx AC_i \frac{dV_G}{dt} \tag{3.4}$$

In a typical displacement current curve (**Figure 3.7d**), turn-on and turn-off of the EGT are clearly exhibited.[137] The forward (reverse) sweep corresponds to charge injection (retraction). After subtracting the baseline (the small current in the off-regime due to parasitic capacitance), the injected charge density is calculated by integrating gate displacement current with respect to gate voltage:

$$p = \frac{Q}{eA} = \frac{\int I_G \mathrm{d}V_G}{eA\frac{dV_G}{dt}} \tag{3.5}$$

The last method, *Hall effect measurement*, is the most accurate one for high performance EGTs, but is not applicable to all the materials. Details of charge density extraction using Hall effect measurements have been provided in Chapter 2.2.3. Special care has to be taken when using Hall effect measurements to determine charge densities in EGTs based on organic semiconductors.[85] As indicated in Chapter 2.2.3, only high mobility semiconductors can give robust, reliable Hall signals. Unfortunately, only 2 electrolyte-gated organic semiconductors, P3HT and rubrene, have been reported to exhibit the Hall effect, and the accuracy of the measured charge densities remains problematic (**Figure 3.8**).[141,144] In EGTs based on rubrene single crystals, the Hall mobility and charge density are more accurate when V_G is small, while the results from Hall measurements deviate from the FET results and are believed to be less reliable at larger V_G. In EGTs based on P3HT,

the Hall effect is heavily underdeveloped ($n_{Hall} >> n_{FET}$, $\mu_{Hall} << \mu_{FET}$) and the results have to be properly analyzed, although the observation of the Hall effect in an electrochemically doped polymer semiconductor is a remarkable achievement. Despite the limited universality, Hall effect measurement is still a powerful way to get charge density and mobility in most inorganic-based EGTs.

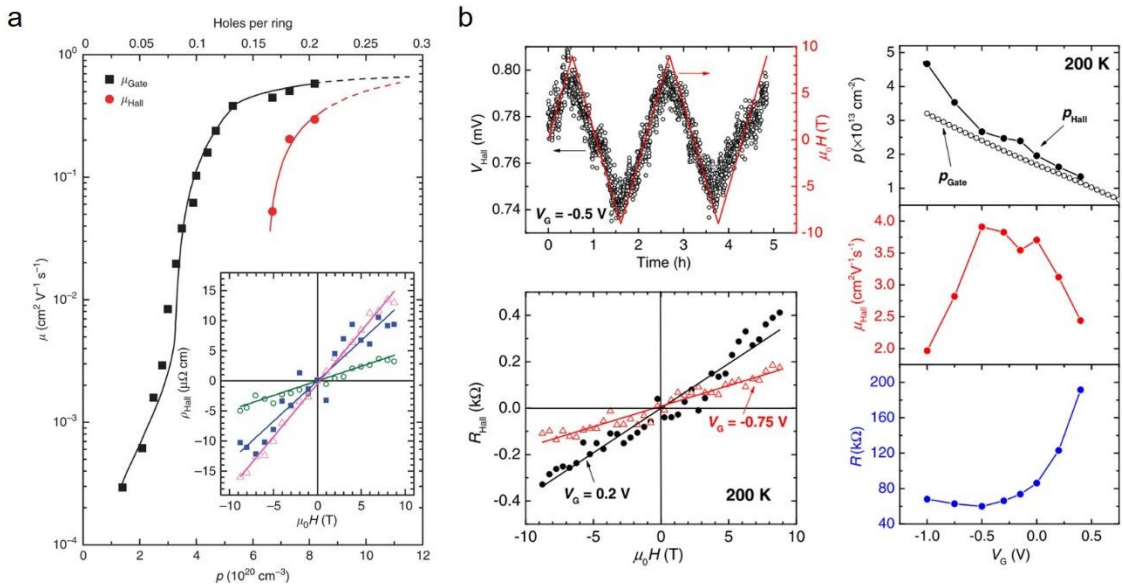

Figure 3.8 (a) Charge density dependence of mobility in a P3HT EGT extracted from step-potential charging and from Hall measurements. Inset: Hall resistivity versus magnetic field for the same device.[141] (b) Top left: Hall voltage and field as a function of time in a rubrene EGT. Bottom left: Hall resistance versus field for the same device. Right: charge density, mobility, and resistance as a function of V_G.[144]

3.4 Charge transport in EGTs

The importance of charge density cannot be emphasized enough. Besides controlling the conductivity of the semiconductor so that the transistor can be turned on or off, tuning transitions among different electronics phases is also possible by changing the charge density. **Figure 3.9** summarizes the electronic ground states of several prototype inorganic and organic materials as a function of charge density.[97,145] It is obvious that most of those interesting phenomena occur at charge densities above 10^{13} cm^{-2}. Such charge densities are

virtually impossible to achieve in conventional FETs but can be accumulated using electrolyte gating. The ultrahigh charge density induced by electrolyte gating has led to the observation of novel gate-tunable phenomena, including but not limited to insulator−metal transitions, superconductivity, ferromagnetism, and ambipolar transport, in a variety of materials.

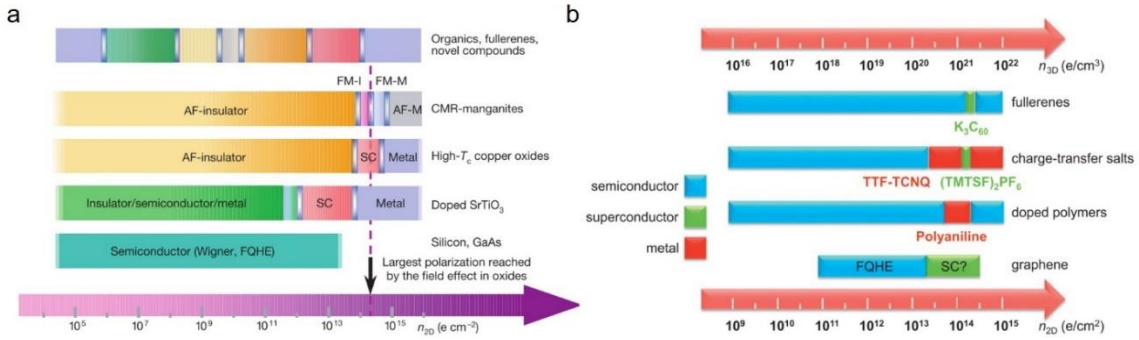

Figure 3.9 (a) Illustration of the zero-temperature ground states of various inorganic materials as a function of charge density.[145] (b) Illustration of the zero-temperature ground states of various organic materials as a function of charge density.[97] Note: AF, antiferromagnetic; FM, ferromagnetic; I, insulator; M, metal; SC, superconductor; FQHE, fractional quantum Hall effect; Wigner, Wigner crystal.

3.4.1 Insulator–metal transition

The first breakthrough in electrolyte-gate-tunable phase transitions was the observation of insulator–metal transition in ZnO EDLTs by Shimotani *et al.* in 2007 (**Figure 3.10a**).[146] By gating highly crystalline epitaxial ZnO films with polymer electrolyte $KClO_4$ /PEO, charge densities up to $4.2*10^{13}$ cm^{-2} (determined by Hall measurement) can accumulate at the ZnO surface, and the resistance–temperature (*R*–*T*) characteristics become *T*-independent at large V_G, demonstrating the gate-induced insulator–metal transition. By replacing the polymer electrolyte with ILs and applying V_G at low temperatures, accumulation of charge carriers as high as $8*10^{14}$ cm^{-2} can be achieved in ZnO.[98] Inspired by the success in ZnO, electrolyte gating has been applied to a broad range of materials,

including correlated oxides,[101,147–151] 2D materials,[120,134,152,153] and topological insulators,[154] to pursue insulator–metal transition.

In addition to EDLTs, ECTs based on several inorganic materials also exhibit insulator-metal transition. Although crystalline oxide films are thought to be impermeable to ions in ILs, electrochemical doping still exists in certain materials. Among these materials, VO_2 is a particularly interesting one, because an insulator–metal transition caused by electrolyte gating was found to be accompanied by charge delocalization over the bulk, which is contradictory to the assumption of 2D electrostatic doping.[148] The formation of metallic state in VO_2 was later proved to be oxygen-sensitive, which suggests that charge accumulation occurs through the formation of oxygen vacancies when a positive V_G is applied (**Figure 3.10b**).[101] The diffusion length of oxygen vacancies can be larger than the electronic screening length, so doping in VO_2 is no longer limited to the VO_2/IL interface, but is actually a 3D electrochemical doping. Similar suppression of insulator-metal transition in oxygen environment has been observed in other oxides such as TiO_2.[155]

Compared with inorganic counterparts, realization of insulator–metal transition in electrolyte-gated organic semiconductors remains elusive. Efforts have been made in benchmark small molecule semiconductor rubrene and polymer semiconductor P3HT.[141,144,156] In rubrene EGTs, maximum charge density of 0.33 charge per molecule ($6.3*10^{13}$ cm^{-2}) has been reached using ionic liquid [P14][FAP] (**Figure 3.10c**). The mobility of IL-gated rubrene, however, is only 2-3 $cm^2V^{-1}s^{-1}$ at room temperature, much smaller than the air-gap mobility (~15 $cm^2V^{-1}s^{-1}$). Remarkably, poorly understood conductance peaks have been observed in transfer curves, where the conductance decreases at the highest V_G magnitudes. Near the conductance peak, the resistance decreases upon

cooling to as low as 120 K, reaching within a factor of 2 of h/e^2, which is close to a 2D insulator–metal transition. At higher charge densities, reentrance of a strongly insulating regime indicates the existence of interfacial electronic disorder such as ion-charge binding interaction. In P3HT, the absence of insulator–metal transition at extremely high hole densities (~10^{21} cm^{-3}) suggests that similar doping-induced electronic disorder limits charge transport. In order to obtain a truly metallic state in organic semiconductors, the influence of these limiting factors needs to be understood and mitigated.

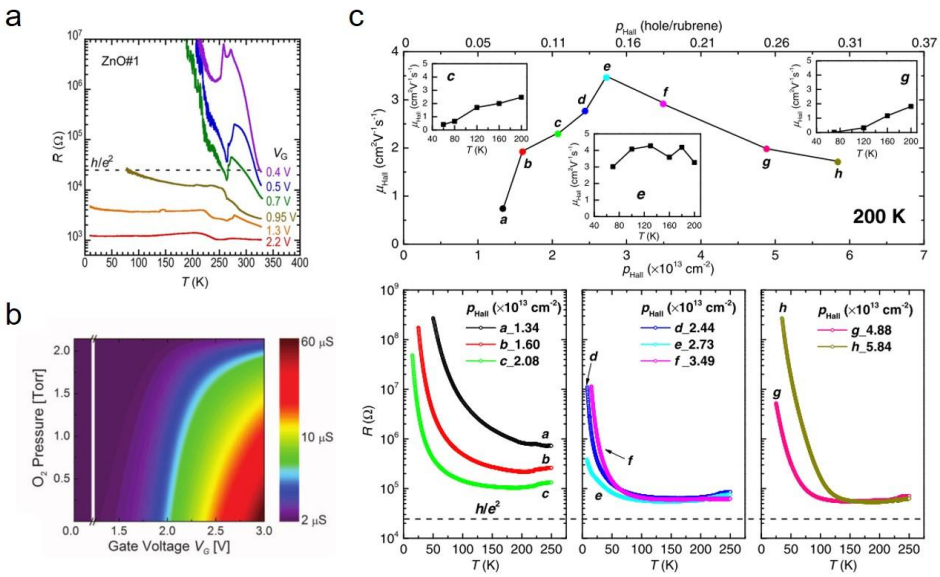

Figure 3.10 (a) Insulator–metal transition in electrolyte-gated ZnO.[146] (b) Sheet conductance of a VO_2 EGT as a function of V_G and oxygen pressure.[101] (c) Resistance versus temperature plots of a rubrene EGT at different charge densities.[144]

3.4.2 Superconductivity

Electrolyte-gate-induced superconductivity was first observed in $SrTiO_3$ (STO) in 2008.[118] Pristine STO is a well-known highly resistive insulator, which is widely used as a growth substrate for oxide films. When fabricated into EDLTs, STO crystals can be electron-doped at positive V_G, and the resistance begins to decrease with decreasing temperature at charge densities over 10^{13} cm^{-2}, similar to the observation of insulator–metal

transition in ZnO. Further cooled down to sub-1K using a dilution refrigerator, the device exhibits superconductivity with a critical temperature (*Tc*) of 0.4 K (**Figure 3.11a**). The induced superconductivity can be confirmed by the observation of critical field and critical current. Motivated by this achievement, electrolyte-gate-induced superconductivity has been reported in many materials, including the extensively studied Cu-based and Fe-based superconductors[124,135,157–159] and van der Waals layered materials.[102,160–164] Phase diagrams of *Tc* versus charge density have been built for several materials, many of which exhibit a dome-like shape with a maximum *Tc* at an optimal charge density (**Figure 3.11b**). Intriguingly, the dome-like phase diagram is similar to those observed in chemically doped Cu-based and Fe-based superconductors.

In some materials, purely electrostatic doping cannot lead to the realization of superconductivity. Instead, superconductivity is induced by electrochemical doping. One example is $MoTe_2$, which does not show superconductivity in EDLT architecture, but has a *Tc* of 2.8 K after K^+ intercalation.[102] The origin of intercalation-induced superconductivity is the ultrahigh electrochemical doping level (charge density over 10^{15} cm^{-2}), one order of magnitude higher than the maximum charge density achieved by electrostatic doping. Similar intercalation-induced superconductivity has also been observed in WS_2 and TaS_2.[163] In addition to metal ion intercalation, electrochemical etching was found to increase the *Tc* of the famous Fe-based superconductor FeSe from 8 K to 40 K.[135] These observations indicate that electrochemistry can be as powerful as electrostatics when exploiting novel physical phenomena in EGTs.

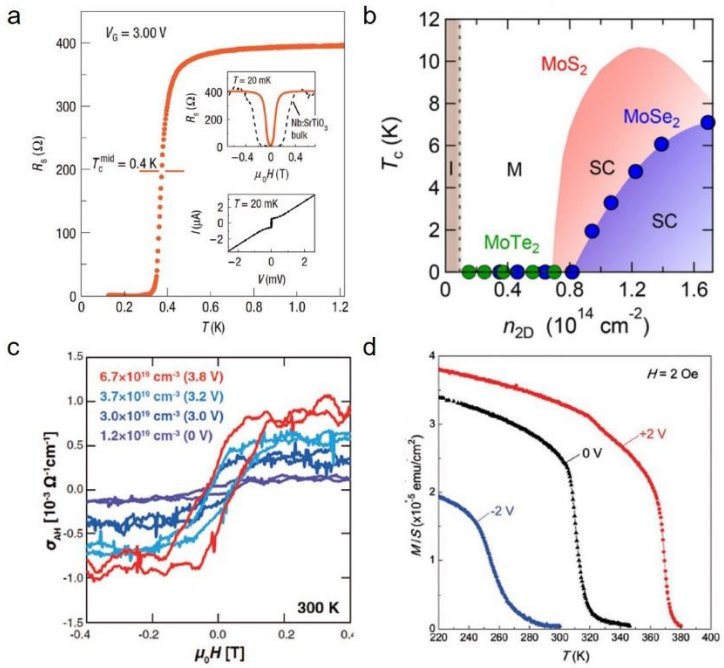

Figure 3.11 (a) Gate-induced superconductivity in STO. Inset: magnetoresistance and *I*–*V* characteristic in the superconducting state.[118] (b) Critical temperature versus charge density phase diagram of electron-doped MoS_2, $MoSe_2$, and $MoTe_2$.[102] (c) Gate-induced ferromagnetism in $Ti_{1-x}Co_xO_2$.[165] (d) Temperature dependence of magnetization in electrolyte-gated Co at different V_G.[166]

3.4.3 Ferromagnetism

Manipulating the magnetic properties of materials, which has been realized in several ferromagnetic oxides, can be achieved by shifting the Fermi level via electrolyte gating to tune the density and type of charge carriers. Due to the high charge densities accumulated by electrolyte gating, the Curie temperatures can be shifted over 150 K in ferromagnetic oxides such as $La_{0.5}Sr_{0.5}CoO_3$.[167,168] Room temperature gate-tunable ferromagnetism has also been observed in a magnetic semiconductor $Ti_{1-x}Co_xO_2$, as confirmed by gate-tunable anomalous Hall effect (**Figure 3.11c**).[165] The same strategy can be applied in controlling the magnetic properties of magnetic metals as well. Due to the high density of free charge carriers in metals, the electric field is heavily screened, and the field-effect is only limited near the surfaces of metals. Therefore, only ultrathin metal films can be used for electrolyte

gating. Nevertheless, EGTs are still capable of tuning the magnetic properties of several metal films including FePt and Co.[166,169] Remarkably, the Curie temperature of ultrathin Co film can be tuned over a range of 100 K with a V_G range of ±2 V (**Figure 3.11d**).[166] In addition to controlling the properties of magnetic materials, another interesting research direction is to make non-magnetic metals magnetic. By using paramagnetic IL [BMIM][$FeCl_4$] to gate Pt film, a clear anomalous Hall effect was observed by Liang *et al*., demonstrating the induced ferromagnetism in Pt.[170] This experiment highlights the use of paramagnetic ILs for switching on/off magnetic states.

3.4.4 Ambipolar transport

In conventional FETs based on many semiconductors, only unipolar behavior has been observed due to the large injection barrier and/or high trap density for minority charge carriers. The rise of electrolyte gating has promoted the recovery of ambipolar transport in certain semiconductors. Accumulation of high charge density fills the traps and reduces the threshold voltage for minority carrier accumulation. Moreover, the strong electric field at the semiconductor/electrolyte interface improves the injection of minority carriers despite the large energy mismatch between the semiconductor bands and metal work functions. The first ambipolar EGT was fabricated using carbon nanotube and polymer electrolytes in 2004.[114] Following this achievement, ambipolar transport has been demonstrated in EGTs based on other materials, including colloidal quantum dots,[171–173] 2D materials,[102,134,162,174–176] and organic single crystals.[177,178] It is worth noting that even those organic semiconductors with large band gaps (e.g., rubrene) can exhibit ambipolar behavior when gated with ion gels, indicating the gating power of EGTs (**Figure 3.12a**).[177]

The application of electrolyte gating in ambipolar devices significantly reduces the threshold voltage for both hole and electron accumulation. Importantly, in many EGTs, the threshold voltage is only affected by the edge of conduction band or valence band. As a result, a new method to probe the band gaps of ambipolar semiconductors has been proposed, where the magnitude of band gap is quantitatively given by the difference between the threshold voltages of p-type and n-type operation (**Figure 3.12b**).[174] This method produces consistent results and has been applied to many 2D materials whose band gaps are difficult to measure by other techniques.

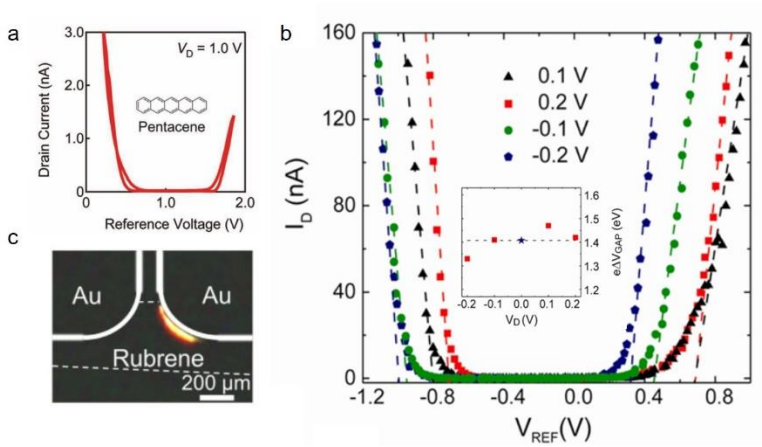

Figure 3.12 (a) Ambipolar transport in ion-gel-gated pentacene single crystals.[177] (b) Ambipolar transport in IL-gated WS_2. Inset: extracted band gap at different V_D.[174] (c) Light-emission in ion-gel-gated rubrene single crystals.[178]

Another feature of ambipolar transistors is the formation of lateral p–n junctions and the possibility of light emission by charge injection and recombination. This type of device is called light-emitting transistors (LETs), which combines the switching and light-emitting capabilities (**Figure 3.12c**).[178,179] The recombination of holes and electrons can be spatially controlled by the applied gate voltage. Consequently, the light emission zone becomes gate-tunable, and can be directly observed due to the planar geometry of the EGT. Among all those reports of LETs based on organic semiconductors, carbon nanotubes and 2D

materials, a particularly interesting one is the observation of circularly polarized light emission in WSe_2 EGTs, due to the unique band structure of monolayer WSe_2 with the valley degree of freedom.[180]

3.4.5 Other interesting phenomena

Recently, EGTs have been found to be a powerful tool to find and optimize thermoelectric materials. The thermoelectric performance is characterized by the figure of merit, $ZT = S^2\sigma T/\kappa$, where S and κ represent the Seebeck coefficient and the thermal conductivity. In semiconductors, S and σ have opposite dependence of charge density, so the ZT value reaches its maximum at a certain charge density. Thanks to the continuous and wide-range charge accumulation capability, electrolyte gating provides a unique platform for the optimization of thermoelectric performance. Using the device geometry shown in **Figure 3.13a**, charge transport and the Seebeck effect can be simultaneously measured in the same EGT.[181] Thermoelectric properties of several semiconductors, including metal oxides,[181–183] transition-metal chalcogenides,[184] and carbon nanotubes,[185,186] have been investigated using electrolyte gating. For example, WSe_2 EGTs exhibit larger ZT compared with chemically doped bulk WSe_2; the ZT value can also be optimized in EGTs due to the continuous tuning of charge accumulation, while in bulk WSe_2 the ZT value has a weak charge density dependence.[184] The advantages of electrolyte gating over chemical doping are therefore demonstrated.

Electrolyte gating can lead to not only electronic phase transitions mentioned earlier, but also structural phase transitions in certain materials. The crystal structure of a 2D material, $MoTe_2$, can be tuned between a semiconducting, hexagonal phase (2H phase) and a metallic, monoclinic phase (1T' phase), when electron densities over 10^{14} cm^{-2} are induced

by electrolyte gating. The phase transition is directed confirmed by Raman spectroscopy while sweeping V_G and is found to be reversible and purely charging-induced (**Figure 3.13b**).[187] Although the mechanism is still controversial, this achievement indicates the potential of electrolyte gating as a platform for studying the competition between different structural ordering. It might be worth trying to apply this technique in other materials, in which similar charging-induced structural phase transitions have been theoretically proposed.

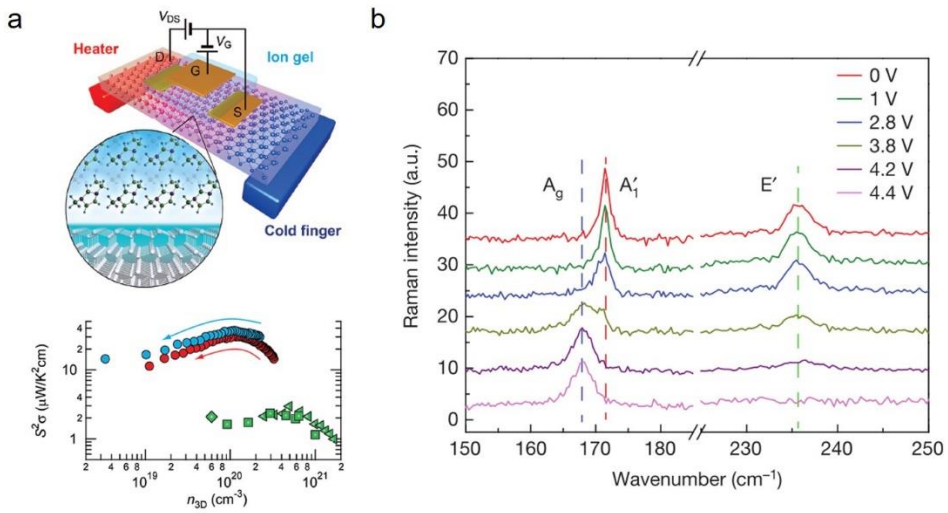

Figure 3.13 (a) Top: Schematic of EGT structure for thermoelectric measurements.[181] Bottom: Dependence of the power factor $S^2\sigma$ in WSe_2 on charge density for EDLTs (red and blue) and bulk-doped samples (green).[184] (b) Raman spectra before, during and after the phase transition of WTe_2 as V_G increases.[187]

Chapter 4 Experimental Methods

4.1 Crystal growth

All the organic crystals in this work are grown by the PVT method described in Chapter 2.3.1. The experimental setup in the Frisbie lab is shown in **Figure 4.1**. Two Pyrex tubes are used as the insulation tube and the gas flow tube, and a quartz tube is used as the crystal growth tube. Powders of source materials are placed in a quartz boat and placed closed to one end of the growth tube. Nichrome resistance wire is wrapped outside the gas flow tube for global heating, while heating tape is wrapped around the insulation tube near the source material to generate the temperature gradient. The heating power is controlled by two Variac variable transformers. To monitor the temperature gradient, two thermal couples are taped near the source material and near the growth zone. Ultrapure Ar is used as the carrier gas.

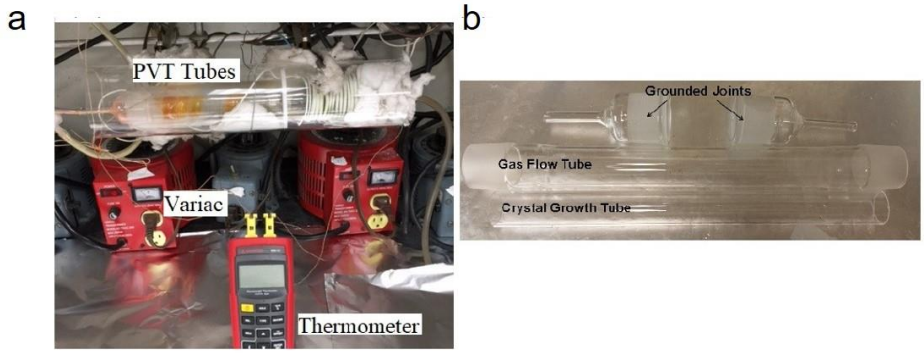

Figure 4.1 (a) Photograph of PVT growth setup including PVT tubes, thermometer, and Variacs. (b) Photograph of glassware used in PVT setup (the insulation tube is not shown).

The growth conditions are obtained empirically. In the Frisbie lab, high quality rubrene single crystals (**Figure 4.2a**) can be grown under the following conditions. Thick crystals (> 10 μm) are obtained after several days at source temperatures of 280-290 °C; thin crystals (< 1 μm) are obtained after 30-60 min at source temperatures of 300-310 °C. The

temperature of the crystal growth zone needs to be maintained at below 250 °C. The gas flow rate should be 10-100 sccm depending on the desired crystals. If the gas flow is too large, the obtained crystals usually have very bad quality.

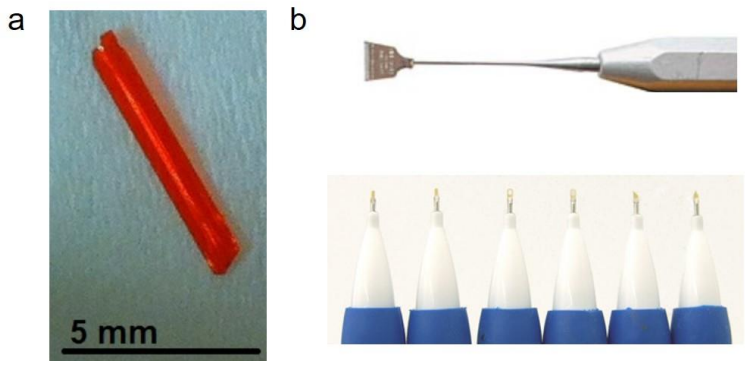

Figure 4.2 (a) Photograph of a PVT-grown rubrene crystal. (b) Tools used to handle rubrene crystals: Ted Pella Micro-Scale (top) and MiTeGen Microtools™ (bottom).

Handling the crystals can be very challenging for beginners. A very steady hand is always required when working with these tiny crystals. Using sharp tools such as tweezers will damage the crystals, so it is better to pick up the crystals electrostatically. Thick crystals can be gently picked up by the small metal tool shown in **Figure 4.2b** and are relatively easy to handle since they are mechanically robust. Thin crystals, however, are more brittle and flexible, so one needs to be extremely careful when working with thin crystals. The tools used to handle thin crystals are MiTeGen Microtools™, which have tips made from soft, flexible polymer films. The polymer tip should be moved slowly towards the target thin crystal, and the electrostatic force will stick the thin crystal and the tip together. When transferring the crystal to the target substrate, one should carefully align the crystal above the desired position under the microscope, tilt and lower down the crystal so that one end of the crystal touches the substrate and sticks to it, and slowly release the handling tool. In most cases, the crystal will spontaneously adhere to the substrate.

4.2 Structural characterization

The single crystallinity of crystals grown is first examined by X-ray diffraction (XRD). The equipment used for XRD is PANalytical X'pert Pro with Cu Kα radiation (wavelength 0.154 nm). Out-of-plane wide angle 2θ-ω scan of a typical rubrene single crystal is shown in **Figure 4.3a**. Since large rubrene crystals are usually plate-like and the largest face corresponds to the *ab*-plane, (00L) planes are probed by 2θ-ω scan. It is obvious that only (002) family of peaks appear in the XRD pattern, and all the peaks have narrow peak width and match the predicted positions. The single crystallinity is further confirmed by in-plane XRD (also known as ϕ scan) of the {200} peaks. The multiplicity of {200} is 2, so 2 peaks separated by 180° should be obtained for a single crystal, which is exactly what is shown in **Figure 4.3b**.

The surface morphology of the obtained crystals can be characterized by atomic force microscopy (AFM). **Figure 4.3c** is a tapping mode AFM image of a rubrene crystal. A series of molecular steps are observed, and the step height matches the intermolecular distance along the *c*-axis of the rubrene unit cell. Within a terrace, the surface roughness is very small, demonstrating the molecularly flat nature of rubrene single crystals. Extra information of surface potential can be given by scanning Kelvin probe microscopy (SKPM), which is able to detect electronic disorder at the surface of crystals.[35,188,189] Surface potential variations correspond to traps or barriers in HOMO/LUMO bands, which can limit charge transport. For high quality rubrene crystals, usually negligible roughness is observed in SKPM images (**Figure 4.3d**).

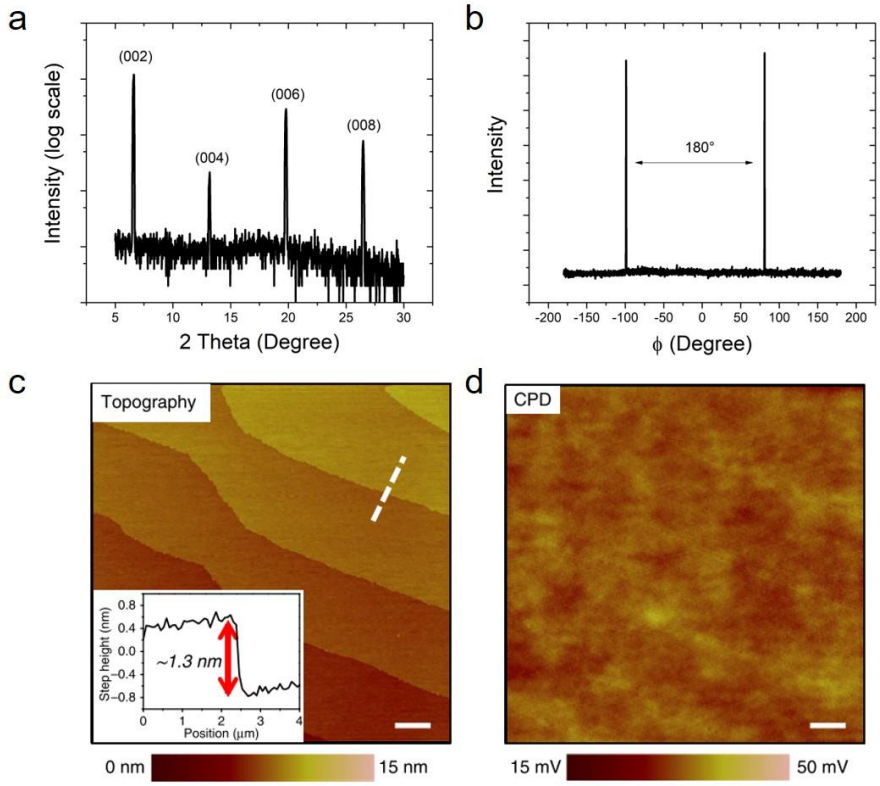

Figure 4.3 (a) Out-of-plane wide angle XRD pattern of a rubrene single crystal. (b) In-plane ϕ scan of the {200} peaks. (c) Topography of a rubrene single crystal with typical terrace structure. Inset: height profile along the dashed line. (d) Surface potential image obtained simultaneously with topography by SKPM.[188]

4.3 Device fabrication

<u>Fabrication of PDMS-based devices</u>

1. A clean environment is strongly recommended for the whole process.
2. Draw the photomask with desired electrode patterns using a program like AutoCAD. The areas covered with chrome will be the raised regions in the PDMS obtained.
3. Fabricate the master wafer using the following procedures:
    - Clean the wafer in piranha solution (H_2SO_4:H_2O_2) for 10 min. Rinse with DI water and blow dry with N_2.
    - Pre-bake at 105 °C for 1 min.
    - Spin coat SU8-2005 photoresist for 30 s, 2500 rpm (~5 μm in thickness).
    - Soft bake at 95 °C for 2 min.

- Exposure (total dose needed is 105 mJ/cm^2, soft contact, gap 25 μm, expose for 9 s if using the Karl Suss MA-6 contact aligner with 12 mJ/cm^2 lamp intensity).
- Post-exposure bake at 95 °C for 3 min.
- Develop with SU8 developer for 50 ~ 55 s.
- Rinse with IPA for 2 mins and blow dry with N_2.
- Hard bake at 150 °C for 5 min.

4. Check the thickness of the air-gap using surface profilometry.
5. Make the PDMS stamp using the following procedures:
    - Put the master wafer in a clean petri-dish with the patterned side facing up.
    - Mix (stir > 5 min) PDMS prepolymer (Sylgard 184, Dow Corning) and curing agent with a weight ratio of 10:1. Fill the mixture into the petri-dish. The thickness of the PDMS stamp is determined by the amount of PDMS.
    - Degas in a vacuum chamber overnight. Make sure that the petri-dish is placed in a flat position.
    - Bake in oven at 80 ˚C for 3 h.
    - Carefully take out the PDMS stamp and peel it from the surface of the master wafer.
6. Put Scotch tape onto the patterned surface of PDMS stamp to emboss the patterns.
7. Cut the PDMS stamp into smaller stamps with individual device patterns using a razor blade. Clean the back side of PDMS stamps with Scotch tape and gently put them on pre-cleaned glass slides (cleaned with Scotch tape). The PDMS will stick to the glass spontaneously.
8. Remove Scotch tape from the surface of PDMS stamps before evaporation.
9. Evaporate Cr/Au (3/17 nm) with a rate of 0.1 nm/s using an e-beam evaporator.
10. Leave the metalized PDMS in the air for at least 1 month. **Note**: this step is critical for fabricating high performance devices, since devices fabricated on fresh PDMS exhibit severe contact problems and performance degradation.
11. To fabricate an air-gap transistor, carefully laminate a single crystal across the source/drain electrodes under a microscope. To achieve good lamination, the PDMS substrate must be dust free and the surface of the crystal must be very smooth.
12. To fabricate a liquid-gated transistor, after Step 11, put a drop of liquid dielectric on the PDMS substrate using a needle. Load the device into the probe station chamber. Use the tip of a probe to drag the liquid towards the crystal. Once the liquid touches the crystal, it will spontaneously fill the air-gap due to the capillary force.
13. To fabricate a metal-insulator-metal capacitor, just replace the semiconductor crystal with a piece of conducting substrate (ITO glass or Au-coated Si wafer).

<u>Sample preparation for Hall effect and *R*–*T* measurements</u>

1. Fabricate a device according to the previous description. Pre-test the transistor performance in the probe station.

2. Put a small amount of GE Varnish adhesive on the sample puck for Physical Property Measurement System (PPMS, Quantum Design). Quickly put the device on the sample puck. Wait for 2-3 min to cure the GE Varnish.
3. Prepare the materials for wire-bonding. Cut Au wire (25 µm or 50 µm diameter) into smaller pieces (~1 cm long). Mix the part A and B of solvent-free Ag epoxy (Chemtronics CW2400) with a ratio of 1:1. **Note:** The use of solvent-free Ag epoxy is critical for the success of *R*–*T* measurements at very low temperatures (< 50 K). If solvent-based Ag paint (e.g., Leitsilber 200 conductive Ag paint) is used, the adhesion between the Ag pad and the PDMS substrate is not strong enough, so the Ag pad may be detached due to the contraction of PDMS during cooling.
4. Use a sharpened wooden stick to put a small amount of Ag epoxy onto the electrode region of the PDMS substrate.
5. Use a pair of tweezers to insert one end of a Au wire into the Ag epoxy on PDMS. Adjust the position of the other end of the Au wire to make sure that it is roughly above a bonding pad on the sample puck.
6. Repeat Steps 4 and 5 for all the electrodes.
7. Leave the sample puck with the device in a glovebox overnight to cure the Ag epoxy.
8. Connect the Au wires to the bonding pads using Ag paint (Leitsilber 200). Ag paint is used here because it sticks well to rigid metal pads and it can be easily removed after measurements.
9. Load the sample puck into the PPMS to start measurements.

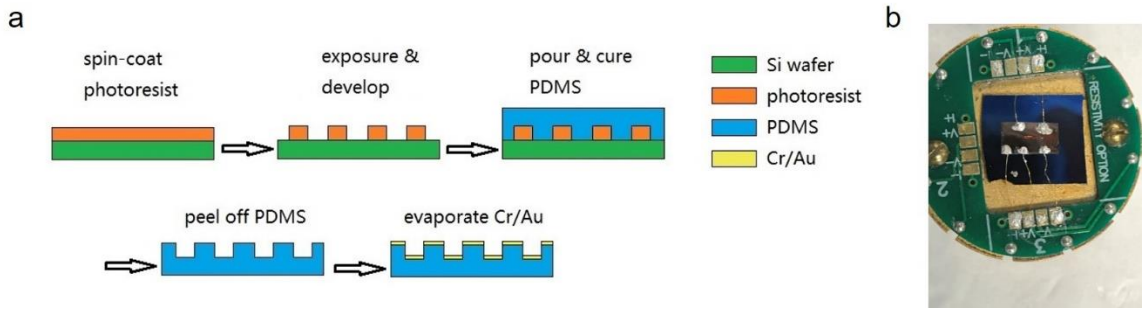

Figure 4.4 (a) Schematic cartoons of fabrication steps for Au-coated PDMS substrates. (b) Photograph of a rubrene EGT wire-bonded to the PPMS sample puck.

4.4 Electrical characterization

Most of the electrical measurements of single crystal OFETs are carried out in a cryogenic probe station (Lakeshore Desert Cryogenics) located in a glovebox filled with N_2. Transistor *I*-*V* measurements are taken using a variety of Keithley source-measure units (SMUs) and multimeters (236, 237, 6517A, 2612). A Lakeshore 331 temperature controller

is used for variable temperature measurements. Hall effect and *R*–*T* measurements are made in a Quantum Design PPMS with a 9 T superconducting magnet. A Keithley 220 current source is used to source the current, a Keithley 2400 SMU is used to apply the gate voltage, and a Keithley 2002 multimeter is used to measure the Hall voltage or the 4-probe voltage.

Figure 4.5 Photograph of equipment used in this study. (a) Cryogenic probe station. (b) Keithley SMUs and multimeters. (c) Quantum Design PPMS.

Chapter 5 Negative Isotope Effect on Field-effect Hole Transport in Fully Substituted ^{13}C-Rubrene

Isotopic substitution is a useful method to study the influence of nuclear motion on the kinetics of charge transport in semiconductors. However, in organic semiconductors, no observable isotope effect on field-effect mobility has been reported. To understand the charge transport mechanism in rubrene, the benchmark organic semiconductor, we have synthesized and characterized crystals of fully isotopically substituted rubrene, ^{13}C-rubrene ($^{13}C_{42}H_{28}$). Vapor-grown ^{13}C-rubrene single crystals have the same crystal structure and quality as native rubrene crystals (i.e., rubrene with a natural abundance of carbon isotopes). The characteristic transport signatures of rubrene, including room temperature hole mobility over 10 $cm^2V^{-1}s^{-1}$, intrinsic band-like transport, and clear Hall behavior in the accumulation layer of air-gap transistors, are also observed for ^{13}C-rubrene crystals. The field-effect mobility distributions based on 74 rubrene and ^{13}C-rubrene devices, respectively, reveal that ^{13}C isotopic substitution produces a 13% reduction in the hole mobility of rubrene. The origin of the negative isotope effect is linked to the red-shift of vibrational frequencies after ^{13}C-substitution, as demonstrated by computer simulations based on the transient localization (dynamic disorder) scenario. Overall, the data and analysis provide an important benchmark for ongoing efforts to understand transport in ordered organic semiconductors. This work has been published as *X. Ren, M. J. Bruzek, D. A. Hanifi, A. Schulzetenberg, Y. Wu, C. Kim, Z. Zhang, J. E. Johns, A. Salleo, S. Fratini, A. Troisi, C. J. Douglas, and C. D. Frisbie, "Negative Isotope Effect on Field-Effect Hole Transport in Fully Substituted ^{13}C-Rubrene", Advanced Electronic Materials, 2017, 3, 1700018*.

5.1 Introduction

The intrinsic transport properties of organic semiconductors are naturally best investigated in single crystals due to the generally low level of static disorder in these samples.[5–7,190] Field-effect transport measurements on crystals of the benchmark organic semiconductor rubrene ($C_{42}H_{28}$, 532.7 g/mol), in particular, have been pivotal for organic electronics as they have revealed the simultaneous presence of both high room temperature hole mobility above 10 $cm^2V^{-1}s^{-1}$,[88] and, crucially, a negative temperature exponent for the mobility, i.e., mobility increases as temperature decreases down to about 180 K.[8] These observations and others, including mobility anisotropy[90,91] and a robust Hall effect,[9,59] are strong evidence for band-like transport in rubrene (bandwidth ~0.5 eV),[191] where many features of classical band transport are observed. However, the estimated carrier mean free paths remain on the order of the unit cell dimension (~1 nm), thus precluding the typical band picture in conventional semiconductors.

The precise nature of band-like transport in organic semiconductor crystals is still being explored.[10] Currently, a consistent picture of charge transport in high mobility crystals is offered by the dynamic disorder model (DDM, also known as transient localization), in which the carrier transient localization length l_{loc} and the propagation rate ω are determined by a competition between intermolecular electronic coupling and charge-phonon interaction; in this scenario the carrier mobility μ can be evaluated as:[44]

$$\mu = \frac{e}{k_B T} l_{loc}^2 \omega \tag{5.1}$$

Here, ω^{-1} can be viewed as the characteristic time that charge is transiently localized due to the lattice dynamics, and it is set by the predominant low frequency intermolecular

modes that modulate the intermolecular electronic coupling; l_{loc} is the length that charge can spread within the characteristic time ω^{-1}, and is limited by the dynamic disorder as well as the intermolecular transfer integral. l_{loc} decreases with temperature because higher temperatures lead to higher degrees of dynamic disorder, reducing intermolecular coupling. Indeed, the degree to which low frequency vibrations modify charge-transfer integrals was recently investigated by thermal diffuse electron diffraction scattering in crystalline TIPS-pentacene, combined with quantum chemical calculations, and it was shown that intermolecular coupling can change by over 100% relative to equilibrium values.[38]

The high hole mobility in orthorhombic crystalline rubrene is generally attributed to the large intermolecular transfer integrals (few tenths of eV) together with a relatively weak coupling of the charge carriers to the relevant intermolecular vibrations, both enhancing l_{loc} (~5 nm at room temperature).[14,40,43] Further, the expectation from DDM is that increasing (decreasing) the frequency of lattice phonons will increase (decrease) the charge mobility because the charge remains localized for shorter (longer) periods of time, i.e. ideally $\mu \sim \omega$.[44] For rubrene, 100% substitution of the ^{13}C isotope into the molecular structure produces an ~8% increase in molecular mass, which can be anticipated to produce a ~4% decrease in intermolecular vibrational frequency and thus a comparable decrease in charge mobility. In contrast, a true band transport system dominated by acoustic phonon scattering has no isotope effect on mobility.[192] Thus, the study of isotopically labeled organic semiconductors with identical electronic structures but changed molecular masses offers the opportunity to confirm expectations of DDM. Furthermore, although isotopic substitution was introduced into organic electronics in the 1970s, largely in conjunction with time-of-flight mobility measurements, the conclusions of these earlier experiments

were mixed, with reports of both positive and negative isotope effects for very similar systems.[193–199] Thus, the opportunity to clarify the nature of the kinetic isotopic effect in crystalline organic semiconductors provides an additional motivation. It is worth noting that Shuai and others have suggested that nuclear tunneling may play a role in charge transport of carbon-based materials, and their hopping model also predicts a significant negative isotope effect on charge mobility upon ^{13}C-substitution.[192,200] Such a hopping model, which is based on a modified Marcus picture, is however only strictly valid in the narrow-band limit, which does not apply to rubrene.

Here we report our experimental and theoretical investigations of field-effect transport in ^{13}C-rubrene ($^{13}C_{42}H_{28}$, 574 g/mol) single crystals. We synthesized ^{13}C-rubrene, grew the single crystals from the vapor phase, and performed structural and electrical characterizations. The results confirm that the crystal structure of ^{13}C-rubrene is identical to native rubrene. We find a surprisingly significant negative isotope effect of –13% on the mobility, which is consistent with DDM, though the effect is somewhat larger than DDM simulations predict.[40] Importantly, our results also demonstrate definitively that semi-classical band transport is not the transport mechanism in rubrene. To the best of our knowledge, this is the first report of a negative isotope effect on field-effect charge transport in an organic semiconductor and the data provide an important benchmark for ongoing theoretical investigations of the properties of organic semiconductors.

5.2 Structural and electrical characterization

The detailed synthetic route to ^{13}C-rubrene can be found somewhere else.[37] Single crystals were grown by the horizontal physical vapor transport (PVT) method. XRD and AFM were used to examine the quality of the crystals. **Figure 5.1a** displays the wide-angle

diffraction patterns for ^{13}C-rubrene and native rubrene single crystals. All the diffraction peaks observed correspond to the family of (002) planes. In a direct comparison between the peaks from ^{13}C-rubrene and native rubrene single crystals, we can see that the positions of corresponding (hkl) peaks are almost identical, which implies that they share the same crystal structure and lattice constant. Moreover, AFM height images (**Figure 5.1b**) show that the surfaces of both rubrene and ^{13}C-rubrene crystals are clean and molecularly flat, with an average step height of 1.3 nm. The step height is close to the interlayer distance along the *c*-axis, which is 1.34 nm calculated from Bragg's Law for the (002) reflection. In addition, the crystals were analyzed by single-crystal X-ray crystallography (see Table A1.1 in Appendix) and revealed a solid-state packing essentially identical to that of native rubrene.[201] The structural characterization was crucial to this study to ensure that no large difference in measured transistor properties could be attributed to differences in crystal structure. This confirms that those crystals with good crystallinity and clean, flat surfaces are qualified for the fabrication of single crystal FETs. Importantly, by Raman spectroscopy we observed a clear isotope effect on low-wavenumber intermolecular modes (**Figure 5.1c**). Peaks from the ^{13}C-rubrene sample in the range of 40 to 200 cm^{-1} appeared at systematically lower wavenumbers, as predicted. These low frequency modes are expected to be critical for transport as they transiently modulate the intermolecular transfer integrals. For example, the Raman peak at 48.0 cm^{-1} shifts to 46.3 cm^{-1} after ^{13}C-substitution, a 3.5% decrease, which is expected to cause a comparable decrease in mobility according to Equation (5.1). In addition, the high-wavenumber modes were also investigated by both IR and Raman (Figure A1.1 in Appendix), demonstrating that ^{13}C-substitution leads to a red-shift for all the vibrational modes in rubrene.

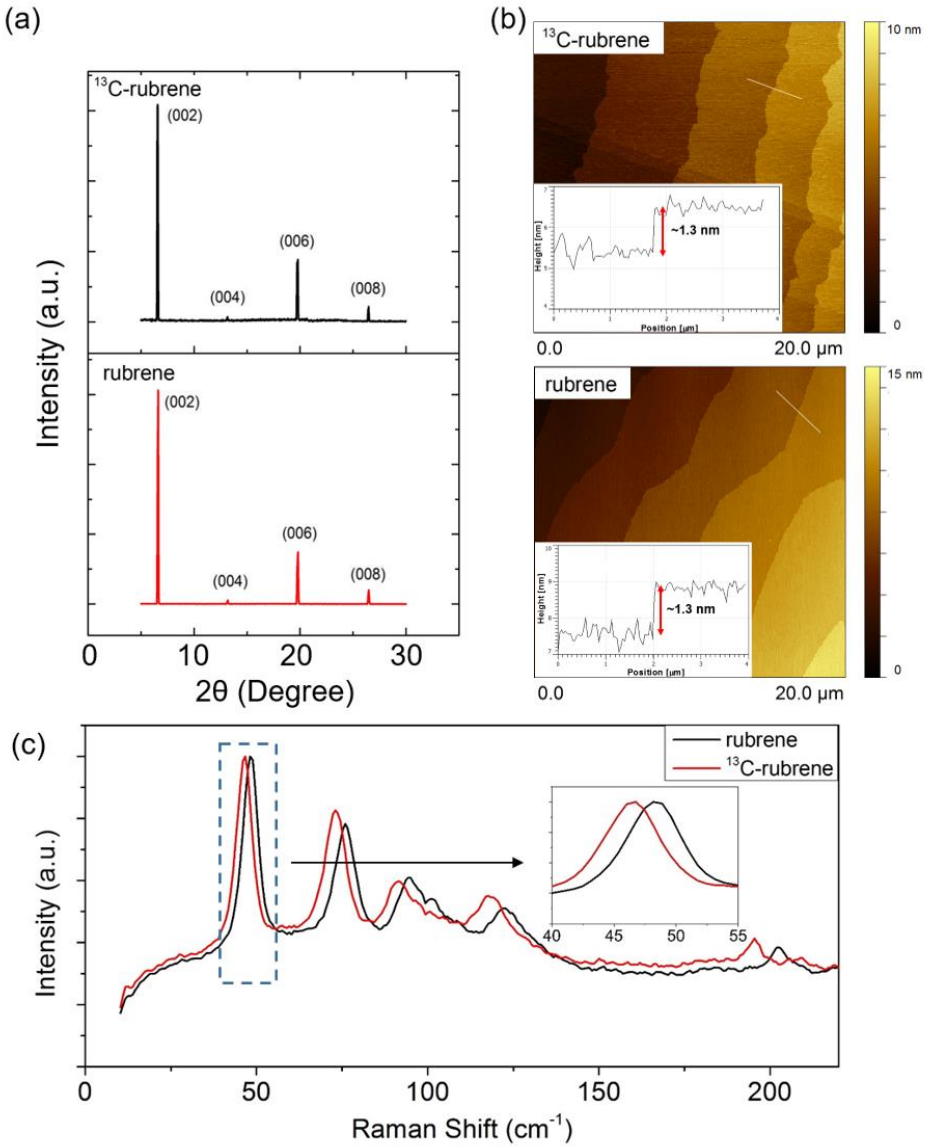

Figure 5.1 Structural characterization of rubrene and ^{13}C-rubrene. (a) Wide-angle X-ray diffraction patterns. (b) Tapping-mode atomic force microscopy height images (inset: height profiles of the white lines in the image). (c) Low-wavenumber Raman spectrum (inset: zoomed-in image of the first peak). The crystal structures are identical, but all the vibrational modes are shifted to lower frequencies.

Air-gap transistors based on ^{13}C-rubrene single crystals were fabricated on PDMS substrates according to earlier publications.[88] The device structure is shown in **Figure 5.2a**. The ^{13}C-rubrene single crystal transistors exhibit p-type operation like native rubrene transistors, in which the semiconducting channel opens at negative gate bias ($V_G < 0$ V). The lack of hysteresis in both transfer curves (**Figure 5.2b**) and output curves (**Figure 5.2c**)

is evidence for a low density of trap states at the rubrene/air interface, as can be expected for the air-gap structure.[93] As shown in **Figure 5.2b**, the device turns on near $V_G = 0$ V and has an on/off ratio of ~10^4. For V_D = -1 V, -2 V and -5 V, the device operates in the linear regime at large V_G, and the perfectly linear transfer curves are indicative of a high quality single crystal FET. The field-effect mobility can be calculated by the standard FET equation ($V_D << V_G - V_{TH}$):

$$I_D = \frac{W}{L} C_i \mu V_D (V_G - V_{TH}) \tag{5.2}$$

where W and L are the width and length of the semiconducting channel, C_i is the specific gate capacitance (for the 5 μm gap, C_i ~ 0.18 nF/cm^2), and V_{TH} is the threshold voltage, which is determined by the intercept from linear extrapolation of I_D to the V_G axis. Regardless of the drain voltage, the device shown in **Figure 5.2b** has a threshold voltage of ~ –5.5 V, and a hole mobility of 15.3 cm^{2}V^{-1}s^{-1}, which is a typical value for high-performance single crystal air-gap FETs. From the output characteristics in **Figure 5.2c**, a linear I_D-V_D relationship at low bias confirms the Ohmic nature of the metal/semiconductor contacts, implying that the hole injection barrier at the contacts is very low, which may originate from the alignment of the HOMO level of ^{13}C-rubrene with the work function of Au.[202]

Variable-temperature electrical measurements were employed to elucidate the charge transport behavior of ^{13}C-rubrene single crystals, and were carried out on devices with a 4-probe configuration to correct for temperature-dependent contact resistance.[56] Two voltage-sensing probes were inserted into the channel to measure the real potential drop

within the channel. In this configuration, the contact-corrected 4-probe field-effect mobility (μ_{4p}) is calculated by:

$$\mu_{4p} = \frac{\Delta L}{WC_i} \frac{\partial \frac{I_D}{\Delta V}}{\partial V_G} \tag{5.3}$$

where ΔL and ΔV are respectively the distance and the potential difference between the two reference probes. The μ_{4p} *vs.* T relationships for three different devices are presented in **Figure 5.2d**. It is clear that the mobility increases with decreasing temperature ($d\mu/dT < 0$), which implies that band-like transport is operative in ^{13}C-rubrene single crystals. During the cooling process, some of the crystals broke apart, which is common for this device architecture due to the difference in thermal contraction for rubrene versus the PDMS stamp. For those crystals that did not crack, when they were heated back to 300 K, the mobility returned to the original value, indicating that the devices did not suffer any thermal degradation during the thermal cycle. The band-like transport phenomenon is reproducible in ^{13}C-rubrene single crystals and has been observed in almost all the devices with room-temperature $\mu_{4p} > 10$ cm^{2}V^{-1}s^{-1}. Interestingly, all three devices shown in **Figure 5.2d** exhibit band-like transport behavior until $T \leq 100$ K. In other words, the critical transition temperature (T^*) from the intrinsic band-like regime to the shallow-trap-dominated regime can be as low as 100 K. According to Morpurgo and coworkers, a lower T^* means that a smaller degree of static disorder is present in the air-gap transistor.[28] For organic single crystal FETs, such a low T^* has only been reported in high quality rubrene and deuterated-rubrene (^{2}H-rubrene) single crystals.[36] Based on these results, it is reasonable to say that ^{13}C-rubrene single crystals have essentially the same T-dependent transport as native rubrene.

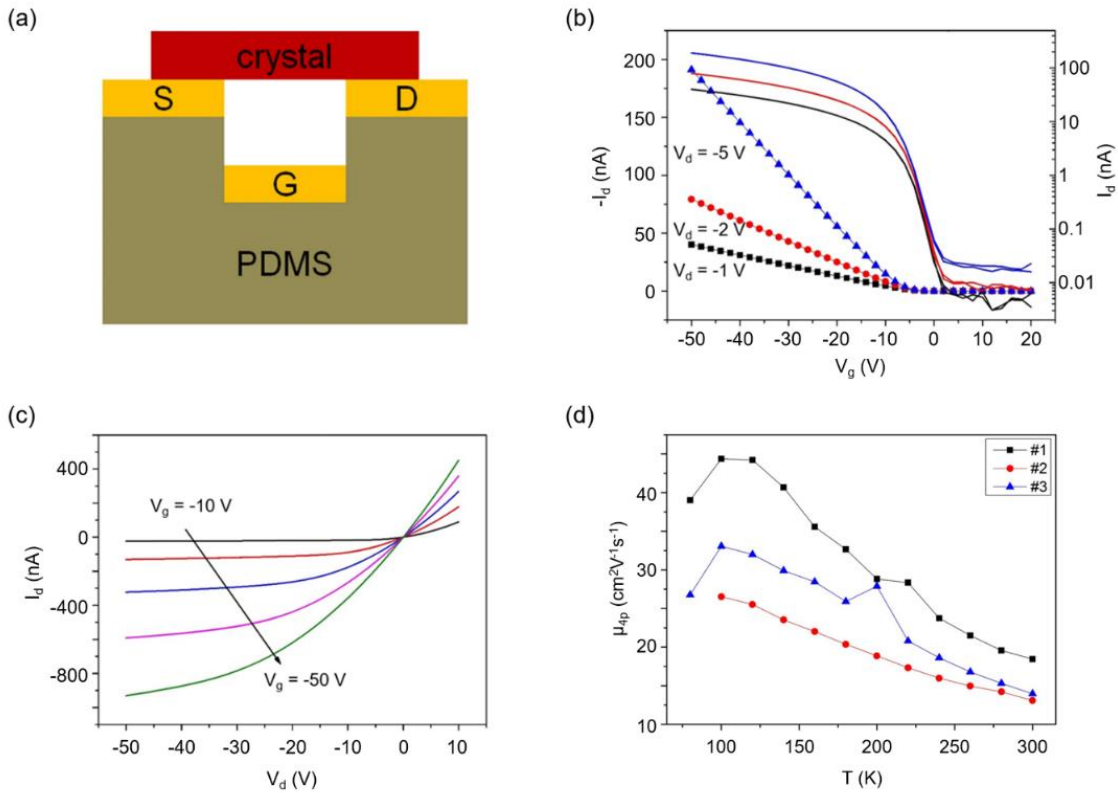

Figure 5.2 (a) Cross section of the device structure. (b) Room temperature transfer characteristics of a device in linear scale (left axis) and log scale (right axis). (c) Room temperature output curves of the same device with gate voltages from –10 V to –50 V. (Device dimensions: L = 300 μm, W = 100 μm.) (d) Temperature dependence of the mobility for three different ^{13}C-rubrene devices. Band-like transport persists to 100 K in these samples.

To further elucidate the intrinsic transport behavior, we carried out Hall measurements on a ^{13}C-rubrene single crystal FET which displayed band-like transport down to 100 K. **Figure 5.3a** shows the Hall resistance (defined as $R_{xy} = V_{xy}/I_d$) as a function of magnetic flux density (B) between 5 T and –5 T at different temperatures with a scan rate of 0.01 T/s. The gate voltage and source current were fixed at –40 V and 10 nA, respectively. A clear Hall signal with a positive slope can be observed, which is consistent with the p-type conduction in ^{13}C-rubrene FETs. The noise level increases very rapidly upon cooling, so any Hall measurement at T < 180 K is prevented, which has been reported earlier in rubrene air-gap transistors.[9] The slope of R_{xy} - B, which is the Hall coefficient $R_H = 1/ep_{Hall}$,

increases with decreasing temperature, indicating smaller charge density at lower temperature. We can extract the Hall mobility (μ_{Hall}) from the equations below:

$$\mu_{Hall} = \frac{\sigma}{ep_{Hall}} = \frac{R_{xy}}{BR_{xx}}\frac{\Delta L}{W} \tag{5.4}$$

where σ is the channel conductivity and R_{xx} is defined as $R_{xx} = \Delta V/I_d$. As shown in **Figure 5.3b**, both μ_{Hall} and μ_{FET} increase upon cooling and their trends are similar, implying that our device is still in the band-like regime even at 180 K. The Hall measurement confirms that the intrinsic, band-like hole transport has been achieved in ^{13}C-rubrene single crystals.

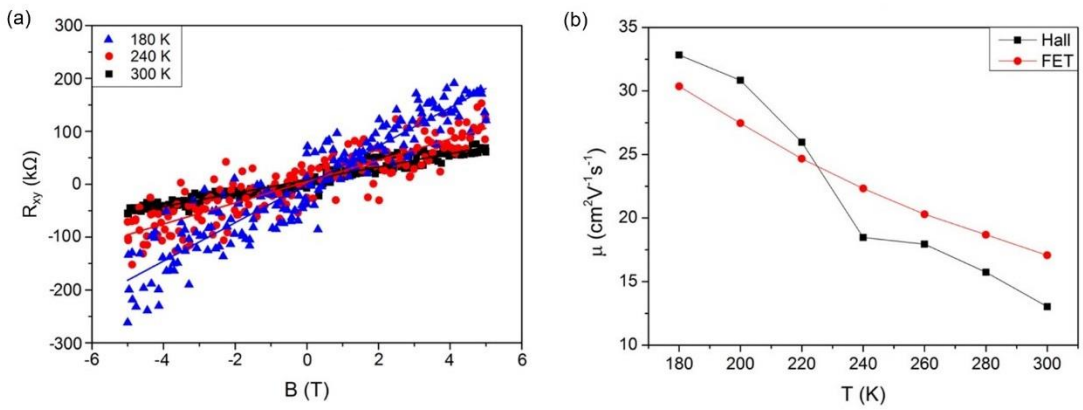

Figure 5.3 (a) Temperature dependence of Hall resistance for a ^{13}C-rubrene air-gap transistor. Measurements were taken at I_D = 10 nA and V_G = –40 V. This device has dimensions of ΔL = 350 μm and W = 220 μm. (b) Temperature dependence of the FET and Hall mobility for this device. Band-like transport persists over the whole temperature range (T > 180 K) in this device.

5.3 Isotope effect and theoretical explanation

To compare FET mobilities for ^{13}C-rubrene and native rubrene, we fabricated 74 ^{13}C-rubrene single crystal FETs in order to get a reasonable distribution of field-effect mobility. In addition, another 74 native rubrene single crystal FETs were fabricated and tested under the same conditions. We find that the mean values for mobility are 12.6 ± 2.2 $cm^2V^{-1}s^{-1}$ and 14.6 ± 2.4 $cm^2V^{-1}s^{-1}$, respectively, for ^{13}C-rubrene and native rubrene, where the

uncertainty interval represents 1 standard deviation. However, as many measurements were made, the t-test can be employed to find the confidence intervals on the mean values of the mobility, which are the confidence levels of finding the true values in such intervals. Based on the full statistics of mobility in **Figure 5.4a**, our calculations reveal that even the 99% confidence intervals have no overlap (see Appendix for detailed calculation). The 99% confidence interval on the mean value of mobility for ^{13}C-rubrene single crystal FETs is found to be 12.6 ± 0.7 $cm^2V^{-1}s^{-1}$, while that for native rubrene is 14.6 ± 0.7 $cm^2V^{-1}s^{-1}$. That is, statistically speaking the mean values of mobility for native rubrene and ^{13}C-rubrene are truly different and based on the mean values, the isotope effect is –13%. We conclude that we have observed a negative isotope effect on charge transport in rubrene single crystals upon complete ^{13}C-substitution.

It is unlikely that the negative isotope effect is due to extrinsic factors such as impurities or structural defects because the ^{13}C-rubrene crystals exhibit beautiful transport properties as shown above and are grown under the same conditions after extensive efforts have been made to clean the ^{13}C-rubrene starting material. The purity and structural perfection was confirmed by photothermal deflection spectroscopy (PDS), which is a highly sensitive absorption technique that measures the density of optically active sub-bandgap states in organic semiconductors.[203,204] In **Figure 5.4b**, it is obvious that both ^{13}C-rubrene and native rubrene have clean bandgaps. Spectra of 2 different ^{13}C-rubrene crystals are shown here in order to demonstrate that the measurements are reproducible. Moreover, the Urbach energy (E_u), which is determined from an exponential fitting of the absorption band edge across 4 decades of signal, can be used to characterize the atomic disorder in each crystal. **Figure 5.4b** reveals that ^{13}C-rubrene and native rubrene have a similar Urbach

energy (~40 meV), which means their degrees of disorder (including both static and dynamic disorder) are comparable. It is thus reasonable to conclude that the origin of the negative isotope effect is the red-shift of vibrational frequencies after ^{13}C-substitution as predicted by DDM.

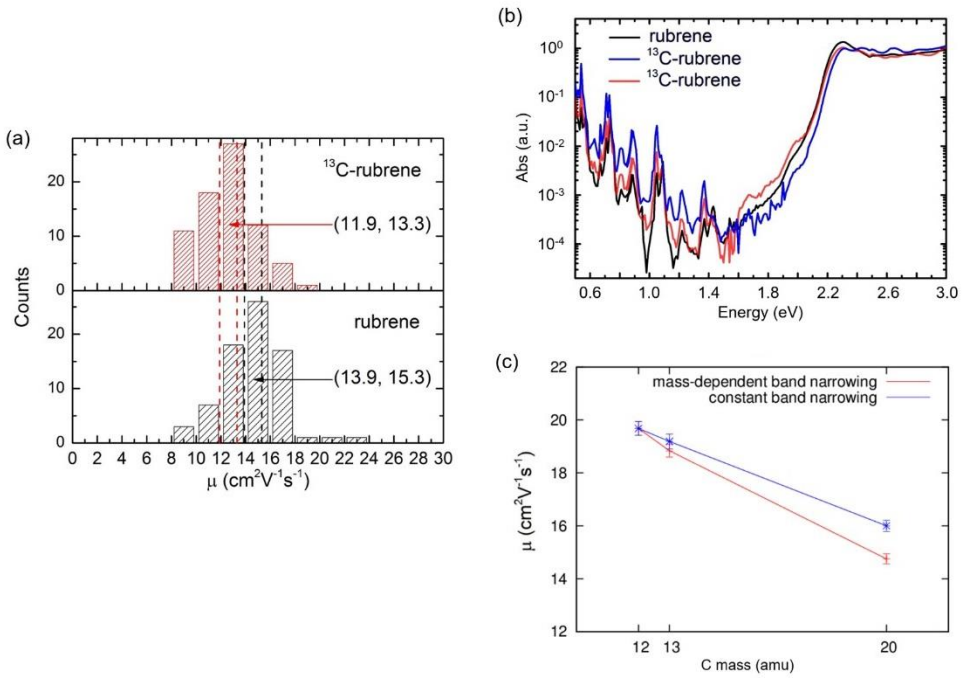

Figure 5.4 (a) Histograms of the room temperature mobility for rubrene and ^{13}C-rubrene. The regions between the dashed lines represent the 99% confidence intervals on the mean values and they have no overlap. (b) Photothermal deflection spectroscopy of a native rubrene and 2 ^{13}C-rubrene crystals. (c) Carbon mass dependence of the calculated mobility of rubrene under two different assumptions: mass-dependent band narrowing (red) and constant band narrowing (blue)

To gain further insight, we carried out simulations based on a numerical model of dynamic disorder introduced by Troisi *et al*.[40] In earlier work it was predicted from this numerical model that increasing the molecular mass will cause a decrease in mobility.[40] However, this model did not include the effect of high-frequency modes. It has been reported that the effect of charge coupling to high frequency vibrations is to reduce the

transfer integrals between neighboring molecules, which is known as band narrowing.[17,205] This effect effectively decreases l_{loc} and is distinct from the role of low frequency intermolecular modes which impact μ through ω. Band narrowing is mass-dependent and from Holstein small polaron theory we find that the bandwidth (transfer integral) of ^{13}C-rubrene is 3.5% narrower (this is an upper limit) due to the increased mass. Adding mass-dependent band narrowing to the dynamic disorder scenario, we computed the mobility at 300 K using rubrene parameters taken from a previous publication.[41] The computed mobility decreases from 19.7 to 18.8 $cm^2V^{-1}s^{-1}$ in going from ^{12}C- to ^{13}C-rubrene, i.e. by 4.5%. If the band narrowing effect is neglected, the mobility reduction is 2.5%. Thus, the simulations confirm a significant negative isotope effect, although the calculated change is smaller than the experimental value. We also calculated the mobility of a hypothetical rubrene where the atomic mass of C is 20 amu to see the isotope effect more clearly (**Figure 5.4c**). Indeed, heavier C atoms produce a more pronounced negative isotope effect. The qualitative agreement between experiment and theory broadly supports the dynamic disorder picture of transport in rubrene, but the quantitative discrepancy between the measured and simulated isotope effect suggests opportunities for further investigations. One possible explanation for the difference could be the existence of a sizable feedback between the reduced vibrational frequencies and the presence of unavoidable sources of extrinsic disorder, signaled here by the observed downturn of the mobility at temperatures below ~100 K. Reduced vibrational frequencies do lead to a reduced hole mobility, but it can also be expected that the resulting slower carriers become more prone to scattering and trapping by impurities and defects, an effect that should further reduce the overall mobility.

This hypothesis was confirmed by preliminary calculations in the presence of site disorder, showing that the effect of isotope substitution is enhanced by a factor of 2-3.

5.4 Conclusions

In summary, we have successfully synthesized ^{13}C-substituted rubrene and systematically investigated the structural and electrical properties of vapor-grown ^{13}C-rubrene single crystals. ^{13}C-rubrene single crystals maintain the intrinsic transport behavior of native rubrene, including hysteresis-free output and transfer characteristics, an average hole mobility over 10 $cm^2V^{-1}s^{-1}$ at room temperature, and the clear signature of band-like transport persisting to very low temperature ($T \leq 100$ K), with a maximum mobility of ~45 $cm^2V^{-1}s^{-1}$ at ~100 K. The excellent performance of ^{13}C-rubrene single crystal FETs is further confirmed by the observation of the Hall effect in the conducting channel of a ^{13}C-rubrene air-gap transistor, which provides characteristic evidence of the diffusive delocalization of charge carriers over a few molecules. Importantly, we have observed a significant negative isotope effect on charge transport in rubrene single crystals after ^{13}C-substitution, which originates from the decreased vibrational frequencies of ^{13}C-rubrene and supports the physical picture of transport under the influence of dynamic disorder. In a general sense, we believe that ^{13}C isotopic substitution opens new opportunities to understand transport phenomena in organic single crystals.

5.5 Experimental methods

Single crystals of ^{13}C-rubrene were grown by the well-developed horizontal physical vapor transport (PVT) method using ultrapure Ar as carrier gas.[78,79] The sublimation temperature was kept at 280-290 °C and growth usually took several days. Crystals collected after one round of PVT were used as source material for a second round of PVT

to minimize impurities in the crystals used for transistor measurements. The surface quality of organic single crystals is very important for charge transport, so only those crystals with very smooth surfaces were selected for device fabrication.

Single-crystal X-ray crystallography was collected on a BRUKER APEX II diffractometer with Cu Kα radiation (λ = 0.154 nm) at 123 K. A Panalytical X'Pert Pro diffractometer was used for the wide-angle XRD experiment, in which monochromatic Cu Kα radiation was applied at 45 kV and 40 mA. The AFM images of the single crystals were taken by a Bruker NanoScope V Multimode scanning probe microscope operating in tapping mode and analyzed using the software Gwyddion. The Raman spectra of were collected in a backscattering geometry using a confocal Raman spectrometer (Witec Alpha300R) with linearly polarized radiation at 633 nm.

PDMS-based air-gap transistors were fabricated according to previous reports.[88] First, the desired patterns were defined on a silicon wafer by photolithography. The wafer was then put in a clean petri-dish and PDMS pre-polymer (Sylgard 184, Dow Corning) was mixed with curing agent and poured into the petri-dish. After it was degassed and baked, the PDMS stamp was peeled off. The depth of the air-gap was measured to be roughly 5 μm by a KLA-Tencor P-16 surface profiler. Finally, Cr/Au contacts (3/20 nm) were formed by electron-beam evaporation using a CHA electron beam deposition system. The air-gap transistors were fabricated by simply laminating the crystals over the source and drain electrodes with their long-axis aligned across the channel. The van der Waals interaction between the crystal and the substrate led to good contacts between organic crystal and Au electrodes. The 5 μm air-gap served as the gate dielectric. All the devices were fabricated

under ambient conditions and transferred into a nitrogen-filled glovebox for further electrical measurements.

Output and transfer characteristics of the transistors were taken in a Desert Cryogenics (Lakeshore Inc.) probe station in a nitrogen-filled glovebox equipped with Keithley 236 and 2612 source-measure units (SMUs) and homemade Labview programs. Two Keithley 6517A electrometers were connected to the voltage-sensing probes for 4-probe measurement. A Lakeshore 331 temperature controller was employed in low-temperature current-voltage (*I*-*V*) measurements. All measurements were performed in vacuum and in the dark.

Temperature- and field-dependent measurements of Hall effect were conducted in a Physical Property Measurement System (PPMS, Quantum Design) with a 9 T superconducting magnet. A Keithley 2400 SMU was used to apply gate voltage, and a Keithley 220 SMU and a Keithley 2002 electrometer were respectively used to source current and measure voltage. To prepare the device for Hall measurement, the crystal was laminated on the PDMS substrate with pre-patterned Hall-bar geometry. The sample was wired on the PPMS puck by Au wires (25 μm diameter) and Ag paint.

PDS measurements were performed on a home-built set-up described by Vandewal *et al.*[206] Measurements were taken using a mechanically chopped (3.333Hz) monochromatic light source using both a 150W Xenon and 100W halogen pump lamp with 5nm spectral resolution focused onto the sample. Degassed and filtered perflourohexane (C_6F_{14}, 3M Flourinert FC-72) was used as the deflection medium. Single crystal samples were transferred onto PDMS on quartz substrates that were stored and transferred in a nitrogen

environment with < 1ppm of oxygen. The crystals were aligned with maximal overlap between the pump beam and single crystal.

Chapter 6 Scanning Kelvin Probe Microscopy Reveals Planar Defects Are Sources of Electronic Disorder in Organic Semiconductor Crystals

Electronic disorder in organic semiconductor single crystals, manifested as parallel surface potential domains with potential variations ranging from tens to hundreds of mV, is observed by scanning Kelvin probe microscopy. Chemical etching and X-ray diffraction indicate that the potential domains are correlated with planar defects such as stacking faults. The results have important implications for understanding structure–transport relationships in organic semiconductor single crystals. This work has been published as *Y. Wu, X. Ren, K. A. McGarry, M. J. Bruzek, C. J. Douglas, and C. D. Frisbie, "Scanning Kelvin Probe Microscopy Reveals Planar Defects Are Sources of Electronic Disorder in Organic Semiconductor Crystals", Advanced Electronic Materials, 2017, 3, 1700117*.

6.1 Introduction

Single crystals of organic semiconductors play a central role in organic electronics research because their low levels of static disorder (vis-à-vis thin films) provide opportunities for examining fundamental electrical transport behavior.[5–7,190] Field effect transistor (FET) measurements based on single crystals of the benchmark semiconductor rubrene, for example, have revealed remarkable transport properties and redefined our understanding of intrinsic transport limits.[8] Key observations on rubrene single crystal FETs include highly reproducible room temperature hole mobilities above 10 $cm^2V^{-1}s^{-1}$, band-like temperature dependence of the mobility (i.e., mobility increasing with cooling down to 100 K), robust Hall effect behavior, and clear mobility anisotropy correlated with

the crystal structure.[9,59,90,91] Collectively, these results support the physical picture of highly mobile and partially delocalized carriers in the crystalline limit where defect densities are low. A handful of other organic semiconductor materials have shown similar behavior suggesting that the excellent properties of rubrene should be general to many single crystal organic semiconductors.[29,32–34,60,207,208]

Yet in reality, the situation is not so simple. Many organic semiconductor materials that appear to be promising in terms of their solid state packing and electronic structure (π-π overlap) do not perform well in commonly employed field effect transport measurements, even in single crystal form.[202,209] This includes materials for which the calculated transfer integrals exceed those for rubrene.[209] In those cases in which the intrinsic packing and electronic structure appear to be excellent for transport, it seems obvious that the difficulty must be extrinsic disorder, i.e., defects that lead to charge traps and barriers. However, it is not always straightforward to detect such disorder. X-ray methods do provide a powerful approach in some cases, though most reports of single crystal FET measurements are not accompanied by detailed X-ray analysis to reveal inhomogeneous strains or dislocation densities, for example. X-ray approaches (e.g., tomography) can also be laborious or require specialized equipment, which can limit their routine application to organic crystals that have not performed well in transport experiments.[210] Thus, the highly desirable link between performance and structure is often broken and, consequently, the inability to consistently and rationally synthesize crystals with superior transport properties remains a long-standing and frustrating challenge for organic electronics.

In this paper we report the observation that surface potential images obtained by scanning Kelvin probe microscopy (SKPM) of many organic semiconductor crystals have

striking contrast that reflects a high degree of electronic disorder. The amplitudes of the surface potential fluctuations can reach 100 mV or more (i.e., > kT), so that it is clear the disorder, which creates "hills" and "valleys" for charge, will affect charge transport, particularly field effect transport that occurs on the surfaces of crystals. The surface potential contrast is directly correlated with structural disorder revealed through a combination of grazing incidence X-ray diffraction and chemical etching. In some cases, it is obvious that the "single crystal" sample is indeed not a single crystal domain, but is instead composed of large crystalline subdomains, much like highly twinned metal crystals. In other cases it appears that stacking faults (i.e., planar defects) are the source of the surface potential variations. While prior work on thin films has shown the ability of SKPM to visualize defects such as grain boundaries,[211–213] the discovery that structural and associated electronic disorder in organic single crystals can be visualized and quantified by a scanning probe technique is important for organic electronics because it provides a rationale for why many organic crystals underperform in transport experiments. To our knowledge, detection of extensive defects in organic single crystals by SKPM has not been reported before.

6.2 Observation of electronic disorder

As model systems, we focus on a series of rubrene derivatives that have packing arrangements similar to their parent molecule, rubrene. One of the rubrene derivatives, bis(trifluoromethyl)-dimethyl-rubrene (FM-rubrene), preserves the same space group as rubrene when grown by the physical vapor transport method.[202] The molecular structure and crystal packing of FM-rubrene are shown in **Figures 6.1a and 6.1b**. Single crystal X-ray crystallography shows that like rubrene, sublimation-grown FM-rubrene crystals adopt

an orthorhombic structure (*Cmca* space group) and slipped π-stack packing motif with the π-stacking direction along the *b* axis.[202] Interestingly, polarized light microscopy of as-grown crystals (**Figure 6.1c**) indicate a single crystal domain with the largest facet being the (100) plane and the longest direction aligned with the crystallographic *b* axis. Quantum chemical calculations based on the crystal structure indicate that electronic transfer integrals are somewhat larger for FM-rubrene than native rubrene suggesting that the electrical transport properties should be favorable.[209] Indeed, single crystals of FM-rubrene display reasonable transport properties in FETs (contact corrected hole mobility ~ 1 $cm^2V^{-1}s^{-1}$),[202] though not as good as native rubrene (contact corrected hole mobility > 10 $cm^2V^{-1}s^{-1}$). The poor performance compared to native rubrene was puzzling to us and suggested that there must be structural disorder in FM-rubrene.

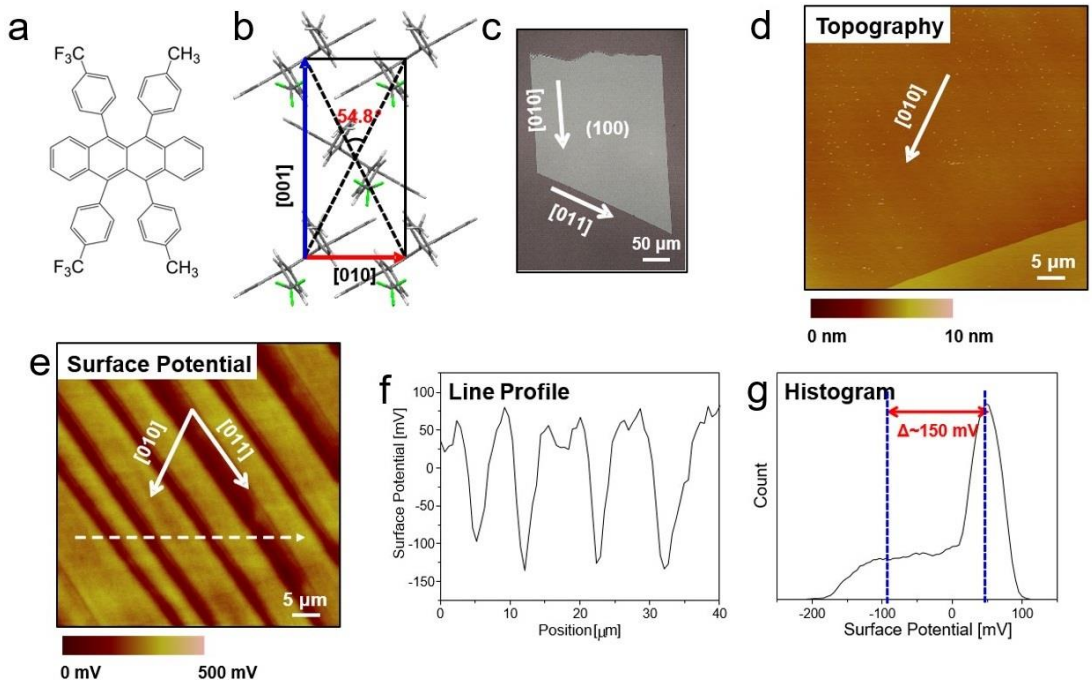

Figure 6.1 (a) Molecular structure of FM-rubrene. (b) Crystal structure in the *b*-*c* plane. (c) Cross-polarized optical micrograph of as-grown FM-rubrene crystal. (d) Topography of FM-rubrene single crystal shows typical terrace structure and each terrace has a height

corresponding to one molecular layer. (e) Corresponding surface potential image obtained simultaneously with topography shows parallel stripes across the surface. (f) Surface potential line profile obtained from the dashed line in (e). (g) Surface potential histogram of the entire surface potential image in (e).

Figures 6.1d and 6.1e show the topography and surface potential images of a FM-rubrene (100) surface obtained by SKPM. The topography image reveals a clean surface with a 17 Å molecular step, coinciding with one-half of the *a* axis unit cell parameter. This is similar to the topography of the rubrene (100) surface, only with a slightly larger step height, as expected, due to the orientation of the $–CH_3$ and $–CF_3$ groups along this axis.

Significantly, the corresponding surface potential map shows striking contrast. There are parallel dark (more negative surface potential) stripes on a bright (more positive surface potential) background. Such surface potential corrugation is quantitatively depicted by the potential line profile in **Figure 6.1f**. Histogram analysis of the entire surface potential image (**Figure 6.1g**) reveals that the average surface potential difference between the dark stripes and the bright background is approximately 150 mV, very significant compared to thermal voltage *kT/e* (25 mV) at room temperature. Examination of approximately 100 FM-rubrene crystals reveals that the majority display surface potential stripes with amplitudes from ~50 mV to ~700 mV as shown in Appendix, Figure A2.1. It is reasonable to suppose that the stripes in **Figure 6.1** reflect structural defects;[212,214,215] indeed, we show below that this is the case. The important point at this juncture is that SKPM reveals defects that are not detected by topographic scans (**Figure 6.1d**) or by polarized light microscopy (**Figure 6.1c**). In addition, standard out-of-plane X-ray diffraction (XRD) revealed no obvious anomalies for any of the crystals (see Figure A2.2 in Appendix). As optical microscopy and out-of-plane XRD are commonly employed to assess the quality of crystals,

it is clear that the defects in **Figure 6.1**, which are readily observable by SKPM, could be missed.

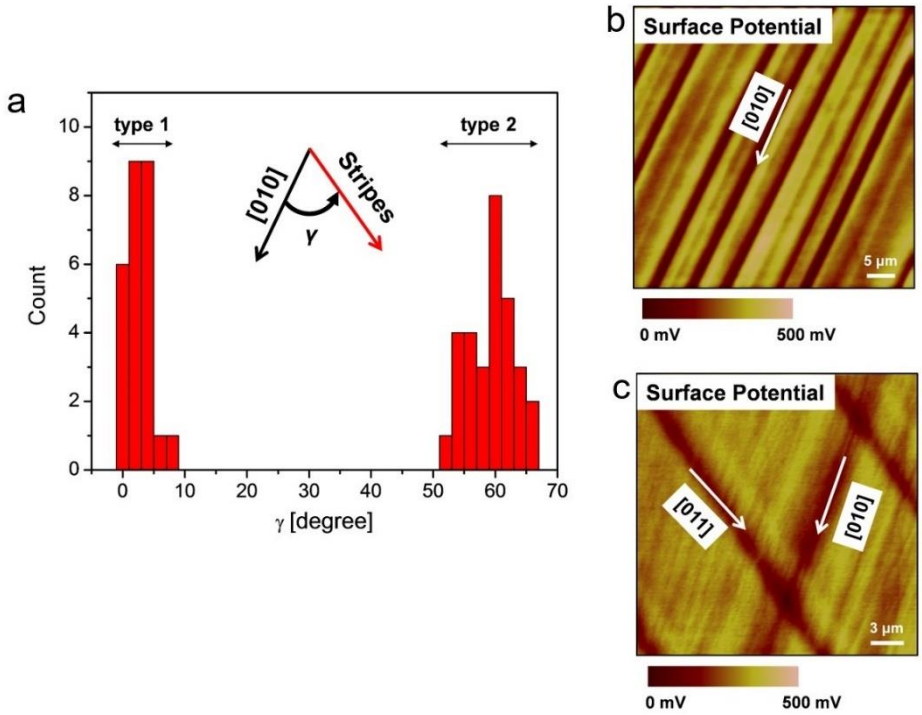

Figure 6.2 (a) Distribution of the orientations of the surface potential stripes in about 50 FM-rubrene samples. The orientation is quantified by the angle (γ) between the stripes and the [010] axis. There are two distinct populations of the samples, one with stripes parallel to the [010] axis (type 1 defect) and the other having a ~60° angle between the stripes and the [010] axis, *i.e.*, parallel to the [011] axis (type 2 defect). (b) A typical surface potential map showing potential stripes parallel to the [010] axis. (c) A rare surface potential map showing crossing potential stripes, one parallel to the [010] axis and the other roughly parallel to the [011] axis.

The crystallographic orientation of the potential stripes was quantified by measuring the angle (γ) between the stripes and the [010] direction, which is aligned along the long axis of the crystal. As indicated in **Figure 6.1e**, the surface potential stripes correspond to the [011] direction. However, upon sampling over 50 crystals, two distinct stripe orientation populations were observed as shown in **Figure 6.2a**, one with γ close to 0° (i.e., stripes along [010], termed a type 1 defect) and the other close to 60° (i.e., stripes along [011], as in **Figure 6.1e**, termed a type 2 defect). **Figure 6.2b** is an example surface potential map

with stripes parallel to [010] and it looks similar to the surface potential image in **Figure 6.1e** in which the stripes are aligned along [011]. **Figure 6.2c** displays a rare image in which surface potential stripes of both orientations are present. The two types of stripes cross through each other. Although we did not frequently observe the situation shown in **Figure 6.2c**, it clearly supports the co-existence of two different potential stripe orientations, and two types of defects, in FM-rubrene crystals.

6.3 Structural origin of electronic disorder

Nearly all FM-rubrene crystals exhibited surface potential stripes. This is very different from our previous examinations of rubrene single crystals by SKPM which show homogeneous surface potential images.[188] To characterize the nature of the defects leading to striping, we undertook *in-plane* (grazing incidence) XRD measurements of the (100) major facet, as out-of-plane XRD (i.e., with the scattering vector normal to (100)) was not informative. Specifically, we performed ϕ scans (ϕ is the angle of the incident X-ray beam relative to a reference crystallographic direction in the (100) plane of the crystal). The geometry of the experimental setup is shown in **Figure 6.3a**. The incident X-ray and detector positions (2θ) are fixed at grazing incidence and reflection and the sample rotates (i.e., ϕ is varied from 0° to 360°). The in-plane 2θ value was determined by the diffraction condition for a particular plane in FM-rubrene; we chose the (022) plane, corresponding to $2\theta = 27.68°$. Since the multiplicity of (022) plane of FM-rubrene is 4, we expected to observe 4 peaks separated by 55° or 125° according to the angle between planes (022) and $(0\bar{2}2)$ of the crystal. However, as shown in **Figure 6.3b**, the ϕ scan shows two sets of peaks instead of one and the angle between the two sets of peaks is roughly 90°. This indicates that this sample is *not* a single crystal; there are sub-domains oriented at 90° to each other.

The situation is depicted in **Figure 6.3c**. Importantly, we observe for such samples that potential stripes align with the [010] direction. Thus, the **Figure 6.3b** data represent detection of type 1 defects, which correspond to parallel domain boundaries between sub-crystals oriented at 90° with respect to each other. Again, neither optical microscopy nor out-of-plane XRD revealed these defects.

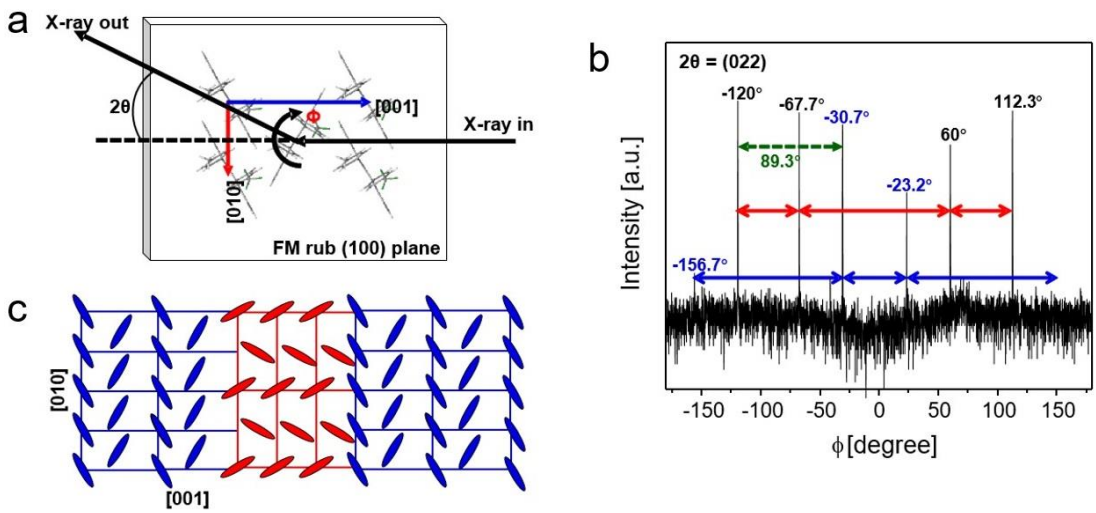

Figure 6.3 Grazing incidence XRD revealing type 1 defects in FM-rubrene. (a) Schematic of the grazing incidence (in-plane) ϕ scan of an FM-rubrene single crystal. The (022) plane with multiplicity of 4 was chosen because unlike planes such as (004), its 2θ value is not too close to the 2θ values of other planes to cause any confusion (see Table A2.1). (b) ϕ scan of FM-rubrene shows two sets of peaks for the (022) diffraction plane. The angle between the two sets of peaks is approximately 90°. (c) Schematic of the proposed type 1 defect in FM-rubrene in which surface potential stripes are aligned along [010].

To further explore the defect structures, we chemically etched the FM-rubrene crystals with ethanol. Chemical etching of defects in organic single crystals was reported for anthracene, naphthalene, and tetracene crystals as early as the 1960s.[216–218] Surprisingly, we found that crystals with type 1 defects did not etch under the conditions we employed. However, crystals with type 2 defects showed deep etch grooves aligned along the [011] stripe direction. **Figures 6.4a and 6.4b** show the topography and corresponding surface potential images of a partially etched FM-rubrene single crystal. The AFM topography

image in **Figure 6.4a** shows parallel grooves with depths on the order of 100 nm according to the line profile analysis. In the corresponding surface potential image (**Figure 6.4b**), the potential corrugation is not as obvious in the deeply etched regions as in regions not yet significantly etched. Importantly, there is a one-to-one correlation between the etching grooves and the surface potential stripes.

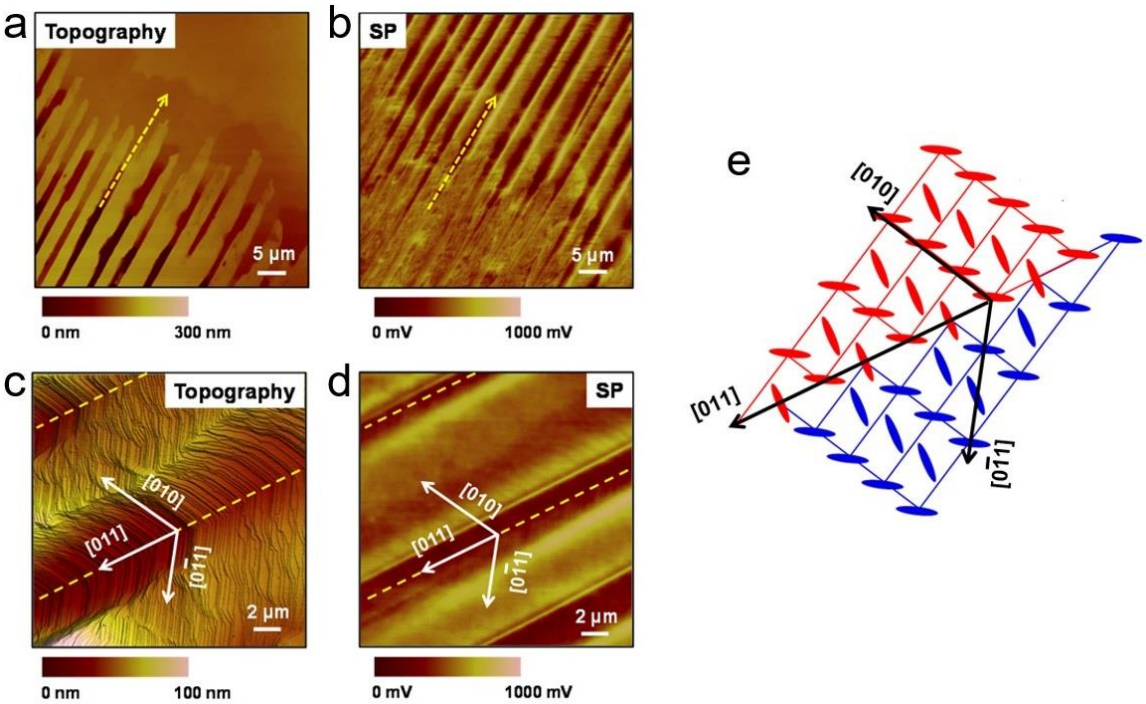

Figure 6.4 Chemical etching of type 2 defects in FM-rubrene. (a) Topography of a partially etched FM-rubrene single crystal shows parallel etch grooves in the deeply etched regions. (b) The simultaneously acquired surface potential image of the crystal in (a). The surface potential corrugation in the deeply etched regions is hard to distinguish while the potential stripes still remain in the regions that are not yet etched. The material in the dark stripe regions is etched preferentially. (c) Higher magnification topography scan of the grooves created by chemical etching. The stable crystallographic directions revealed by etching are the [010] and [0$\bar{1}$1] directions. (d) Simultaneously acquired surface potential map of the crystal in (c). The centers of the dark potential stripes correspond with the centers of the grooves. (e) Schematic of proposed stacking fault in FM-rubrene that results in potential stripes parallel to [011].

To take a closer look at how the grooves form, the etching time was controlled to render an FM-rubrene surface that was only slightly etched. The topography and the

corresponding surface potential images at higher magnification are shown in **Figures 6.4c and 6.4d**, respectively. The grooves are highly faceted, **Figure 6.4c**. It appears that the stable crystallographic directions revealed by etching correspond to the [010] and [0$\bar{1}$1] directions, as labeled in the figure. The grooves along [011] gradually deepen as the etching fronts of the top molecular layers advance over time followed with the etching of the underlying layers. The corresponding surface potential image in **Figure 6.4d** reveals that the center of the dark potential stripes coincides with the center of the grooves.

It is known that defect types can be determined by the shapes of the etch pits. Etch grooves are typically regarded as the result of two-dimensional planar defects, which include, for instance, grain boundaries, twin boundaries, and stacking faults.[219–221] We have not yet identified the precise nature of the type 2 planar defect in FM-rubrene; this will require sophisticated electron microscopy of these soft crystals. However, considering the specific orientations of the stripes and the groove facets in **Figures 6.4c and 6.4d**, we hypothesize that the type 2 defect is a stacking fault. **Figure 6.4e** depicts a proposed stacking fault created by partial slip of the crystal along the [011] direction by one half of the magnitude of [011]. This proposed defect is consistent with our observation that the type 2 defects were not detectable by grazing incidence XRD, conventional out-of-plane XRD, or by polarized light microscopy.

A key point is that both type 1 and 2 defects do not change the molecular packing (*d*-spacing) along the a-direction, so topographic AFM and wide-angle XRD (normal to (100)) will not be sensitive to these defects. For polarized light microscopy, the type 1 defect is likely not observed because two sub-domains oriented at 90° to each other will give uniform brightness across the crystal for all crystal orientations; the type 2 defect is not

observed because a stacking fault does not change the principal optical axes of the crystal so that the brightness is also still the same.

Of course, a crucial issue is why type 1 and type 2 planar defects exhibit surface potential contrast. We propose that both types of faults originate to relieve strain in the crystal (see below), and that residual strain between the fault planes gives rise to surface potential fluctuations. Indeed, we have demonstrated recently that very small elastic strains on the order of 0.1% in organic crystals can give rise to substantial surface potential excursions.[188] We will return to this point below.

T/K	283	333	383	433	483
Crystal Structure	Orthorhombic	Orthorhombic	Triclinic	Triclinic	Triclinic
a/Å	34.1654	34.2709	17.4039	17.3801	17.2620
b/Å	7.2502	7.2797	7.3439	7.4024	7.5012
c/Å	14.0113	14.1173	14.1270	13.9034	14.8987
α	90.0000	90.0000	89.2403	88.5863	89.6164
β	90.0000	90.0000	87.7138	86.0192	85.4755
γ	90.0000	90.0000	78.0939	78.2871	77.7923
V/Å^3	3470.670	3522.014	1765.350	1747.167	1879.563

Table 6.1 Unit cell parameters of FM-rubrene as a function of temperature. A structural transformation occurs at the temperature between 333 K and 383 K. The crystal structure changes from orthorhombic to triclinic as temperature increases.

The frequent occurrence of planar defects in FM-rubrene can be understood by temperature-dependent single crystal XRD measurements. As shown in **Table 6.1**, there is a distinct structural transformation within the temperature range of 333 K to 383 K. At room temperature, physical-vapor-grown FM-rubrene crystals adopt an orthorhombic crystal structure. As temperature increases to 333 K, the crystals undergo thermal expansion but the orthorhombic structure is preserved. However, as the temperature reaches 383 K a solid-solid phase transition occurs and the crystals adopt a triclinic

structure. When the crystals are cooled back to the room temperature, the orthorhombic crystal structure is recovered. Such a solid-solid phase transition does not occur in native rubrene as shown in Table A2.2 in Appendix; this table shows that in native rubrene only uniform changes of lattice parameters resulting from thermal expansion are observed across the entire temperature range.

FM-rubrene crystals were grown at ~500 K by the physical vapor transport method, and were cooled to room temperature for collection and analysis. Thus, the XRD results indicate that the final FM-rubrene crystals harvested from the growth apparatus went through a structural transformation from triclinic to orthorhombic crystal packing upon cooling in the furnace. Given the tremendous strain (several %, see Appendix and Figure A2.3) associated with such a solid state phase change, it is not surprising that an abundance of planar defects are generated. Furthermore, the two types of planar defects we observe in FM-rubrene, namely stacking faults and domain boundaries, likely only remove part of the elastic strain associated with the phase transition. The defects themselves have an associated free energy cost that must be balanced against the free energy gain associated with strain relief. Thus, not all of the strain associated with the phase transition will be eliminated. We thus propose that residual strain in the crystals is the cause of the surface potential domains. We have previously shown that elastic strain leads to surface potential variations in benchmark crystals of rubrene.[188] According to our previous findings, elastic strains of 0.1% can lead to surface potential variations of 100 mV. The 80-150 mV excursions we observe for FM-rubrene crystals may indeed correspond to such very small residual strains.

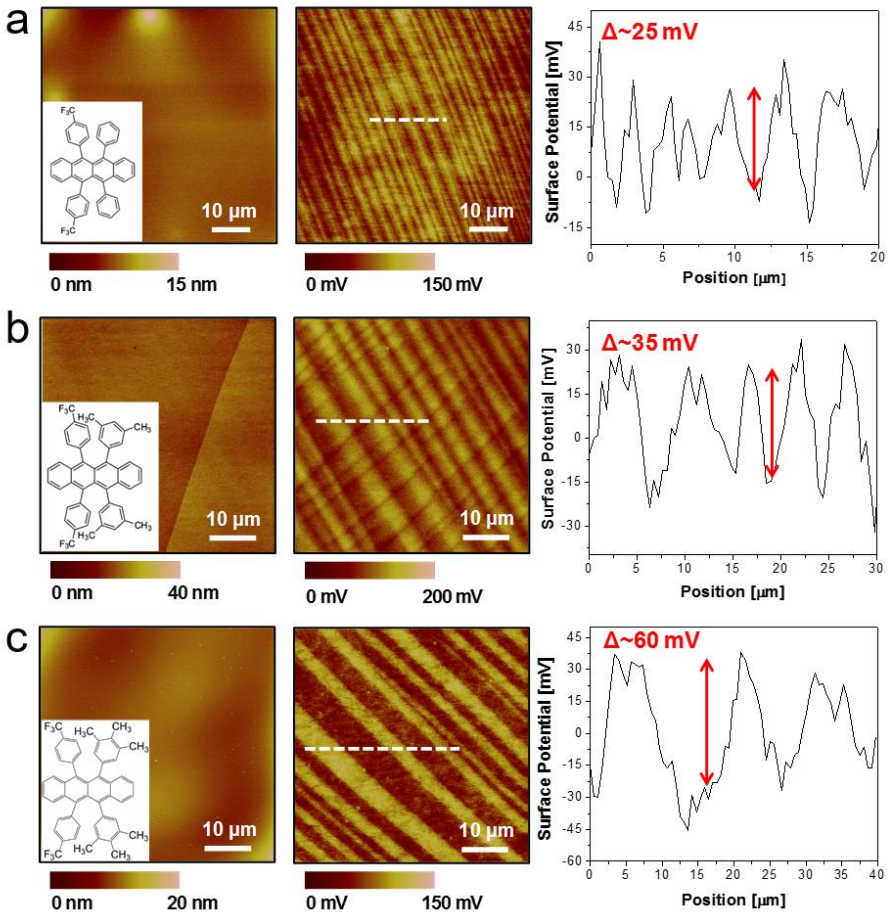

Figure 6.5 Potential stripes in other rubrene derivatives. (a) Topography, surface potential, and potential profile for F-rubrene (structure shown in inset). The profile corresponds to the white dashed line. The potential difference between the peaks and valleys in the potential profile is ~25 mV. (b) Topography, surface potential, and potential profile of the white dashed line for FM2-rubrene. The potential difference between the peaks and valleys in the potential profile is ~35 mV. (c) Topography, surface potential, and potential profile of the white dashed line for FM3-rubrene. The potential difference between the peaks and valleys in the potential profile is ~60 mV.

To explore the generality of our findings we investigated a number of other organic single crystals grown by physical vapor transport. Interestingly, the phenomenon observed in FM-rubrene is also commonly found in many other materials. **Figure 6.5** shows the SKPM results of three other rubrene derivatives with different numbers of $–CH_3$ and $–CF_3$ pendant groups. Parallel potential stripes are evident for all three derivatives although the

magnitudes of the potentials vary from one crystal to another. Furthermore, as shown in Appendix Figure A2.4, SKPM examinations of other organic semiconductor single crystals including p-type dinaphtho[2,3-b:2,3-f]thieno[3,2-b]thiophene (DNTT),[222] and n-type semiconductors buckminsterfullerene (C60),[223] and a naphthalene diimide derivative (Cl_2-NDI),[224] also show similar stripes. With this preliminary work, it appears to us that electronic and structural disorder is fairly common in a variety of organic semiconductor crystals. Rubrene, however, generally does not show surface potential domains and this may be key to its excellent FET transport characteristics.

6.4 Conclusions

In summary, SKPM reveals planar defects in a variety of organic semiconductor single crystals. In the case of FM-rubrene, the defects appear to result from a solid-solid phase transition that occurs on cooling from the growth temperature to room temperature. Significantly, the planar defects are not readily detectable by commonly employed characterization methods such as polarized light microscopy or conventional out-of-plane XRD, but are easily visualized by SKPM. The surface potentials associated with the defects represent electronic disorder, perhaps due to residual strains, and are likely to have high impact on the field effect transport properties of the crystals, for example by causing fluctuations in the HOMO and LUMO band-edge positions leading to barriers and traps for charge. Future experiments will focus on establishing a one-to-one correlation between the defect potentials and transport. Nevertheless, the current results highlight the utility of SKPM as a method of revealing correlated electronic and structural disorder in organic single crystals, which should help to advance the understanding of structure-property relationships in organic electronics.

6.5 Experimental methods

Single crystals investigated in this work were grown by physical vapor transport using ultrapure Ar as carrier gas.[78,79] The sublimation temperatures varied from ~200 °C (Cl_2-NDI) to ~600 °C (C60) depending on the types of organic materials. Only thin crystals (<5 μm) with uniform crystalline regions and smooth/clean surfaces were selected for sample preparation. Freshly made crystals were laminated onto PDMS substrates. Spontaneous adhesion of the crystals to the substrates occurred. In order to electrically ground the sample, vapor deposited gold film with thicknesses around 500 nm was removed from a Si substrate and transferred to cover part of the crystal by tweezers, and silver paint was then used to connect the gold film to the metal SKPM sample puck.

SKPM measurements were performed with a Bruker Nanoscope V Multimode 8 Scanning Probe Microscope, which works in a two pass "lift mode". In the first pass of each line of an image, the conductive probe scans the rubrene surface in attractive-regime dynamic mode to generate the topographic data under conventional amplitude-modulation feedback (also known as "AC" or "tapping" mode) while mechanically vibrating the cantilever near resonance. To stabilize performance in the attractive regime, the cantilever was driven at a drive frequency slightly larger (~150 Hz) than the fundamental resonant frequency, and the setpoint amplitude was about 90% of the free amplitude (~90 nm). In the second "interleave" pass, the probe was lifted to a constant height above the surface and scanned the topographic trajectory acquired in the first pass. A tip-applied AC bias resonantly excites the cantilever (via a time-varying electrostatic force gradient between tip and sample) while a DC bias was adjusted under feedback so as to *null* the AC excitation by matching (and thus measuring) the surface potential point-to-point across the surface.[225]

The measurements were carried out inside an argon-filled glove box with oxygen level <5 ppm. The typical probes were from Bruker (FMV-PT, Pt/Ir coated, resonant frequency ~75 kHz, spring constant ~2.8 N/m). The lift height during the second pass was 20 nm, which was beyond the range where van der Waals forces come into play. The applied AC voltage in SKPM was 0 to +6 V in amplitude. The SKPM images were analyzed using the freeware Gwyddion.

Ethanol was used as the etchant for chemical etching. The crystal samples were submerged into ethanol drops in an atmosphere saturated with ethanol vapor. After a desired etching period (from 30 min up to 3 hours), the sample was rinsed with a distilled water spray (~20 s) to quench the etching reaction. Isopropyl alcohol spray bottle rinse (~60 s) followed to remove residual organic buildup on the sample surface after chemical etching. The sample was thoroughly rinsed by distilled water spray again and was then dried with N_2 gas (~60 s).

High resolution in-plane (ϕ scan) and out-of-plane XRD measurements were carried out with a PANalytical X'Pert Pro X-ray diffractometer with a Cu Kα source (λ = 0.154 nm) operated at 45 kV and 40 mA filament current. The lattice parameters as a function of temperature for FM-rubrene and rubrene single crystals were determined by a Bruker SMART Platform CCD diffractometer using graphite-monochromated Mo Kα radiation (λ = 0.71073 Å) at temperatures from 283 K to 483 K with increments of 50 K.

Chapter 7 Rubrene Single-Crystal Transistors with Perfluoropolyether Liquid Dielectric: Exploiting Free Dipoles to Induce Charge Carriers at Organic Surfaces

We report the use of perfluoropolyether (PFPE) as a liquid dielectric for use in rubrene single-crystal transistors. In particular, we explore the effect of the free, permanent dipoles in PFPE on the charge carrier accumulation and transport at the rubrene/ PFPE interface. This provides a complementary approach to ionic liquid dielectrics where charge accumulation is achieved via mobile ions. Large hysteresis (i.e., a memory effect) in transistor transfer curves and peaks in the gate displacement current curves are observed and interpreted in terms of the dipolar response of PFPE to the gate electric field. The orientation of free dipoles in PFPE is found to have a significant influence on the formation and annihilation of the rubrene conducting channel. Hole densities on the order of 1011 cm−2 are achieved at the surface of rubrene, and a transition from band-like to hopping transport near the freezing point of PFPE is evidenced by temperature-dependent Hall effect and resistance measurements. Overall, the dipole-induced memory effect and the possibility of further increase in charge accumulation by increasing the dipole density suggest that liquids with free, permanent dipoles may be interesting dielectrics for use in field-effect transport experiments. This work has been published as *X. Ren, E. Schmidt, J. Walter, K. Ganguly, C. Leighton, and C. D. Frisbie, "Rubrene Single-Crystal Transistors with Perfluoropolyether Liquid Dielectric: Exploiting Free Dipoles to Induce Charge Carriers at Organic Surfaces", The Journal of Physical Chemistry C, 2017, 121, 6540*.

7.1 Introduction

Previously, we and others have advanced the use of liquids as gate dielectrics for field-effect transport experiments on organic single crystals.[97,125,137,138,144,226–228] For fundamental work, liquid dielectrics offer several advantages, including the possibility of tuning the dielectric constant over a wide range (e.g., 2-60), the possibility of introducing mobile ions facilitating electrical double layer formation, the ability to insert the liquid at room temperature thus minimizing crystal damage, and, in principle, the option to remove the liquid and return to an air-gap structure such that comparisons of transport with and without the liquid can be made.[97,138] Using this strategy, we have shown that the carrier mobility of systems such as rubrene systematically decreases as the liquid's dielectric constant increases, consistent with earlier findings for solid dielectrics.[93,138] We have also shown that it is possible to achieve extremely high charge carrier densities on the surface of rubrene crystals using ionic liquid electrolytes, which has allowed the observation of gate-induced near-metallic behavior, as well as intriguing peaks in conductance as a function of charge carrier density.[144,228]

Following initial work by Lee *et al.*, here we explore the use of a different liquid as a gate dielectric, namely the perfluorinated oligomer perfluoropolyether (PFPE), which has a free electric dipole with a moment of 0.4 Debye.[229] The density of these dipoles is ~10^{21} cm^{-3} and we could thus expect, based on Lee's work, that orientation of the dipoles under the influence of a gate electric field could lead to an enhancement of the charge carrier density on the surface of rubrene crystals. The earlier work by Lee *et al.* indeed showed that significant charge carrier densities, and a trap-healing effect, could be observed in resistivity measurements on rubrene in contact with PFPE. However, in that work field-

effect transistor (FET) geometries using PFPE as the dielectric were not investigated. Here, by making such PFPE-gated FETs and measuring gate displacement currents, FET transfer characteristics, and the Hall effect, we observe interesting and unusual charge accumulation effects, as well as achieving charge carrier densities that exceed the expected values based on the dielectric constant of PFPE (~4) alone. Specifically, due to the existence of dipole-induced charge (10^{10}-10^{11} cm^{-2}), we find a memory effect in the transfer curves of PFPE-gated rubrene transistors, which creates a 3-order-of-magnitude difference in the conductance near $V_G = 0$ depending on the prior gate voltage application history. We anticipate that a higher charge carrier density can be expected if a liquid with a larger dipole density is applied. Overall, the results point to intriguing opportunities to use dipolar liquids in field-effect transport experiments.

7.2 Displacement current measurements and transistor characteristics

Initially, the dielectric properties of PFPE were characterized by DCM on an MIM capacitor (**Figure 7.1a**). In **Figure 7.1b**, the currents are seen to be constant when sweeping in one direction and have similar magnitude but opposite sign when sweeping in the other direction, which are features of an ideal capacitor. From these DCM curves, we can extract the specific capacitance ($C_i = C/A$, where C is the total capacitance and A is the channel area) according to:

$$I_G = \frac{d(CV_G)}{dt} \approx AC_i \frac{dV_G}{dt} \tag{7.1}$$

The specific capacitance of the device shown in **Figure 7.1b** is 0.71 nF/cm^2, which corresponds to a dielectric constant of ~4 (Figure A3.1 in Appendix). These DCM data on MIM structures thus support the idea that PFPE can be used as a liquid dielectric in FETs,

the existence of a dipole moment appearing to have no observable effect on the performance of the MIM capacitor.

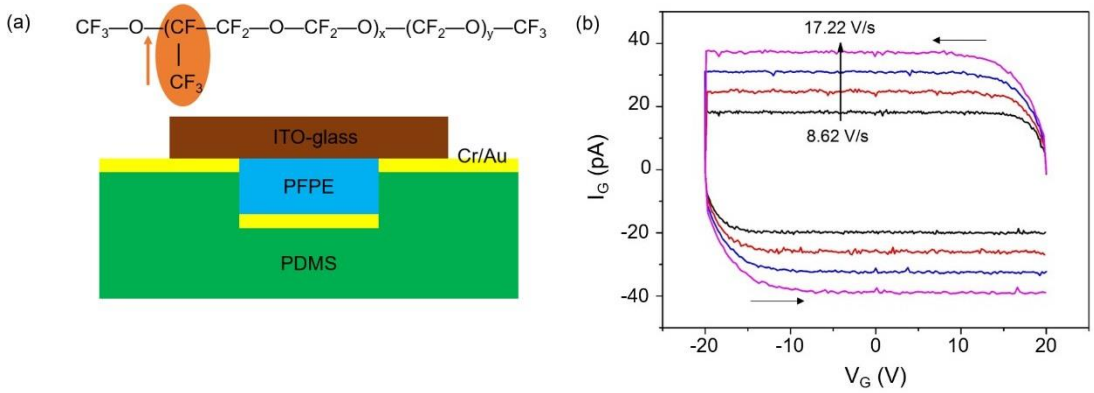

Figure 7.1 (a) Top: molecular structure of PFPE; Bottom: schematic cross-section of the PFPE MIM capacitor with dielectric thickness of 5 μm. (b) Displacement currents of the PFPE MIM capacitor with sweep rates from 8.62 to 17.22 V/s at 300 K. Device dimensions: L = 500 μm, W = 620 μm.

Before proceeding to employ PFPE as a dielectric material in rubrene FETs, rubrene air-gap devices were first fabricated and tested. The hole mobility was calculated in the linear regime from the standard FET equation (when $V_D << V_G - V_{TH}$):

$$I_D = \frac{W}{L} C_i \mu V_D (V_G - V_{TH}) \tag{7.2}$$

where W and L are respectively the width and length of the semiconducting channel, μ is the carrier mobility, and V_{TH} is the threshold voltage. The air-gap transistor shown in **Figure 7.2a** has a FET mobility of 14.5 $cm^2V^{-1}s^{-1}$, and the transfer curve is hysteresis free, both of which are typical for rubrene single crystal air-gap FETs. After selecting a high performance device such as this, the air-gap was then filled with PFPE liquid (see inset to **Figure 7.2b**) to carry out liquid-gating experiments. **Figure 7.2a** clearly shows that the transfer curve of the PFPE-gated device presents large hysteresis, which is absent in the air-gap device. Understanding the origin of this hysteresis, which is a central observation

of this work, is critical to understanding the operating mechanism. It is known from Lee *et al.*'s earlier work that the dipole moment in PFPE can cause charge accumulation at the rubrene/PFPE interface even without a gate voltage, and that the induced charge carrier density can be as high as 10^{10}-10^{11} cm^{-2}.[229] Thus, when the device in **Figure 7.2** is operating under a negative gate bias, the charge carrier density in the rubrene channel consists of two parts: a dipole-induced charge and a gate-induced charge. In the current work, since the device is tested under a gate bias, the dipole's response to the electric field must clearly be taken into consideration.

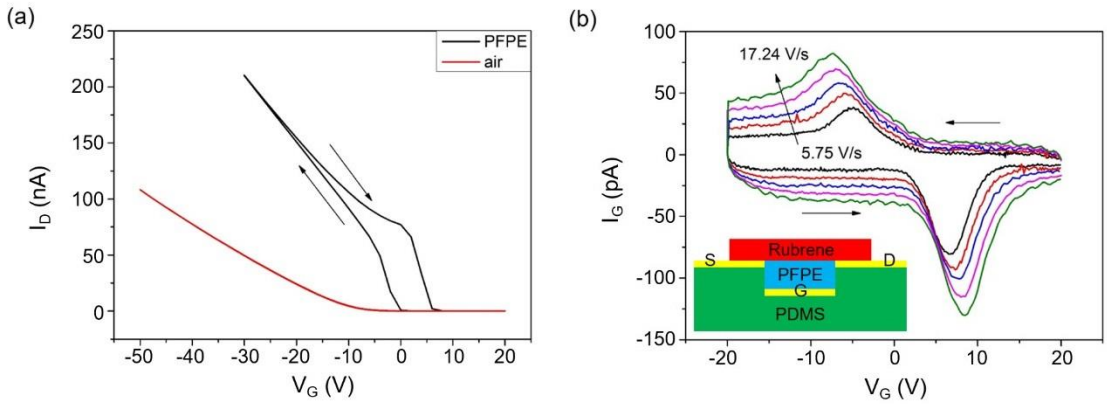

Figure 7.2 (a) Transfer curves of a rubrene single crystal transistor with different dielectrics at 300 K: air (red) and PFPE (black). Mobilities: μ_{air} = 14.5 $cm^2V^{-1}s^{-1}$, μ_{PFPE} = 6.3 $cm^2V^{-1}s^{-1}$. (b) Displacement currents of the PFPE-gated device with sweep rates from 5.75 to 17.24 V/s at 300 K (inset: device structure of the PFPE-gated rubrene FET). A large hysteresis appears in the transfer curve of the PFPE-gated device and two peaks are observed in the displacement currents. Device dimensions: L = 500 μm, W = 600 μm.

To study the response of the PFPE dipoles to sweeping gate voltages, we also measured the gate displacement currents of PFPE-gated rubrene FETs. In these measurements, the source/drain electrodes were grounded while the gate voltage was swept at various rates. DCMs have been widely used to study the charge injection properties of organic FETs (OFETs) with different dielectrics, including oxides and ionic liquids.[137,142,143] Interestingly, the DCM curves of PFPE-gated devices are very different from those of

devices with other dielectrics. In **Figure 7.2b**, for instance, regardless of the sweep rate, there are always two peaks in a single V_G loop. The peak in the forward sweep (from positive to negative voltage) appears at -5 V to -10 V, while the one in the reverse sweep appears at +5 V to +10 V. The existence of these peaks can be explained by a dipole flipping process under applied gate voltages. In the forward sweep, which indicates a hole injection process, the device turns on near $V_G = 0$ V (**Figure 7.2a**), and a pronounced DCM peak starts to form as the gate voltage is swept further negative (**Figure 7.2b**). This peak likely corresponds to the rearrangement of dipoles near the rubrene surface, and the simultaneous surge of positive charge into the channel upon reaching the threshold voltage. We note here that a peak in the forward scan of a displacement current curve only is typical in OFETs with conventional dielectrics, related to the formation of the conducting channel.[142] However, the magnitude of the peaks in these PFPE-gated rubrene FETs is much larger, indicating that the peaks in PFPE-gated FETs have a different origin. After the forward peak, the gate displacement current becomes nearly gate voltage-independent, which again is anticipated from similar experiments on OFETs with conventional dielectric materials.[143] During the reverse sweep, however, which corresponds to the hole extraction process, the displacement current is first flat and small for $V_G < 0$ V, and no turn-off is observed by 0 V, consistent with the hysteresis in the transfer curve. As the conductivity of the channel is still high at this point, we suppose, as discussed further below, that a large concentration of holes in the surface charge layer are "pinned" (though not trapped) by oriented dipoles at the rubrene/PFPE interface. Importantly, as the gate bias on the reverse sweep is scanned to positive values, a very large negative current peak occurs. We attribute this large negative peak to the flipping of the dipoles under the influence of the gate electric

field and the simultaneous release of holes from the rubrene accumulation layer into the source and drain contacts.

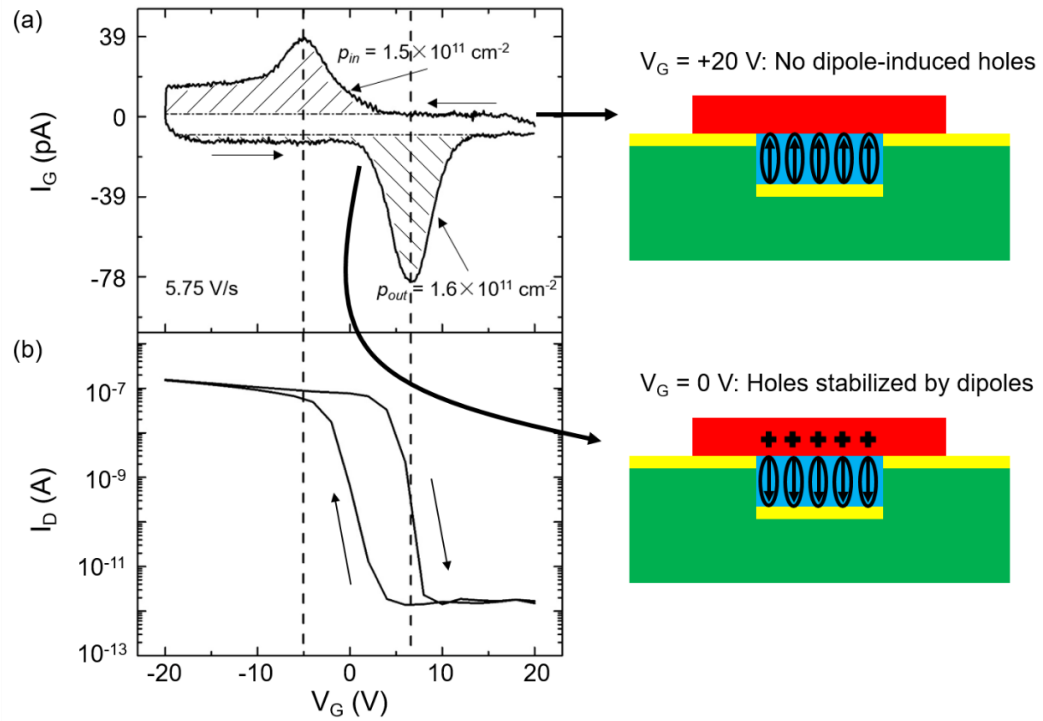

Figure 7.3 (a) Displacement current of a PFPE-gated rubrene FET (the same device shown in Figure 7.2) at 300 K. On the right are the schematics of dipole-induced hole accumulation at different gate voltages. (b) Semi-log-scale transfer curve of the same device at 300 K. The amounts of charge injected (p_{in}) and extracted (p_{out}) are also shown.

Within this picture, the hysteresis in the transfer curve and the peaks in the DCM curve are of course directly related. To better visualize this, the transfer curve is plotted in **Figure 7.3** on a semi-log scale, along with the DCM at a single sweep rate. Comparison of panels (a) and (b) clearly shows that the peak in the forward gate displacement sweep (**Figure 7.3a**) appears when the device is almost totally turned on (**Figure 7.3b**), and the peak in the reverse sweep appears as the device is turning off. It is worth noting here that the conductance hysteresis and DCM peaks only exist when PFPE is in the liquid state. When the PFPE is frozen, the dipoles cannot respond to the external electric field, so the dipole-

induced charge accumulation is no longer affected by the applied gate voltages, as would be expected (see Figures A3.2 and A3.3 in Appendix for more details).

The injected charge carrier density can be extracted from the forward sweep of the DCM curve in **Figure 7.3a** using Equation (7.3):

$$p = \frac{Q}{eA} = \frac{\int I_G dV_G}{\frac{dV_G}{dt} eA} \tag{7.3}$$

where e is the elementary electron charge. The integrated charge carrier density increases monotonically as a function of gate voltage and reaches 1.5×10^{11} cm^{-2} at V_G = -20 V. This charge carrier density is clearly larger than what could be expected from a conventional dielectric with $\varepsilon_r \sim 4$, which would give $p = 9 \times 10^{10}$ cm^{-2} at V_G = -20 V for a 5 μm thick dielectric. Moreover, the quantities of charge injected and extracted (on the reverse sweep) are very close (see **Figure 7.3a**), indicating a nearly trap-free rubrene/PFPE interface. The reverse peak in **Figure 7.3a** represents almost exclusively dipole-stabilized charge with a density of ~10^{11} cm^{-2} (it may vary with sweep rate), and its position on the voltage axis is consistent with the hysteresis in the transfer curve shown in **Figure 7.3b**.

Consistent with the above, we interpret the transfer curve hysteresis and related DCM peaks in PFPE-gated rubrene devices in terms of a pinned dipole model. The behavior is in fact somewhat reminiscent of a ferroelectric-gated device,[230] which we propose arises due to behavior analogous to an anisotropic paraelectric, where an energy barrier to dipole reversal develops. The induced rubrene surface charge density is made up by two contributions: that from conventional dielectric charging, and that from the PFPE dipole moments. The latter moments can be oriented under the applied electric field (as in a

paraelectric), but exhibit hysteresis in field response due to anisotropy and pinning, deriving from factors such as the interaction between the dipoles and induced charge carriers, and the steric effects associated with the PFPE chains to which the dipoles are connected. Critically in this context, it is apparent that the peaks seen in the DCM curves for the PFPE-gated FETs (**Figure 7.3a**) are absent in the DCM curves of the PFPE MIM capacitors (**Figure 7.1b**). One possible reason for this is that the dipole-induced charge interaction is fundamentally different in rubrene FETs and MIM devices. In the one case we have interaction between PFPE surface dipoles and relatively low mobility/ low density holes at a low dielectric constant (and thus low screening) organic semiconductor surface. In the other we have dipoles interacting with a metallic surface with more effective screening, which could reduce the pinning/anisotropy responsible for the hysteresis. Additional future work to understand this mechanism would be beneficial. We note, however, that we have verified that the hysteresis effect with PFPE also occurs in other p-type organic crystals FETs, such as those based on DNTT (see Figure A3.4 in Appendix), indicating that the phenomenon is indeed general to PFPE-based p-type FETs. We believe that the dipole-charge interaction in an n-type semiconductor would be different due to the asymmetric molecular structure of PFPE, though more experiments are required.

7.3 Hall effect and *R*–*T* measurements

The Hall effect, perhaps the most definitive method for studying charge transport in high mobility organic semiconductors, has been successfully performed on rubrene single crystal FETs with various dielectrics.[9,59,144] In pioneering work, Lee *et al.* reported the observation of the Hall effect at the surface of PFPE-functionalized rubrene single crystals with an excellent signal-to-noise ratio.[229] In this work, we thus performed Hall

measurements on PFPE-gated rubrene devices at various temperatures and gate voltages. **Figure 7.4a** shows the room temperature Hall resistance (defined as $R_{xy} = V_{xy}/I_D$, where V_{xy} is the Hall voltage) as a function of the magnetic flux density (B) at different gate voltages, with a scan rate of 0.01 T/s. A clear Hall signal with a positive slope was observed, consistent with hole-dominated conduction in rubrene. The hole density (p_{Hall}) and the Hall mobility (μ_{Hall}) were calculated using:

$$p_{Hall} = \frac{1}{eR_H} = \frac{B}{eR_{xy}} \tag{7.4}$$

$$\mu_{Hall} = \frac{\sigma}{ep_{Hall}} = \frac{R_{xy}}{BR_{xx}}\frac{\Delta L}{W} \tag{7.5}$$

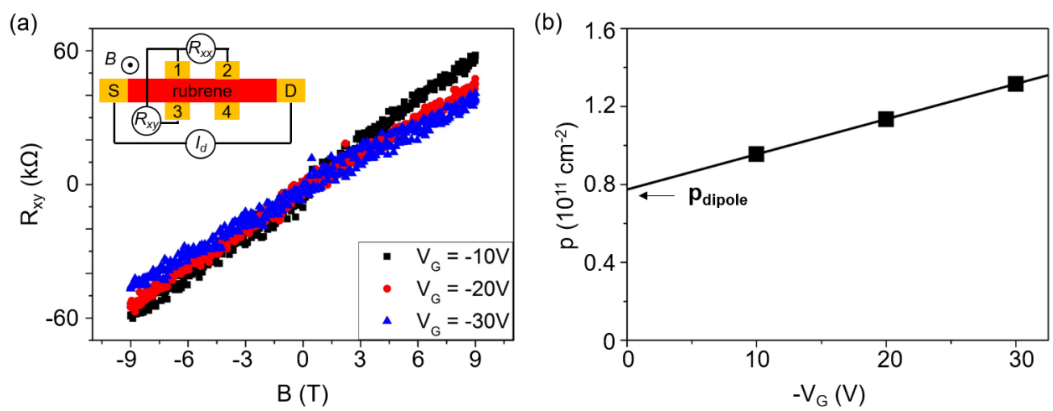

Figure 7.4 (a) Zero field background subtracted Hall resistance as a function of magnetic flux density at different V_G for a PFPE-gated FET at 300 K and I_D = 50 nA (inset: the Hall-bar geometry used in this experiment). (b) Hole density as a function of V_G at 300 K. The density of dipole-induced charge can be exacted from the intercept. Device dimensions: L = 1000 μm, ΔL = 250 μm, W = 250 μm.

where R_H is the Hall coefficient, ΔL and ΔV are respectively the distance and the potential difference between the two reference electrodes, and R_{xx} is the channel resistance, which is defined as $R_{xx} = \Delta V/I_d$. The charge carrier density (p_{Hall}) at different gate voltages is thus summarized in **Figure 7.4b**. Clearly, with the increase of the gate voltage, the charge

carrier density increases linearly. However, the fitted straight line that represents the p_{Hall} - V_G relationship does not go through the origin. Rather, it has an intercept of 7.7×10^{10} cm^{-2} at $V_G = 0$, which corresponds to the density of dipole-induced charge. The Hall data thus further confirm the earlier understanding that both dipole-induced charge and gate-induced charge must exist when these devices are in operation.

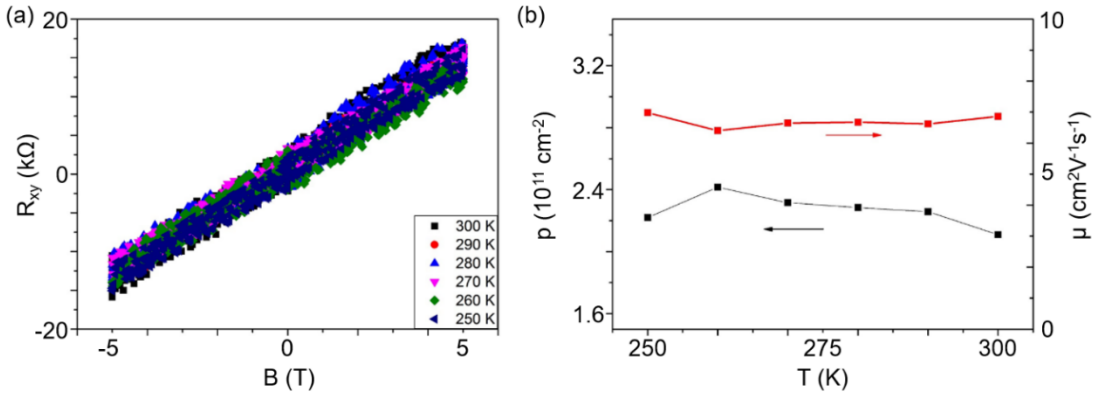

Figure 7.5 (a) Zero field background subtracted Hall resistance as a function of magnetic flux density at different temperatures for a different PFPE-gated FET at V_G = -30 V and I_D = 200 nA. (b) Hole density and Hall mobility as a function of temperature. The Hall mobility is nearly temperature-independent down to 250 K. Device dimensions: L = 1000 μm, ΔL = 150 μm, W = 300 μm.

The temperature dependence of the R_{xy} *vs*. B response is shown in **Figure 7.5a**. The gate voltage and source current were fixed here at -30 V and 200 nA respectively. The Hall signal is seen to possess a good signal-to-noise ratio between 300 K and 250 K (V_{xy} ~ 1 mV, V_{noise} < 0.1 mV), μ_{Hall} and p_{Hall} being nearly T-independent in this temperature range (**Figure 7.5b**). However, at only slightly lower temperatures, around 240 K, the Hall signal is abruptly suppressed (the apparent mobility shrinks by a factor of 2 in the space of only 10 K) and becomes distinctly noisier. This is shown quantitatively in Figure A3.5 in Appendix. The cause of this is apparently a sharp decrease in charge carrier mobility as the PFPE begins to freeze (the freezing point of PFPE is ~240 K).[231] To support this, we

measured the corresponding sheet resistance ($R_S = R_{xx}W/\Delta L$) as a function of temperature, again at a fixed gate voltage V_G = -30 V (**Figure 7.6**). Clearly, the R_S *vs*. T curve can be divided into two distinct regimes. Above ~250 K, the resistance decreases upon cooling, which corresponds to band-like transport, consistent with the Hall data of **Figure 7.5b**. Below 250 K, however, the resistance increases rapidly with decreasing temperature. This suggests a sharp crossover from band-like to strongly insulating transport (likely dominated by hopping), occurring very close to the freezing point of PFPE (~240 K).[231] It is thus concluded, intriguingly, that the solid-liquid phase transition in PFPE strongly influences the channel resistance in PFPE-gated rubrene single crystal FETs, even when cooling in the "ON" state.

One possible explanation is that the dipoles' ability to fluctuate is important for detrapping of charge carriers in rubrene. Specifically, the local electrical field produced by the dipoles no doubt causes potential corrugation at the PFPE/rubrene interface, affecting charge transport in the rubrene. In the liquid state, the dipoles can fluctuate (e.g., in displacement or orientation with respect to the rubrene surface), and therefore the potential corrugation is dynamic, which could potentially assist in freeing charge carriers from traps. Below the freezing point, however, the dipoles are immobilized, and so the potential corrugation becomes static. Another possible factor is that as the liquid cools and approaches the freezing point, the contraction of liquid also creates a number of microscopic-delamination sites across the PFPE/rubrene interface. These delamination sites would experience weakened electric field compared to the surrounding areas, and act as trap sites for charge carriers, ultimately resulting in percolative transport. We suggest

that more studies must be done in this area to further explore this phenomenon, including possible links to the hysteresis effects in transfer curves, and DCM peaks.

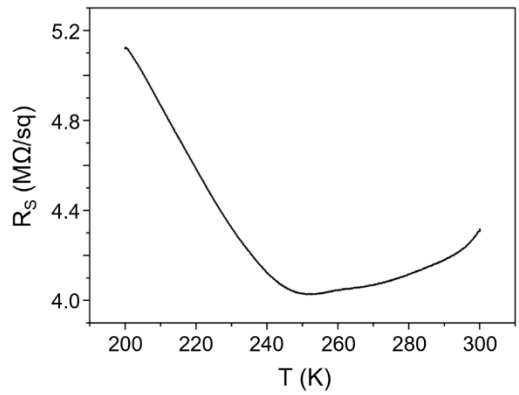

Figure 7.6 Sheet resistance as a function of temperature for the same PFPE-gated FET shown in Figure 7.5 at V_G = -30 V. There is a clear transition near the freezing point of PFPE.

7.4 Conclusions

In summary, we have investigated the electrical transport properties of PFPE-gated rubrene single crystal FETs. Using various electrical characterization methods, room temperature mobilities over 6 $cm^2V^{-1}s^{-1}$ and charge densities over 10^{11} cm^{-2} have been obtained. This mobility is lower than the air-gap mobility (> 10 $cm^2V^{-1}s^{-1}$), consistent with the well-known result that as the dielectric constant increases, the mobility decreases.[93] The dipole moment present in the structure of PFPE is found to play a significant role in the transport behavior of PFPE-gated devices, being responsible for the high carrier density at the PFPE/rubrene interface. The dipole-rubrene interaction also results in large hysteresis in FET transfer curves and peaks in the gate displacement current, which are conspicuously absent in MIM capacitors or rubrene FETs with other dielectrics. We interpret this in terms of behavior analogous to a pinned/anisotropic paraelectric. The charge transport properties of PFPE-gated devices were also studied by Hall measurements, which show a

temperature-independent Hall mobility above the freezing point of PFPE. Below the freezing point, however, the Hall coefficient shrinks and becomes abruptly lower in signal-to-noise ratio, coincident with a clear crossover from band-like to hopping in channel resistance *vs*. *T*. These observations indicate that the liquid-solid transition in PFPE has a surprising influence on the conduction in the rubrene channel, even in the "ON" state. Collectively, these results demonstrate that PFPE, which integrates surface functionalization into the dielectric layer, can be a promising liquid dielectric material to study the influence of free dipoles on charge accumulation and transport at semiconductor/dielectric interfaces in OFETs. Additional future work to further understand the hysteretic gate voltage dependence and temperature dependence of such devices is clearly worthwhile.

7.5 Experimental methods

Rubrene and PFPE (LVAC 25/6) were purchased from Sigma Aldrich. Rubrene single crystals were grown from the vapor phase using the horizontal physical vapor transport (PVT) method with a source temperature of 280-290 °C.[78,79] Polydimethylsiloxane (PDMS, Dow Corning Sylgard® 184) stamps with an air-gap structure (depth ~5 μm) were prepared according to previous publications.[88] Cr/Au (3/20 nm) electrodes were then deposited onto the PDMS stamps using a CHA e-beam evaporator to form the source, drain and gate contacts. Air-gap FETs were fabricated by laminating rubrene single crystals with smooth surfaces across the source/drain electrodes. The performance of air-gap devices was first tested, and then the gap was filled with PFPE liquid, with the aid of capillarity, to fabricate PFPE-gated devices. For the fabrication of metal-insulator-metal (MIM) capacitors, a small

piece of ITO glass (Delta Technologies) was laminated onto the PDMS substrate to act as the top electrode, and the gap was then filled with PFPE liquid.

Current-voltage (*I*-*V*) characteristics and gate displacement currents of air-gap and PFPE-gated rubrene single crystal FETs were measured in a Desert Cryogenics (Lakeshore Inc.) vacuum probe station equipped with a Lakeshore 331 temperature controller in a glove box filled with nitrogen gas. For transfer curves, two Keithley 236/237 source-measure units (SMUs) were used to apply the drain/gate voltages (V_D and V_G) and measure the resulting currents (I_D and I_G), and a Keithley 2612 SMU was used to ground and measure the source current (I_S). The displacement current measurements (DCMs) were taken by a Keithley 2612 SMU, which swept the gate voltage and measured the displacement current through the grounded source/drain contacts. Temperature- and field-dependent Hall effect measurements and resistance *vs*. temperature (*R vs*. *T*) measurements were conducted in a Physical Property Measurement System (PPMS, Quantum Design) with a 9 T superconducting magnet. A Keithley 2400 SMU was used to apply the gate voltage, and a Keithley 220 source unit and Keithley 2002 electrometer, respectively, were used to source current and measure voltage. To prepare devices for Hall measurements, the crystal was laminated on the PDMS substrate with a pre-patterned Hall-bar geometry. The sample was then wired on the PPMS puck using Au wires (25 μm diameter) and Ag paint.

Chapter 8 Anomalous Cooling-Rate-Dependent Charge Transport in Electrolyte-Gated Rubrene Crystals

Although electrolyte gating has been demonstrated to enable control of electronic phase transitions in many materials, long sought-after gate-induced insulator–metal transitions in organic semiconductors remain elusive. To better understand limiting factors in this regard, here we report detailed wide-range resistance–temperature (R–T) measurements at multiple gate voltages on ionic-liquid gated rubrene single crystals. Focusing on the previously observed high-bias regime where conductance anomalously decreases with increasing bias magnitude, we uncover two surprising (and related) features. First, distinctly cooling-rate-dependent transport is detected for the first time. Second, power law R–T is observed over a significant T window, which is highly unusual in an insulator. These features are discussed in terms of electronic disorder at the rubrene/ionic liquid interface influenced by (i) cooling-rate-dependent structural order in the ionic liquid and (ii) the intriguing possibility of a gate-induced glassy short-range charge-ordered state in rubrene. These results expose new physics at the gated rubrene surface, pointing to exciting new directions in the field. This work has been published as *X. Ren, C. D. Frisbie, and C. Leighton, "Anomalous Cooling-Rate-Dependent Charge Transport in Electrolyte-Gated Rubrene Crystals", The Journal of Physical Chemistry Letter, 2018, 9, 4828*.

8.1 Introduction

Electrolyte gating in the field-effect transistor (FET) geometry has emerged as an effective technique to induce very high charge carrier densities (10^{13} to 10^{15} cm^{-2}) at surfaces.[97,232,233] Accumulation of such charge densities has led to a series of breakthroughs in electrical control of ground states, including gate-induced insulator-metal transitions,

superconductivity, and ferromagnetism.[118,134,148,151,157–164,167,234] These achievements have been largely limited to electrolyte-gated transistors (EGTs) based on *inorganic* materials, however, such as oxides and 2D materials. Although tuning transitions among electronic ground states in *organic* conductors has been an active area since the 1970s, the techniques used to control charge density (e.g., chemical doping[235,236], charge-transfer interactions[237,238], *etc*.) are discrete and irreversible. Notably, gate-tuned electronic phase transitions such as insulator-metal transitions, or even superconducting transitions, remain elusive in organic semiconductor EGTs.

Driven by the above, several recent studies have reported EGTs based on single crystals of the benchmark organic semiconductor rubrene, which exhibits high hole mobility (>10 $cm^2V^{-1}s^{-1}$) and band-like transport in air-gap trnasistors.[115,137,144,226,239] High hole densities (of order 10^{13} cm^{-2}) have been induced on the surface of rubrene crystals using ionic liquid (IL) electrolytes, but, critically, *without* an insulator-metal transition. Rather, poorly understood conductance peaks have been observed *vs*. gate voltage (V_G), where the conductance *decreases* at the highest V_G magnitudes.[137,144] Temperature (T)-dependent measurements reveal conventional (activated or hopping-based) insulating transport at low $|V_G|$, near-metallic behavior at the conductance peak, but then reentrance of anomalous, strongly-localized transport at the highest $|V_G|$. Remarkably, near the conductance peak the resistance decreases on cooling to as low as 120 K, reaching within a factor of 2 of h/e^2.[144] This is tantalizingly close to a 2D insulator-metal transition, and it is thus imperative to understand the reentrance of strongly insulating behavior at high $|V_G|$.

While the origin of the unusual transport at the highest hole densities in rubrene is unclear, previous results suggest a key role for the rubrene/IL interface. Intrinsic

electrostatic doping (without gate bias) and free carrier saturation have been observed at the rubrene/IL interface by charge modulation spectroscopy, for example, which are not present in rubrene FETs with conventional dielectrics.[240] It has also been observed that the sizes of the ions in ILs impact device performance and peak mobility in rubrene EGTs, indicating that the Coulomb corrugation potential experienced by holes at the rubrene surface could be a limiting factor (unpublished results). Several studies have in fact suggested a role for interfacial electrostatic disorder at high bias in rubrene EGTs.[228,241] Better understanding of the ion-hole interaction at the IL/rubrene interface would thus provide vital insight, both for device optimization and realization of metallicity on the rubrene surface.

In this work we have performed systematic wide T range resistance-temperature (R-T) measurements on IL-gated rubrene crystals at multiple gate voltages and cooling rates. Consistent with earlier observations,[144] with increasing $|V_G|$ the transport mechanism is found to crossover from thermally-activated to a highly unusual power law T dependence. More surprisingly, in the anomalous power law regime, devices are found to exhibit distinctly cooling-rate-dependent R-T. Specifically, significantly smaller resistances are achieved at low T (e.g., 50 K) when cooled from high T (e.g., 240 K) at faster cooling rates. These observations are discussed in terms of likely differences in structural order on the IL side of the IL/rubrene interface at different cooling rates, thereby influencing interfacial electrostatic disorder. Inspired by recent observations in related organic conductors,[242] the fascinating possibility of glassy behavior due to geometrically-frustrated short-range charge-order at fractional filling is also discussed.

8.2 Cooling-rate-dependent *R*–*T* measurements

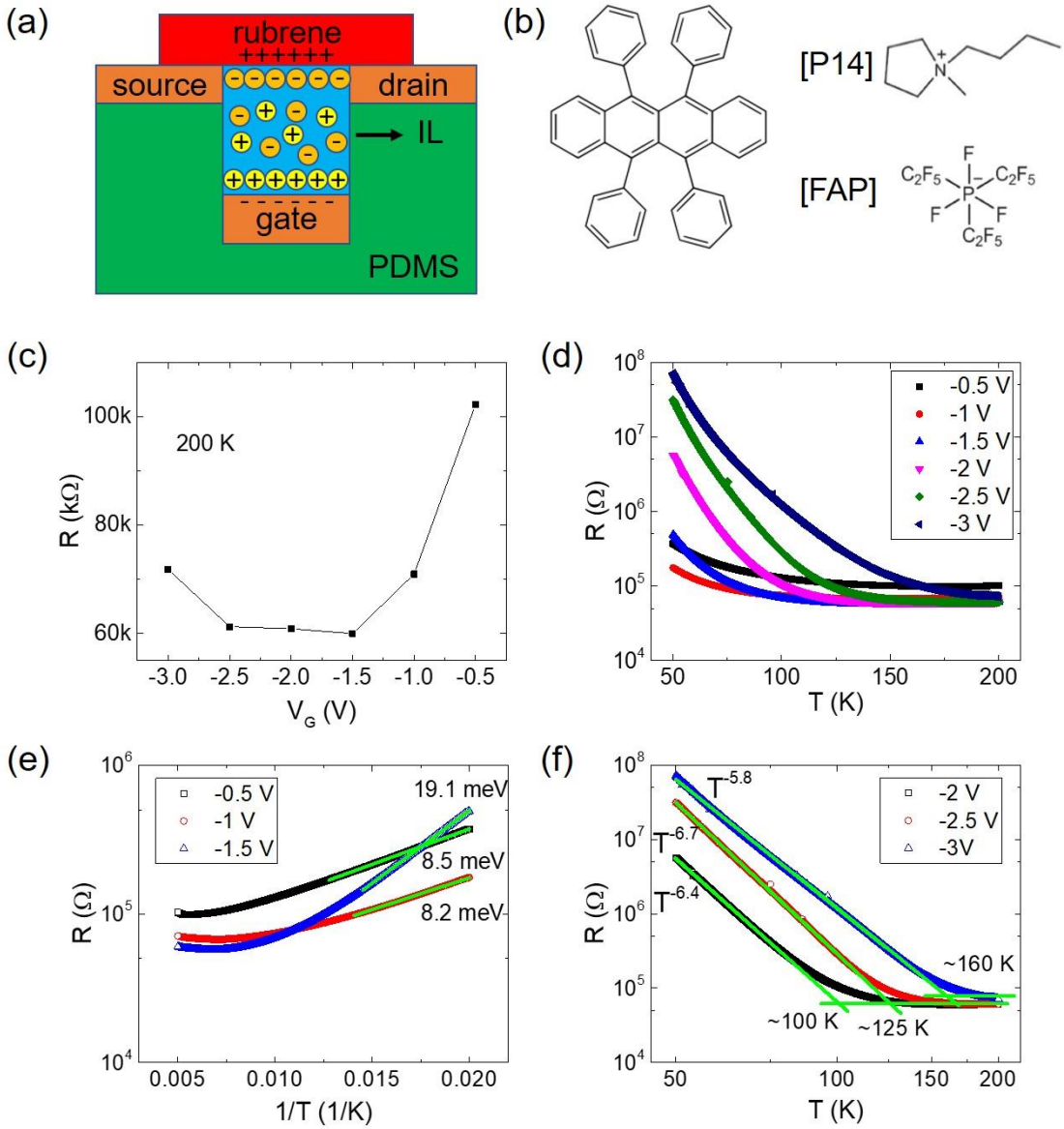

Figure 8.1 (a) Cross-sectional device structure of a rubrene EGT. (b) Molecular structures of rubrene (left) and [P14][FAP] (right). (c) V_G-dependent sheet resistance of a rubrene EGT at 200 K. (d) *T* dependence of the sheet resistance (log scale) at each V_G shown in (c), at a 1 K/min cooling rate. (e) Arrhenius plots (log*R* vs. 1/*T*) for V_G = -0.5 V, -1 V, and -1.5 V. Extracted activation energies are shown. (f) Log-log plot of *R*-*T* for V_G = -2 V, -2.5 V, and -3 V. Shown are the onset temperatures of power law behavior, and the extracted exponents. Data shown in (e) and (f) are the same as shown in (d). All *R*-*T* data are taken on warming.

Rubrene EGTs were fabricated on polydimethylsiloxane (PDMS) stamps by first fabricating air-gap transistors and then filling the gap with IL (**Figure 8.1a**).[137,138] The IL [1-butyl-1-methylpyrrolidinium][tris(pentafluoroethyl)trifluorophosphate] ([P14][FAP], **Figure 8.1b**) was chosen here as it provides a large V_G stability window.[137] Because of the mechanical rigidity of the frozen IL, such rubrene EGTs can survive to much lower temperatures than air-gap transistors by overcoming the thermal expansion mismatch between PDMS and rubrene. All electronic transport measurements were performed in a standard cryostat (a Quantum Design Physical Property Measurement System) with 4-terminal methods. *R-T* data were taken both on cooling and warming, after cooling at the rates specified. More details on experimental methods are given in Chapter 8.5.

The R-V_G relationship at 200 K in a typical rubrene EGT is shown in **Figure 8.1c**. Note that these data were not acquired by sweeping V_G, due to the freezing point of the IL. Instead, V_G was applied at 240 K, above the freezing point, and then the temperature lowered to 200 K to record each R value. (For a typical 300 K EGT transfer curve, see Figure A4.1 in Appendix). Clearly, from **Figure 8.1c**, R-V_G is nonmonotonic. As V_G is driven from zero to -1.5 V the resistance decreases, as expected, but then at $V_G < -1.5$ V an anomalous resistance *increase* sets in. As discussed above, such conductance peaks are common in EGTs based on organic crystals and polymers, arising due to a poorly understood mobility maximum.[137,144,241,243] As in our prior work on rubrene, the minimum resistance here is within a factor of 2 of h/e^2, indicating proximity to a 2D metallic phase. Corresponding *R-T* characteristics at a cooling rate of 1K/min are shown in **Figure 8.1d**, where the nonmonotonic V_G response is again apparent. *R-T* is relatively weak at small $|V_G|$ (-0.5 to -1.5 V), but at $V_G \leq -2$ V the resistance is first flat down to some T, before increasing

rapidly at lower T. As shown in **Figure 8.1e**, at -0.5, -1 and -1.5 V, R-T at low T can be well fit by an Arrhenius function, $R \propto \exp(-E_A/k_BT)$, with E_A as low as 8.2 meV at -1 V. At -2, -2.5 and -3 V, however, the log$R$-log$T$ plot in **Figure 8.1f** illustrates highly unusual power law T-dependence, *i.e.*, $R \propto T^{-n}$, with n consistently around 6. Note that the power law R-T turns on abruptly below some fairly well-defined (V_G-dependent) $T \approx$ 100-160 K, and that it is obeyed over substantial T and V_G windows. Zabrodskii plots[244] (Figure A4.2 in Appendix) confirm the crossover from thermally-activated to power law behavior, consistent with our previous publication.[144] This behavior is thus reproducible across devices.

In addition to these relatively slow cooling rate (1 K/min) R-T measurements, data were also acquired on the same device (**Figure 8.2**) at order-of-magnitude faster cooling rates (10 K/min). The cooling rate is seen to have negligible impact for V_G = -1 and -1.5 V (**Figures 8.2a and 8.2b**). For V_G = -2 and -2.5 V, however, in the anomalous high bias regime, substantially smaller low T resistance is found after fast cooling (**Figures 8.2c and 8.2d**). Significantly, this provides clear evidence of a kinetic effect in charge transport at large $|V_G|$ in rubrene EGTs, which was apparently overlooked in prior work. At high cooling rates such as 10 K/min, the rubrene surface at low T is somehow kinetically-trapped in a different electronic state to when it is cooled more slowly. Importantly, in the "fast-cooled" state the resistance at low T is *smaller* than at slow cooling rates, *i.e.*, fast cooling is beneficial for charge transport.

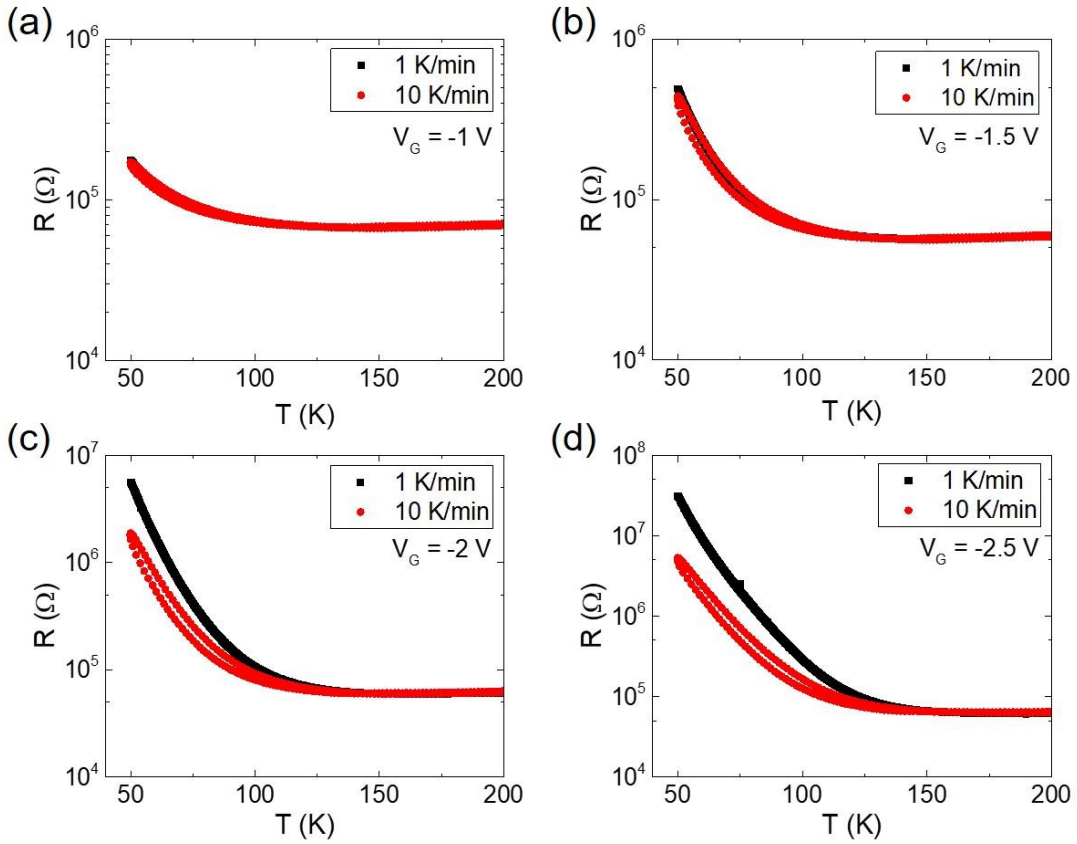

Figure 8.2 Cooling rate-dependent *R-T* curves (log scale), from the same device shown in Figure 8.1, at different gate voltages: (a) -1 V; (b) -1.5 V; (c) -2 V; (d) -2.5 V. All data are shown at cooling rates of 1K/min and 10 K/min. Note the clear cooling rate dependence in (c) and (d). All data are taken on both cooling and warming.

It should be emphasized that cooling-rate-dependence is only observed in the anomalous high bias regime, coincident with power law *R-T*, i.e., the onset of the two unusual phenomena reported here is simultaneous. **Figure 8.3a** illustrates this by summarizing the cooling rate dependence of *R-T* for 6 devices. Two new parameters are defined to this end. The first is the ratio of slow-cooling to fast-cooling resistances, R_{slow}/R_{fast}, which is 1 in the absence of cooling rate dependence, but >1 in the presence of cooling rate dependence. The second parameter is V^*, the V_G at which power law *T*-dependence is first detected. This latter parameter is introduced to enable facile comparison between devices, which tend to have slightly different onsets of power-law *R-T*. **Figure 8.3a** plots R_{slow}/R_{fast} *vs*.

$|V_G|$-$|V^*|$, vividly illustrating that cooling rate-dependent *R-T* turns on simultaneously with the crossover from thermally-activated to power law *R-T*; the vertical dashed line marks the transition between these two regimes.

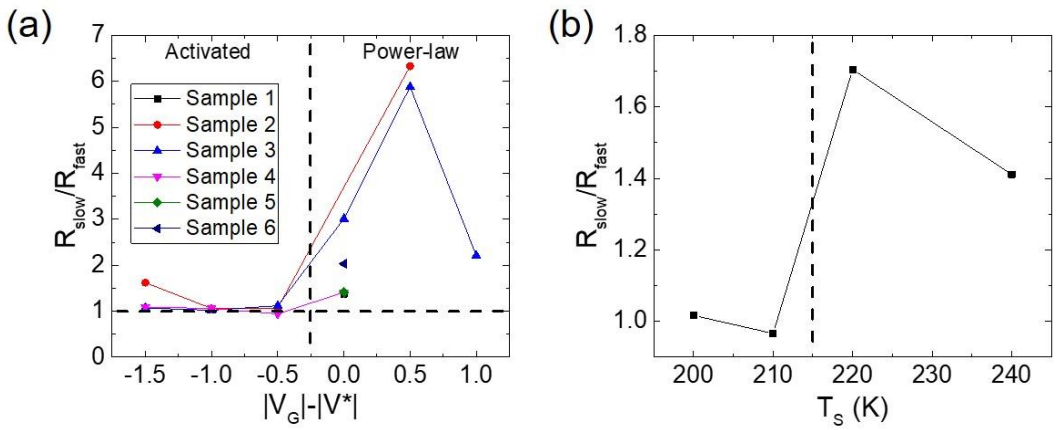

Figure 8.3 (a) Summary of the cooling rate dependence of the resistance at different gate voltages for 6 different devices. R_{slow}/R_{fast} (50 K), *i.e.*, the ratio of 50 K resistances at 1 K/min and 10 K/min cooling rates, is plotted *vs*. the magnitude of V_G-V^*. V^* is defined in the text. Note the simultaneous onset of cooling rate dependence in all devices, coinciding with power law *R-T*. The starting temperature T_S is 240 K here. (b) Influence of T_S on R_{slow}/R_{fast} (50 K). Note that these data were taken from another device to those shown in Figs. 8.1-8.2. A critical temperature is expected (dashed line) between 210 K and 220 K. Here the device was first slowly cooled from 240 K to *Ts*, then fast-cooled to 50 K.

Additional information was obtained by varying the starting temperature (T_s) for fast-cooling. To do this, devices were first slowly cooled at 1 K/min from 240 K down to some temperature T_s, below which they were fast-cooled at 10 K/min. R_{slow}/R_{fast} at T = 50 K is then plotted as a function of T_s in **Figure 8.3b**. Significantly, a critical T_s between 210 and 220 K (vertical dashed line) is discovered, below which R_{slow}/R_{fast} is very close to 1, i.e., there is no cooling rate dependence. This critical temperature coincides remarkably with the freezing point of the IL, [P14][FAP]. As shown in Figures A4.3 and A4.4 in Appendix, differential scanning calorimetry (DSC) and transport measurements indicate that the freezing point of [P14][FAP] is ~215 K. It is thus the cooling rate *across the freezing point of the IL* that affects transport in IL-gated rubrene EGTs. Fast cooling from temperatures

below this has no influence on the electronic state, whereas fast cooling from above this does. Complementary to the above, we also performed experiments where fast cooling (at 10 K/min) was done from 240 to 200 K, followed by slow cooling to 50 K at 1 K/min. *R-T* under these conditions is identical to that obtained when the device is simply cooled to 50 K at 10 K/min (Figure A4.4b in Appendix). The dynamics of freezing of the IL are thus clearly important.

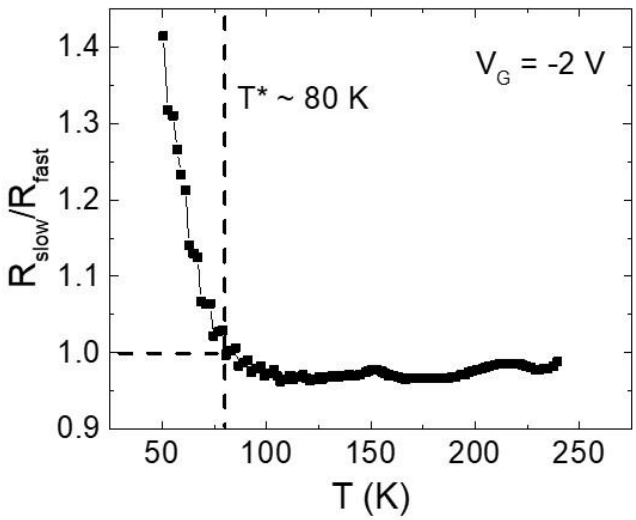

Figure 8.4 R_{slow}/R_{fast}, *i.e.*, the ratio of resistances at 1 K/min and 10 K/min cooling rates, as a function of temperature. Note that these data were taken from another device to those shown in Figs. 8.1-8.3 (device dimensions: L = 150 μm, ΔL = 70 μm, W = 370 μm). A T^* ≈ 80 K is obtained.

A final observation is provided in **Figure 8.4**, which plots $R_{slow}/R_{fast}(T)$, comparing 1 K/min and 10 K/min cooling rates at V_G = -2 V. A clear onset temperature, T^*, is uncovered, below which cooling rate dependence kicks in. Although the device studied here is not identical to **Figure 8.1**, note that T^* is quite similar to the point at which the resistance dramatically increases on cooling, following the anomalous power law *R-T*. Intriguingly, this T^* is far beneath the IL freezing point. This indicates that although it is cooling across

the IL freezing point that plays such an important role (**Figure 8.3b**), the cooling-rate-dependent *R*-*T* does not develop until much lower *T*.

8.3 Possible explanations

In terms of discussion of the above observations, we first note that it is known that the low *T* solid-state structure of ILs can be influenced by cooling conditions.[245] To demonstrate this in our [P14][FAP], DSC measurements were performed at different cooling rates (Figure A4.3 in Appendix). A freezing peak was clearly observed at 1 K/min, but was suppressed at 10 K/min. The solid phase of [P14][FAP] thus exhibits stronger crystalline order when slow-cooled at 1 K/min, but is more glassy (amorphous) when fast-cooled at 10 K/min. We propose that this provides a viable explanation for cooling-rate-dependent *R*-*T* in rubrene/IL EGTs. Specifically, the electrostatic disorder experienced by holes at the rubrene surface due to the arrangement of ions in the IL is very likely influenced by the (cooling-rate-dependent) degree of ionic ordering. Interfacial electrostatic disorder in rubrene/IL devices has been discussed in terms of Coulomb-mediated trapping of holes at clusters of anions.[228,241] These anion clusters emerge at negative V_G, from the anion/cation checkerboard anticipated on the IL side of the interface at $V_G = 0$. Hole conduction on the rubrene side of the interface is then percolative, occurring through a network of trap-free sites.[228,241] In this picture, or related ones, reduced crystalline order in the IL at fast cooling rates could result in a less ordered arrangement of traps. This IL configuration, as opposed to a more rigid crystalline one, could then be beneficial for percolative hole transport, thus explaining lower resistance after fast cooling. Within this picture, electrostatic disorder at the rubrene/IL interface is also likely responsible for the power law *R*-*T*, and we hope that this work will stimulate further theory

in this context. Multiphonon hopping is one mechanism for power law *T*-dependence in insulators, but is usually observed only in highly disordered systems, such as amorphous semiconductors, very different to single crystal rubrene.[246,247]

We also discuss another class of phenomena that could potentially explain our results: charge ordering. Recently, a number of organic conductors, such as BEDT-TTF-based compounds (bis(ethylenedithio)tetrathiafulvalene) have been found to display charge ordering.[242,248–250] In these materials an equilateral triangular structural motif leads to geometric frustration of charge ordering at fractional (1/4) filling. This leads to a short-range charge-ordered cluster glass, with strongly cooling-rate-dependent *R*-*T*, strikingly similar to our data on rubrene in some cases.[242] Highly significant in this context is that the molecular arrangement in the close-packing plane of rubrene is essentially identical to that of the conducting plane of BEDT-TTF compounds. Both have herringbone motifs, the rubrene lattice in fact being even closer to an ideal equilateral triangle.[201] Strong geometric frustration of charge order could thus be anticipated in rubrene. Moreover, the hole densities accumulated at the rubrene surface in EGTs are in the mid-10^{13} cm^{-2} range (Figure A4.1 in Appendix and ref. [144]), corresponding to 1/3 to 1/4 filling, as in the reported charge cluster glasses.

A short-range charge-ordered cluster glass analogous to that seen in the BEDT-TTF compounds could potentially provide qualitative explanations for many aspects of our data. First, the sharp onset temperatures for strongly insulating behavior in **Figure 8.1f** could correspond to V_G-dependent charge ordering temperatures, thus explaining the overall increase in resistance at high $|V_G|$ (**Figure 8.1c**), as fractional filling (e.g., ¼) is approached. The cooling-rate-dependent *R*-*T* of **Figure 8.2c,d** would then be natural, arising from the

glassy short-range charge-ordered state, i.e., kinetic avoidance of charge-order at high cooling rate. This would also qualitatively explain the data of **Figure 8.4**, where R_{slow}/R_{fast} turns on sharply, reminiscent of a phase transition, at a temperature T^*. Importantly, in certain charge-ordered systems, such as $La_{1-x}Sr_xFeO_3$, the unusual power law *R*-*T* we report here has also been observed.[251] While this is not well understood, it nevertheless points to an important additional parallel with charge-ordered systems. While challenging, we note that *in operando* synchrotron X-ray scattering on rubrene EGTs at high bias could potentially provide a test for charge cluster glass behavior.

Finally, we note that one aspect of our data is difficult to understand within either of the pictures advanced. Specifically, it is difficult to reconcile that the onset of power law *R*-*T* and strong cooling-rate dependence occurs below ~160 K (**Figures 8.1f, 8.2c,d and 8.4**), while the temperature important for cooling rate dependence is 210-220 K, i.e., the freezing point of the IL (**Figure 8.3b**). Within the picture of cooling-dependent structural ordering in the IL, it is difficult to understand why cooling rate dependence in *R*-*T* only emerges far below the 215 K freezing point. Similarly, within the charge cluster glass picture, it is difficult to understand why the IL freezing point is so important. In fact, additional experiments show that changing the cooling rate across the putative charge ordering temperature T^* has no impact on *R*-*T* (Figure A4.5 in Appendix). One possible resolution involves interplay, across the interface, between rubrene charge ordering and IL structural ordering. Unlike the BEDT-TTF systems, the rubrene here is electrostatically-doped *via* electric double layers. Since the electric double layer configuration will be different at different cooling rates, different charge-ordered states in the rubrene could be anticipated, and these may be frozen in below 215 K.

8.4 Conclusions

In summary, we have reported extensive V_G- and cooling-rate-dependent *R-T* measurements on a benchmark organic semiconductor/electrolyte interface: rubrene/[P14][FAP]. The anomalous high gate bias regime was studied, where a reentrant strongly insulating state prevents a 2D insulator-metal transition. In this regime we find a crossover from thermally-activated to power-law *T*-dependence, as well as significant cooling-rate dependence, apparently overlooked in prior work. These results have been thoroughly discussed in terms of cooling-rate-dependent structural ordering in the ionic liquid, as well as possible short-range frustrated charge-ordering near fractional filling. This work thus not only uncovers new physics at the rubrene/IL interface, but points to clear need for additional experimental and theoretical work.

8.5 Experimental methods

Rubrene and [P14][FAP] ILs were purchased from Sigma-Aldrich. Rubrene crystals were grown by physical vapor transport,[78,79] and device fabrication was based on previously established methods.[88] First, a four-terminal rubrene air-gap transistor was fabricated on a patterned PDMS (Dow Sylgard®184) substrate by laminating a rubrene crystal across the channel so that the *bc* crystal plane of rubrene (space group *Cmca*) is gated. The metal electrodes were formed by e-beam evaporation of Cr/Au (3/20 nm) prior to crystal lamination. Devices dimensions are: channel length L = 150 μm, distance between 2 voltage-sensing probes ΔL = 70 μm. Channel width W is determined by the width of the rubrene crystal, which is in the range of 200-600 μm. Next, a droplet of IL was dragged by a probe tip to fill the air-gap by capillarity, thus completing the fabrication process. For electrical characterization, devices were loaded into a Quantum Design

Physical Property Measurement System and cooled to 240 K to apply V_G. To measure *R-T* characteristics, V_G was held constant while the device was cooled down to 50 K at desired cooling rates. A Keithley 2612B source-measure unit and a Keithley 2002 multimeter were used to measure DC resistance between 50 K and 240 K at a constant drain voltage of 0.1 V.

Chapter 9 Future Work

9.1 *In-operando* probe of the rubrene/IL interface by synchrotron X-ray

As discussed in Chapter 8, the IL/rubrene interface plays a significant role in charge transport in rubrene EGTs. Possible limiting factors exist on both the rubrene side and the IL side of the interface. On the rubrene side, the possibility of short-range charge ordering at fractional filling deserves exploring; on the IL side, the Coulomb corrugation potential experienced by holes could effectively serve as interfacial electrostatic disorder. To get a better understanding of what occurs at the IL/rubrene interface during electrolyte gating, other probes beyond electronic transport, such as *in-operando* X-ray scattering, are urgently needed.

X-ray scattering has been developed as a powerful tool to study charge ordering in many correlated materials.[252–255] Recently, it has also been used to confirm the existence of charge ordering in several BEDT-TTF-based organic conductors.[242,248,249] If there is charge ordering, in addition to Bragg peaks of the lattice, extra charge ordering peaks with certain scattering vectors would appear in diffuse scattering measurements. The shapes of peaks depend on the nature of charge ordering. In a typical 2D reciprocal space map, long-range charge ordering would give small, bright spots, while short-range charge ordering would lead to the appearance of diffuse rods with lower intensities. Therefore, in rubrene EGTs, if short-range charge ordering really exists, charge ordering signals should be detected by X-ray when the applied V_G becomes large enough.

Unlike those organic conductors in which charge ordering is developed over the bulk, in rubrene EGTs, charge accumulation and transport are limited at the rubrene/IL interface. Consequently, grazing incidence X-ray scattering is required to probe 2D phenomena at

the interface. In addition, due to its 2D nature, the interfacial charge ordering may only give very weak scattering signals. As a result, synchrotron X-ray sources with large intensities are needed. Although progress has been made in studying the microstructure of organic semiconductors using grazing incidence X-ray, it is still challenging to perform synchrotron X-ray scattering experiments on electrolyte-gated rubrene crystals. The main difficulty comes from the overlying electrolyte layer, which may cause problems such as extra scattering and absorption of X-ray. Recently, synchrotron X-ray scattering and absorption spectroscopy experiments have been made in EGTs based on several inorganic materials, leading to findings including gate-induced lattice expansion and oxygen vacancy formation.[234,256–261] Similar experiments on organic single crystal EGTs, however, have not been done yet.

To perform *in-operando* X-ray scattering experiments on rubrene EGTs, the device structure needs to be modified. The PDMS-based device geometry is obviously not suitable for scattering, since the interface we are interested in is the bottom surface of the crystal, which cannot be probed by grazing incidence X-ray. An alternative side-gated geometry is therefore proposed (**Figures 9.1a and 9.1b**). To make sure that most of the applied V_G drops at the rubrene/IL interface, the gate area is designed to be much larger than the size of a rubrene crystal. Such a device architecture allows the observation of conduction peaks in transfer curves of rubrene EGTs (**Figure 9.1c**). It is worth noting that the variation of peak positions in different devices is very small, demonstrating great reproducibility of the side-gated rubrene EGTs.

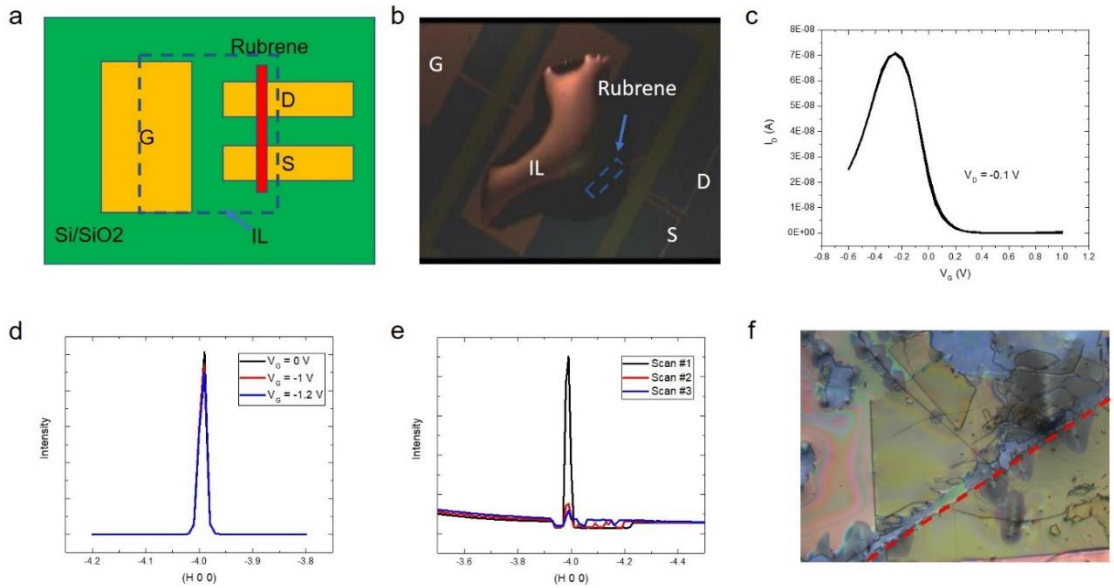

Figure 9.1 (a) Schematic of side-gated rubrene EGTs. (b) Optical image of a side-gated rubrene EGT with IL covering both the gate and the channel. (c) Typical transfer curve of a side-gated rubrene EGT. (d) Grazing incidence synchrotron X-ray scattering of an IL-gated rubrene crystal at different V_G. (e) Beam damage test of the same crystal shown in (d). (f) Optical image of the rubrene crystal after beam damage test. The red dashed line depicts the etched region.

We have carried out preliminary synchrotron X-ray scattering experiments on rubrene EGTs in the Advanced Photon Source at Argonne National Laboratory. The X-ray used here is a grazing incidence X-ray beam with an energy of 23 keV and a grazing angle of 0.4°. The sample is mounted to the sample stage using Ag paint and the conducting wires are soldered to the Au electrodes on the sample by indium in order to apply V_G. Thin rubrene crystals with relatively large dimensions (L > 1000 μm, W > 100 μm) are chosen, because the diameter of the X-ray beam is ~ 100 μm. After applying the IL droplet, the channel and the gate are covered by a piece of Kapton film to make the IL layer thin and flat. Under these conditions, the Bragg peaks of electrolyte-gated rubrene crystals have been observed. **Figure 9.1d** shows the room-temperature in-plane (H00) scans around the (400) diffraction peak of a rubrene single crystal at different gate voltages. No gating-

induced structural change is observed at V_G up to -1.2 V, confirming the electrostatic nature of charge accumulation in rubrene EGTs. Note that the conductance peak usually appears at V_G = 0 to -0.5 V, so the possibility of electrochemistry-induced conductance peak is excluded.

The influence of beam damage, however, still exists and needs to be overcome. **Figure 9.1e** exhibits the beam damage test of the same sample shown in **Figure 9.1d**. In the beam damage test, the crystal is scanned continuously by X-ray, and each scan takes about 20 min. Obviously, the intensity of the (400) peak decreases dramatically upon long-time X-ray exposure, and the (400) peak becomes almost negligible during the third scan. The beam damage is further evidenced by the optical image of the rubrene crystal after X-ray scattering experiments, in which some regions of the crystal are found to be etched by X-ray (**Figure 9.1f**).

Several approaches might be helpful to reduce the influence of beam damage. The first one is to perform X-ray scattering experiments at low temperatures, which has been found to mitigate beam damage in EGTs based on inorganic materials such as LSCO.[234] Taking measurements at different positions on the same crystal could also further lower the influence of beam damage, which is not difficult to achieve considering the length of the crystal (> 1000 μm). Another possible solution is to use a fluorine-free ionic liquid, since people believe that the major source of beam damage is the absorption of X-ray by fluorine. Despite the technical difficulties, the realization of stable, reproducible synchrotron X-ray scattering experiments on EGTs based on organic single crystals would be a remarkable achievement.

9.2 Reducing interfacial electronic disorder by inserting a spacer layer

In EGTs, the existence of ions near the semiconductor channel inevitably leads to interfacial electronic disorder, especially when the charge density is very high. The Coulomb corrugation potential experienced by charge carriers near the semiconductor/electrolyte surface could be a limiting factor for charge transport. The influence of such interfacial electronic disorder is particularly significant in organic semiconductors whose dielectric constants are relatively small, due to the weakly screened electrical field. In the case of rubrene EGTs, the observation of negative transconductance and free carrier saturation further suggest that the ion-charge interaction should be mitigated to improve charge transport in rubrene.[144,156,240,241]

One way to reduce the interfacial electronic disorder is to separate the ions and the charge farther, as electric field inversely scales with distance. This can be achieved by inserting an ultrathin (several nm) insulating layer between the semiconductor and the electrolyte. The spacer layer needs to be chemically inert to avoid possible electrochemical reactions during electrolyte gating; its dielectric constant also needs to be relatively small, since the insulating material with a large dielectric constant would be an extra source of electronic disorder due to the formation of interfacial Froehlich polaron.[93] The capacitance would of course decrease after inserting the spacer layer because of the increased thickness of electrical double layer. Consequently, there would be a trade-off between achieving high charge densities (thin spacers) and high mobilities (thick spacers).

The possibility of using parylene as the spacer has been examined. Parylene is a chemically stable insulator with a low dielectric constant (< 3). It can be deposited at room temperature by CVD to form a pinhole-free, conformal coating, and therefore was used as

the dielectric to fabricate the first rubrene single crystal transistor.[84] It has recently been found that controllable deposition of nm-thick parylene films can be achieved by an effusion-limited CVD process.[262] The ultrathin parylene films can be observed under an optical microscope, which exhibit a blue-green color (**Figure 9.2a**). The thicknesses of ultrathin parylene films, which depend on the amount of source materials, can be optically determined by measuring the reflectance as a function of wavelength (Filmetrics F50-EXR), as shown in **Figure 9.2b**.

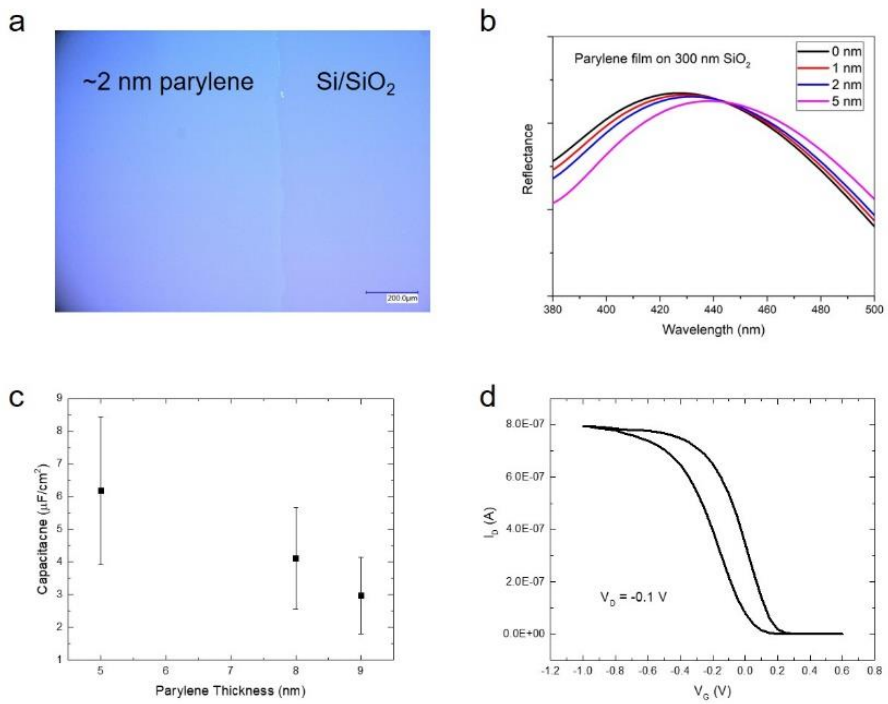

Figure 9.2 (a) Optical image of an ultrathin parylene film on Si/SiO_2 substrate. (b) Theoretical reflectance versus wavelength for parylene films with different thicknesses. (c) Capacitance of rubrene EGTs with various thicknesses of parylene spacer layers. (d) Saturation-like transfer curve of a rubrene EGT with parylene spacer.

Based on the device geometry shown in **Figure 9.1a**, rubrene EGTs with parylene spacers have been fabricated and tested. After laminating thin rubrene crystals onto the Si/SiO_2 wafer with prepatterned electrodes, the devices are loaded into the CVD chamber to deposit the parylene spacers, and IL droplets are applied onto the parylene-coated

rubrene crystals. With the increase of parylene thickness, the decrease of capacitance is observed as expected (**Figure 9.2c**). In transfer curves of some devices with parylene spacers, the conductance peaks are no longer observed; instead, saturation-like drain current appears at high V_G (**Figure 9.2d**). The maximum V_G window, however, is not improved, probably due to the relatively large roughness of parylene (~3 nm), which may allow the ions to diffuse through the spacer layer and to touch the rubrene crystal. Therefore, the maximum conductivity of rubrene EGTs is not improved owing to the decreased charge density.

Recently, using hexagonal boron nitride (hBN) as spacer layers in EGTs based on 2D materials has been reported, and improved mobility and device stability have been observed.[263–266] The atomically flat, dangling bond-free nature of hBN makes it a perfect candidate for spacer layer in EGTs. Transferring hBN thin flakes on rubrene crystals, however, is still very challenging. Mechanically exfoliated hBN thin flakes are small (~10 μm), which is not enough to fully cover the rubrene channel. On the other hand, CVD-grown multilayer hBN can be large enough, but the transfer process involves the use of solvents, which is detrimental to rubrene crystals. Nevertheless, applying van der Waals layered insulators in rubrene EGTs is still promising, if solvent-free transfer of large area ultrathin films could be realized.

Bibliography

(1) Chiang, C. K.; Fincher, C. R.; Park, Y. W.; Heeger, A. J.; Shirakawa, H.; Louis, E. J.; Gau, S. C.; MacDiarmid, A. G. Electrical Conductivity in Doped Polyacetylene. *Phys. Rev. Lett.* **1977**, *39* (17), 1098–1101.

(2) Forrest, S. R. The Path to Ubiquitous and Low-Cost Organic Electronic Appliances on Plastic. *Nature* **2004**, *428* (6986), 911–918.

(3) Dimitrakopoulos, C. D.; Malenfant, P. R. L. Organic Thin Film Transistors for Large Area Electronics. *Adv. Mater.* **2002**, *14* (2), 99–117.

(4) Sekitani, T.; Someya, T. Stretchable, Large-Area Organic Electronics. *Adv. Mater.* **2010**, *22* (20), 2228–2246.

(5) Podzorov, V. Organic Single Crystals: Addressing the Fundamentals of Organic Electronics. *MRS Bull.* **2013**, *38* (1), 15–24.

(6) de Boer, R. W. I.; Gershenson, M. E.; Morpurgo, A. F.; Podzorov, V. Organic Single-Crystal Field-Effect Transistors. *Phys. Status Solidi* **2004**, *201* (6), 1302–1331.

(7) Gershenson, M. E.; Podzorov, V.; Morpurgo, A. F. Colloquium: Electronic Transport in Single-Crystal Organic Transistors. *Rev. Mod. Phys.* **2006**, *78* (3), 973–989.

(8) Podzorov, V.; Menard, E.; Borissov, A.; Kiryukhin, V.; Rogers, J. A.; Gershenson, M. E. Intrinsic Charge Transport on the Surface of Organic Semiconductors. *Phys. Rev. Lett.* **2004**, *93* (8), 86602.

(9) Podzorov, V.; Menard, E.; Rogers, J. A.; Gershenson, M. E. Hall Effect in the Accumulation Layers on the Surface of Organic Semiconductors. *Phys. Rev. Lett.* **2005**, *95* (22), 226601.

(10) Coropceanu, V.; Cornil, J.; da Silva Filho, D. A.; Olivier, Y.; Silbey, R.; Brédas, J.-L. Charge Transport in Organic Semiconductors. *Chem. Rev.* **2007**, *107* (4), 926–952.

(11) Stassen, A. F.; De Boer, R. W. I.; Losad, N. N.; Morpurgo, A. F. Influence of the Gate Dielectric on the Mobility of Rubrene Single-Crystal Field-Effect Transistors. *Appl. Phys. Lett.* **2004**, *85* (17), 3899–3901.

(12) https://phys.org/news/2014-08-benzene.html.

(13) Brédas, J. L.; Calbert, J. P.; da Silva Filho, D. A.; Cornil, J. Organic Semiconductors: A Theoretical Characterization of the Basic Parameters Governing Charge Transport. *Proc. Natl. Acad. Sci. U. S. A.* **2002**, *99* (9), 5804–5809.

(14) da Silva Filho, D. A.; Kim, E.-G.; Bredas, J.-L. Transport Properties in the Rubrene Crystal: Electronic Coupling and Vibrational Reorganization Energy. *Adv. Mater.* **2005**, *17* (8), 1072–1076.

(15) Bao, Z.; Locklin, J. *Organic Field-Effect Transistors*; CRC Press: Boca Raton, FL, 2007.

(16) Holstein, T. Studies of Polaron Motion Part I. The Molecular-Crystal Model. *Ann. Phys. (N. Y).* **1959**, *8*, 325–342.

(17) Holstein, T. Studies of Polaron Motion: Part II The “Small” Polaron. *Ann. Phys. (N. Y).* **1959**, *8*, 343–389.

(18) Friedman, L.; Holstein, T. Studies of Polaron Motion. *Ann. Phys. (N. Y).* **1963**, *21* (3), 494–549.

(19) Emin, D. Transport Properties of Small Polarons. *J. Solid State Chem.* **1975**, *12* (3–4), 246–252.
(20) Ortmann, F.; Roche, S. Polaron Transport in Organic Crystals: Temperature Tuning of Disorder Effects. *Phys. Rev. B* **2011**, *84* (18), 180302.
(21) Marcus, R. A. Chemical and Electrochemical Electron-Transfer Theory. *Annu. Rev. Phys. Chem.* **1964**, *15* (1), 155.
(22) Marcus, R. A. Electron Transfer Reactions in Chemistry: Theory and Experiment (Nobel Lecture). *Rev. Mod. Phys.* **1993**, *32* (8), 1111–1121.
(23) Miller, A.; Abrahams, E. Impurity Conduction at Low Concentrations. *Phys. Rev.* **1960**, *120* (3), 745–755.
(24) Mott, N. F.; Davis, E. A. *Electronic Processes in Non-Crystalline Materials*; OUP Oxford, 2012.
(25) Shklovskii, B. I.; Efros, A. L. *Electronic Properties of Doped Semiconductors*; Springer Science & Business Media, 2013; Vol. 45.
(26) Silbey, R.; Munn, R. W. General Theory of Electronic Transport in Molecular Crystals. I. Local Linear Electron–phonon Coupling. *J. Chem. Phys.* **1980**, *72* (4), 2763.
(27) Karl, N. Charge Carrier Transport in Organic Semiconductors. *Synth. Met.* **2003**, *133–134*, 649–657.
(28) Xie, H.; Alves, H.; Morpurgo, A. F. Quantitative Analysis of Density-Dependent Transport in Tetramethyltetraselenafulvalene Single-Crystal Transistors: Intrinsic Properties and Trapping. *Phys. Rev. B* **2009**, *80* (24), 245305.
(29) Liu, C.; Minari, T.; Lu, X.; Kumatani, A.; Takimiya, K.; Tsukagoshi, K. Solution-Processable Organic Single Crystals with Bandlike Transport in Field-Effect Transistors. *Adv. Mater.* **2011**, *23* (4), 523–526.
(30) Nakayama, K.; Hirose, Y.; Soeda, J.; Yoshizumi, M.; Uemura, T.; Uno, M.; Li, W.; Kang, M. J.; Yamagishi, M.; Okada, Y.; Miyazaki, E.; Nakazawa, Y.; Nakao, A.; Takimiya, K.; Takeya, J. Patternable Solution-Crystallized Organic Transistors with High Charge Carrier Mobility. *Adv. Mater.* **2011**, *23* (14), 1626–1629.
(31) Kubo, T.; Häusermann, R.; Tsurumi, J.; Soeda, J.; Okada, Y.; Yamashita, Y.; Akamatsu, N.; Shishido, A.; Mitsui, C.; Okamoto, T.; Yanagisawa, S.; Matsui, H.; Takeya, J. Suppressing Molecular Vibrations in Organic Semiconductors by Inducing Strain. *Nat. Commun.* **2016**, *7*, 11156.
(32) Minder, N. A.; Ono, S.; Chen, Z.; Facchetti, A.; Morpurgo, A. F. Band-like Electron Transport in Organic Transistors and Implication of the Molecular Structure for Performance Optimization. *Adv. Mater.* **2012**, *24* (4), 503–508.
(33) Minder, N. A.; Lu, S.; Fratini, S.; Ciuchi, S.; Facchetti, A.; Morpurgo, A. F. Tailoring the Molecular Structure to Suppress Extrinsic Disorder in Organic Transistors. *Adv. Mater.* **2014**, *26* (8), 1254–1260.
(34) Krupskaya, Y.; Gibertini, M.; Marzari, N.; Morpurgo, A. F. Band-Like Electron Transport with Record-High Mobility in the TCNQ Family. *Adv. Mater.* **2015**, *27* (15), 2453–2458.
(35) He, T.; Wu, Y.; D'Avino, G.; Schmidt, E.; Stolte, M.; Cornil, J.; Beljonne, D.; Ruden, P. P.; Würthner, F.; Frisbie, C. D. Crystal Step Edges Can Trap Electrons on the Surfaces of N-Type Organic Semiconductors. *Nat. Commun.* **2018**, *9* (1), 2141.
(36) Xie, W.; McGarry, K. A.; Liu, F.; Wu, Y.; Ruden, P. P.; Douglas, C. J.; Frisbie, C.

D. High-Mobility Transistors Based on Single Crystals of Isotopically Substituted Rubrene-d_{28}. *J. Phys. Chem. C* **2013**, *117* (22), 11522–11529.
(37) Ren, X.; Bruzek, M. J.; Hanifi, D. A.; Schulzetenberg, A.; Wu, Y.; Kim, C.-H.; Zhang, Z.; Johns, J. E.; Salleo, A.; Fratini, S.; Troisi, A.; Douglas, C. J.; Frisbie, C. D. Negative Isotope Effect on Field-Effect Hole Transport in Fully Substituted ^{13}C-Rubrene. *Adv. Electron. Mater.* **2017**, *3* (4), 1700018.
(38) Eggeman, A. S.; Illig, S.; Troisi, A.; Sirringhaus, H.; Midgley, P. A. Measurement of Molecular Motion in Organic Semiconductors by Thermal Diffuse Electron Scattering. *Nat. Mater.* **2013**, *12* (11), 1045–1049.
(39) Troisi, A.; Orlandi, G.; Anthony, J. E. Electronic Interactions and Thermal Disorder in Molecular Crystals Containing Cofacial Pentacene Units. *Chem. Mater.* **2005**, *17* (20), 5024–5031.
(40) Troisi, A.; Orlandi, G. Charge-Transport Regime of Crystalline Organic Semiconductors: Diffusion Limited by Thermal Off-Diagonal Electronic Disorder. *Phys. Rev. Lett.* **2006**, *96* (8), 86601.
(41) Troisi, A. Prediction of the Absolute Charge Mobility of Molecular Semiconductors: The Case of Rubrene. *Adv. Mater.* **2007**, *19* (15), 2000–2004.
(42) Fratini, S.; Ciuchi, S. Bandlike Motion and Mobility Saturation in Organic Molecular Semiconductors. *Phys. Rev. Lett.* **2009**, *103* (26), 266601.
(43) Troisi, A. Dynamic Disorder in Molecular Semiconductors: Charge Transport in Two Dimensions. *J. Chem. Phys.* **2011**, *134* (3), 1–10.
(44) Fratini, S.; Mayou, D.; Ciuchi, S. The Transient Localization Scenario for Charge Transport in Crystalline Organic Materials. *Adv. Funct. Mater.* **2016**, *26* (14), 2292–2315.
(45) Klauk, H. Organic Thin-Film Transistors. *Chem. Soc. Rev.* **2010**, *39* (7), 2643.
(46) Takenobu, T.; Takahashi, T.; Takeya, J.; Iwasa, Y. Effect of Metal Electrodes on Rubrene Single-Crystal Transistors. *Appl. Phys. Lett.* **2007**, *90* (1), 2005–2008.
(47) Zaumseil, J.; Sirringhaus, H. Electron and Ambipolar Transport in Organic Field-Effect Transistors. *Chem. Rev.* **2007**, *107* (4), 1296–1323.
(48) Newman, C. R.; Frisbie, C. D.; Da Silva Filho, D. A.; Brédas, J. L.; Ewbank, P. C.; Mann, K. R. Introduction to Organic Thin Film Transistors and Design of N-Channel Organic Semiconductors. *Chem. Mater.* **2004**, *16* (23), 4436–4451.
(49) Choi, H. H.; Cho, K.; Frisbie, C. D.; Sirringhaus, H.; Podzorov, V. Critical Assessment of Charge Mobility Extraction in FETs. *Nat. Mater.* **2017**, *17* (1), 2–7.
(50) Uemura, T.; Rolin, C.; Ke, T. H.; Fesenko, P.; Genoe, J.; Heremans, P.; Takeya, J. On the Extraction of Charge Carrier Mobility in High-Mobility Organic Transistors. *Adv. Mater.* **2016**, *28* (1), 151–155.
(51) Bittle, E. G.; Basham, J. I.; Jackson, T. N.; Jurchescu, O. D.; Gundlach, D. J. Mobility Overestimation due to Gated Contacts in Organic Field-Effect Transistors. *Nat. Commun.* **2016**, *7*, 10908.
(52) McCulloch, I.; Salleo, A.; Chabinyc, M. Avoid the Kinks When Measuring Mobility. *Science* **2016**, *352* (6293), 1521–1522.
(53) Phan, H.; Ford, M. J.; Lill, A. T.; Wang, M.; Bazan, G. C.; Nguyen, T.-Q. Electrical Double-Slope Nonideality in Organic Field-Effect Transistors. *Adv. Funct. Mater.* **2018**, *28* (17), 1707221.
(54) Xu, Y.; Sun, H.; Liu, A.; Zhu, H.; Li, B.; Minari, T.; Balestra, F.; Ghibaudo, G.;

Noh, Y.-Y. Essential Effects on the Mobility Extraction Reliability for Organic Transistors. *Adv. Funct. Mater.* **2018**, *28* (42), 1803907.
(55) Braga, D.; Horowitz, G. High-Performance Organic Field-Effect Transistors. *Adv. Mater.* **2009**, *21* (14–15), 1473–1486.
(56) Pesavento, P. V.; Chesterfield, R. J.; Newman, C. R.; Frisble, C. D. Gated Four-Probe Measurements on Pentacene Thin-Film Transistors: Contact Resistance as a Function of Gate Voltage and Temperature. *J. Appl. Phys.* **2004**, *96* (12), 7312–7324.
(57) Rolin, C.; Kang, E.; Lee, J.-H.; Borghs, G.; Heremans, P.; Genoe, J. Charge Carrier Mobility in Thin Films of Organic Semiconductors by the Gated van der Pauw Method. *Nat. Commun.* **2017**, *8*, 14975.
(58) Chen, Y.; Yi, H. T.; Podzorov, V. High-Resolution AC Measurements of the Hall Effect in Organic Field-Effect Transistors. *Phys. Rev. Appl.* **2016**, *5* (3), 34008.
(59) Takeya, J.; Tsukagoshi, K.; Aoyagi, Y.; Takenobu, T.; Iwasa, Y. Hall Effect of Quasi-Hole Gas in Organic Single-Crystal Transistors. *Japanese J. Appl. Physics, Part 2 Lett.* **2005**, *44* (46–49), 1393–1396.
(60) Mitsui, C.; Okamoto, T.; Yamagishi, M.; Tsurumi, J.; Yoshimoto, K.; Nakahara, K.; Soeda, J.; Hirose, Y.; Sato, H.; Yamano, A.; et al. High-Performance Solution-Processable N-Shaped Organic Semiconducting Materials with Stabilized Crystal Phase. *Adv. Mater.* **2014**, *26* (26), 4546–4551.
(61) Yamashita, Y.; Hinkel, F.; Marszalek, T.; Zajaczkowski, W.; Pisula, W.; Baumgarten, M.; Matsui, H.; Müllen, K.; Takeya, J. Mobility Exceeding 10 cm^2/Vs in Donor-Acceptor Polymer Transistors with Band-like Charge Transport. *Chem. Mater.* **2016**, *28*, 420–424.
(62) Chang, J. F.; Sakanoue, T.; Olivier, Y.; Uemura, T.; Dufourg-Madec, M. B.; Yeates, S. G.; Cornil, J.; Takeya, J.; Troisi, A.; Sirringhaus, H. Hall-Effect Measurements Probing the Degree of Charge-Carrier Delocalization in Solution-Processed Crystalline Molecular Semiconductors. *Phys. Rev. Lett.* **2011**, *107* (6), 1–4.
(63) Jiang, H.; Kloc, C. Single-Crystal Growth of Organic Semiconductors. *MRS Bull.* **2013**, *38* (1), 28–33.
(64) Pfann, W. G. Principles of Zone-Melting. *JOM* **1952**, *4* (7), 747–753.
(65) Bridgman, P. W. Certain Physical Properties of Single Crystals of Tungsten, Antimony, Bismuth, Tellurium, Cadmium, Zinc, and Tin. In *Proceedings of the American Academy of Arts and Sciences*; JSTOR, 1925; Vol. 60, pp 305–383.
(66) Mueller, G. The Czochralski Method-where We Are 90 Years after Jan Czochralski's Invention. *Cryst. Res. Technol. J. Exp. Ind. Crystallogr.* **2007**, *42* (12), 1150–1161.
(67) Warta, W.; Stehle, R.; Karl, N. Ultrapure, High Mobility Organic Photoconductors. *Appl. Phys. A* **1985**, *36* (3), 163–170.
(68) Hong, I. H.; Jie Tan, K.; Toh, M.; Jiang, H.; Zhang, K.; Kloc, C. Impurities in Zone-Refining Anthracene Crystals. *J. Cryst. Growth* **2013**, *363*, 61–68.
(69) https://en.wikipedia.org/wiki/Zone_melting.
(70) https://en.wikipedia.org/wiki/Bridgman%E2%80%93Stockbarger_technique.
(71) https://en.wikipedia.org/wiki/Czochralski_process.
(72) liu, Y.; Han, Y.; Zhao, X.; Tong, Y.; Tang, Q.; Liu, Y. Single-Crystal Tetrathiafulvalene Microwire Arrays Formed by Drop-Casting Method in the Saturated Solvent Atmosphere. *Synth. Met.* **2014**, *198*, 248–254.

(73) Jang, J.; Nam, S.; Im, K.; Hur, J.; Cha, S. N.; Kim, J.; Son, H. Bin; Suh, H.; Loth, M. A.; Anthony, J. E.; Park, J.; Park, E. N.; Kim, J. M.; Kim, K. Highly Crystalline Soluble Acene Crystal Arrays for Organic Transistors: Mechanism of Crystal Growth During Dip-Coating. *Adv. Funct. Mater.* **2012**, *22* (5), 1005–1014.

(74) Minemawari, H.; Yamada, T.; Matsui, H.; Tsutsumi, J.; Haas, S.; Chiba, R.; Kumai, R.; Hasegawa, T. Inkjet Printing of Single-Crystal Films. *Nature* **2011**, *475* (7356), 364–367.

(75) Yang, Y.; Liu, C.; Gao, S.; Li, Y.; Wang, X.; Wang, Y.; Minari, T.; Xu, Y.; Wang, P.; Zhao, Y.; Tsukagushi, K.; Shi, Y. Large [6,6]-Phenyl C_{61} Butyric Acid Methyl (PCBM) Hexagonal Crystals Grown by Solvent-Vapor Annealing. *Mater. Chem. Phys.* **2014**, *145* (3), 327–333.

(76) Yamamura, A.; Watanabe, S.; Uno, M.; Mitani, M.; Mitsui, C.; Tsurumi, J.; Isahaya, N.; Kanaoka, Y.; Okamoto, T.; Takeya, J. Wafer-Scale, Layer-Controlled Organic Single Crystals for High-Speed Circuit Operation. *Sci. Adv.* **2018**, *4* (2), eaao5758.

(77) Giri, G.; Verploegen, E.; Mannsfeld, S. C. B.; Atahan-Evrenk, S.; Kim, D. H.; Lee, S. Y.; Becerril, H. A.; Aspuru-Guzik, A.; Toney, M. F.; Bao, Z. Tuning Charge Transport in Solution-Sheared Organic Semiconductors Using Lattice Strain. *Nature* **2011**, *480* (7378), 504–508.

(78) Kloc, C.; Simpkins, P. G.; Siegrist, T.; Laudise, R. A. Physical Vapor Growth of Centimeter-Sized Crystals of α-Hexathiophene. *J. Cryst. Growth* **1997**, *182* (3–4), 416–427.

(79) Laudise, R. A.; Kloc, C.; Simpkins, P. G.; Siegrist, T. Physical Vapor Growth of Organic Semiconductors. *J. Cryst. Growth* **1998**, *187* (3–4), 449–454.

(80) Lee, C.-H.; Schiros, T.; Santos, E. J. G.; Kim, B.; Yager, K. G.; Kang, S. J.; Lee, S.; Yu, J.; Watanabe, K.; Taniguchi, T.; Hone, J.; Kaxiras, E.; Nuckolls, C.; Kim, P. Epitaxial Growth of Molecular Crystals on van Der Waals Substrates for High-Performance Organic Electronics. *Adv. Mater.* **2014**, *26* (18), 2812–2817.

(81) Wilkinson, F. S.; Norwood, R. F.; McLellan, J. M.; Lawson, L. R.; Patrick, D. L. Engineered Growth of Organic Crystalline Films Using Liquid Crystal Solvents. *J. Am. Chem. Soc.* **2006**, *128* (51), 16468–16469.

(82) Niemax, J.; Tripathi, A. K.; Pflaum, J. Comparison of the Electronic Properties of Sublimation- and Vapor-Bridgman-Grown Crystals of Tetracene. *Appl. Phys. Lett.* **2005**, *86* (12), 122105.

(83) Reese, C.; Bao, Z. Organic Single-Crystal Field-Effect Transistors. *Mater. Today* **2007**, *10* (3), 20–27.

(84) Podzorov, V.; Pudalov, V. M.; Gershenson, M. E. Field-Effect Transistors on Rubrene Single Crystals with Parylene Gate Insulator. *Appl. Phys. Lett.* **2003**, *82* (11), 1739–1741.

(85) Yi, H. T.; Gartstein, Y. N.; Podzorov, V. Charge Carrier Coherence and Hall Effect in Organic Semiconductors. *Sci. Rep.* **2016**, *6* (8), 23650.

(86) Yi, H. T.; Chen, Y.; Czelen, K.; Podzorov, V. Vacuum Lamination Approach to Fabrication of High-Performance Single-Crystal Organic Field-Effect Transistors. *Adv. Mater.* **2011**, *23* (48), 5807–5811.

(87) Takeya, J.; Goldmann, C.; Haas, S.; Pernstich, K. P.; Ketterer, B.; Batlogg, B. Field-Induced Charge Transport at the Surface of Pentacene Single Crystals: A Method to Study Charge Dynamics of Two-Dimensional Electron Systems in Organic Crystals.

J. Appl. Phys. **2003**, *94* (9), 5800.
(88) Menard, E.; Podzorov, V.; Hur, S.-H.; Gaur, A.; Gershenson, M. E.; Rogers, J. A. High-Performance N- and P-Type Single-Crystal Organic Transistors with Free-Space Gate Dielectrics. *Adv. Mater.* **2004**, *16* (23–24), 2097–2101.
(89) de Boer, R. W. I.; Klapwijk, T. M.; Morpurgo, A. F. Field-Effect Transistors on Tetracene Single Crystals. *Appl. Phys. Lett.* **2003**, *83* (21), 4345–4347.
(90) Sundar, V. C.; Zaumseil, J.; Podzorov, V.; Menard, E.; Willett, R. L.; Someya, T.; Gershenson, M. E.; Rogers, J. A. Elastomeric Transistor Stamps: Reversible Probing of Charge Transport in Organic Crystals. *Science* **2004**, *303* (5664), 1644–1646.
(91) Reese, C.; Bao, Z. High-Resolution Measurement of the Anisotropy of Charge Transport in Single Crystals. *Adv. Mater.* **2007**, *19* (24), 4535–4538.
(92) Horowitz, G. Organic Field-Effect Transistors. *Adv. Mater.* **1998**, *10* (5), 365–377.
(93) Hulea, I. N.; Fratini, S.; Xie, H.; Mulder, C. L.; Iossad, N. N.; Rastelli, G.; Ciuchi, S.; Morpurgo, A. F. Tunable Fröhlich Polarons in Organic Single-Crystal Transistors. *Nat. Mater.* **2006**, *5* (12), 982–986.
(94) Yoon, M.-H.; Yan, H.; Facchetti, A.; Marks, T. J. Low-Voltage Organic Field-Effect Transistors and Inverters Enabled by Ultrathin Cross-Linked Polymers as Gate Dielectrics. *J. Am. Chem. Soc.* **2005**, *127* (29), 10388–10395.
(95) Halik, M.; Klauk, H.; Zschieschang, U.; Schmid, G.; Dehm, C.; Schütz, M.; Maisch, S.; Effenberger, F.; Brunnbauer, M.; Stellacci, F. Low-Voltage Organic Transistors with an Amorphous Molecular Gate Dielectric. *Nature* **2004**, *431* (7011), 963–966.
(96) Ahn, C. H.; Gariglio, S.; Paruch, P.; Tybell, T.; Antognazza, L.; Triscone, J.-M. Electrostatic Modulation of Superconductivity in Ultrathin $GdBa_2Cu_3O_{7-X}$ Films. *Science* **1999**, *284* (5417), 1152–1155.
(97) Xie, W.; Frisbie, C. D. Electrolyte Gated Single-Crystal Organic Transistors to Examine Transport in the High Carrier Density Regime. *MRS Bull.* **2013**, *38* (1), 43–50.
(98) Yuan, H.; Shimotani, H.; Tsukazaki, A.; Ohtomo, A.; Kawasaki, M.; Iwasa, Y. High-Density Carrier Accumulation in ZnO Field-Effect Transistors Gated by Electric Double Layers of Ionic Liquids. *Adv. Funct. Mater.* **2009**, *19* (7), 1046–1053.
(99) Khodagholy, D.; Rivnay, J.; Sessolo, M.; Gurfinkel, M.; Leleux, P.; Jimison, L. H.; Stavrinidou, E.; Herve, T.; Sanaur, S.; Owens, R. M.; et al. High Transconductance Organic Electrochemical Transistors. *Nat. Commun.* **2013**, *4* (1), 2133.
(100) Thomas, E. M.; Brady, M. A.; Nakayama, H.; Popere, B. C.; Segalman, R. A.; Chabinyc, M. L. X-Ray Scattering Reveals Ion-Induced Microstructural Changes During Electrochemical Gating of Poly(3-Hexylthiophene). *Adv. Funct. Mater.* **2018**, *28* (44), 1803687.
(101) Jeong, J.; Aetukuri, N.; Graf, T.; Schladt, T. D.; Samant, M. G.; Parkin, S. S. P. Suppression of Metal-Insulator Transition in VO_2 by Electric Field-Induced Oxygen Vacancy Formation. *Science* **2013**, *339* (6126), 1402–1405.
(102) Shi, W.; Ye, J.; Zhang, Y.; Suzuki, R.; Yoshida, M.; Miyazaki, J.; Inoue, N.; Saito, Y.; Iwasa, Y. Superconductivity Series in Transition Metal Dichalcogenides by Ionic Gating. *Sci. Rep.* **2015**, *5* (1), 12534.
(103) White, H. S.; Kittlesen, G. P.; Wrighton, M. S. Chemical Derivatization of an Array of Three Gold Microelectrodes with Polypyrrole: Fabrication of a Molecule-Based

Transistor. *J. Am. Chem. Soc.* **1984**, *106* (18), 5375–5377.
(104) Chao, S.; Wrighton, M. S. Solid-State Microelectrochemistry: Electrical Characteristics of a Solid-State Microelectrochemical Transistor Based on poly(3-Methylthiophene). *J. Am. Chem. Soc.* **1987**, *109* (7), 2197–2199.
(105) Chao, S.; Wrighton, M. S. Characterization of a Solid-State Polyaniline-Based Transistor: Water Vapor Dependent Characteristics of a Device Employing a Poly(vinyl Alcohol)/phosphoric Acid Solid-State Electrolyte. *J. Am. Chem. Soc.* **1987**, *109* (22), 6627–6631.
(106) Ofer, D.; Wrighton, M. S. Potential Dependence of the Conductivity of poly(3-Methylthiophene) in Liquid Sulfur Dioxide/electrolyte: A Finite Potential Window of High Conductivity. *J. Am. Chem. Soc.* **1988**, *110* (13), 4467–4468.
(107) Ofer, D.; Crooks, R. M.; Wrighton, M. S. Potential Dependence of the Conductivity of Highly Oxidized Polythiophenes, Polypyrroles, and Polyaniline: Finite Windows of High Conductivity. *J. Am. Chem. Soc.* **1990**, *112* (22), 7869–7879.
(108) Ofer, D.; Park, L. Y.; Schrock, R. R.; Wrighton, M. S. Potential Dependence of the Conductivity of Polyacetylene: Finite Potential Windows of High Conductivity. *Chem. Mater.* **1991**, *3* (4), 573–575.
(109) Rosenblatt, S.; Yaish, Y.; Park, J.; Gore, J.; Sazonova, V.; McEuen, P. L. High Performance Electrolyte Gated Carbon Nanotube Transistors. *Nano Lett.* **2002**, *2* (8), 869–872.
(110) Shimotani, H.; Kanbara, T.; Iwasa, Y.; Tsukagoshi, K.; Aoyagi, Y.; Kataura, H. Gate Capacitance in Electrochemical Transistor of Single-Walled Carbon Nanotube. *Appl. Phys. Lett.* **2006**, *88* (7), 73104.
(111) Back, J. H.; Shim, M. pH-Dependent Electron-Transport Properties of Carbon Nanotubes. *J. Phys. Chem. B* **2006**, *110* (47), 23736–23741.
(112) Buth, F.; Kumar, D.; Stutzmann, M.; Garrido, J. A. Electrolyte-Gated Organic Field-Effect Transistors for Sensing Applications. *Appl. Phys. Lett.* **2011**, *98* (15), 153302.
(113) Fenton, D. E.; Parker, J. M.; Wright, P. V. Complexes of Alkali Metal Ions with Poly(ethylene Oxide). *Polymer* **1973**, *14* (11), 589.
(114) Siddons, G. P.; Merchin, D.; Back, J. H.; Jeong, J. K.; Shim, M. Highly Efficient Gating and Doping of Carbon Nanotubes with Polymer Electrolytes. *Nano Lett.* **2004**, *4* (5), 927–931.
(115) Panzer, M. J.; Frisbie, C. D. High Charge Carrier Densities and Conductance Maxima in Single-Crystal Organic Field-Effect Transistors with a Polymer Electrolyte Gate Dielectric. *Appl. Phys. Lett.* **2006**, *88* (20), 203504.
(116) Panzer, M. J.; Frisbie, C. D. Polymer Electrolyte Gate Dielectric Reveals Finite Windows of High Conductivity in Organic Thin Film Transistors at High Charge Carrier Densities. *J. Am. Chem. Soc.* **2005**, *127* (19), 6960–6961.
(117) Panzer, M. J.; Frisbie, C. D. High Carrier Density and Metallic Conductivity in Poly(3-Hexylthiophene) Achieved by Electrostatic Charge Injection. *Adv. Funct. Mater.* **2006**, *16* (8), 1051–1056.
(118) Ueno, K.; Nakamura, S.; Shimotani, H.; Ohtomo, a; Kimura, N.; Nojima, T.; Aoki, H.; Iwasa, Y.; Kawasaki, M. Electric-Field-Induced Superconductivity in an Insulator. *Nat. Mater.* **2008**, *7* (11), 855–858.
(119) https://opentextbc.ca/chemistry/chapter/11-2-electrolytes/.
(120) Wu, C.-L.; Yuan, H.; Li, Y.; Gong, Y.; Hwang, H. Y.; Cui, Y. Gate-Induced Metal–

Insulator Transition in MoS_2 by Solid Superionic Conductor LaF_3. *Nano Lett.* **2018**, *18* (4), 2387–2392.
(121) Said, E.; Crispin, X.; Herlogsson, L.; Elhag, S.; Robinson, N. D.; Berggren, M. Polymer Field-Effect Transistor Gated via a Poly(styrenesulfonic Acid) Thin Film. *Appl. Phys. Lett.* **2006**, *89* (14), 143507.
(122) Zhao, J.; Wang, M.; Li, H.; Zhang, X.; You, L.; Qiao, S.; Gao, B.; Xie, X.; Jiang, M. Lithium-Ion-Based Solid Electrolyte Tuning of the Carrier Density in Graphene. *Sci. Rep.* **2016**, *6* (1), 34816.
(123) Zhao, J.; Wang, M.; Zhang, X.; Lv, Y.; Wu, T.; Qiao, S.; Song, S.; Gao, B. Application of Sodium-Ion-Based Solid Electrolyte in Electrostatic Tuning of Carrier Density in Graphene. *Sci. Rep.* **2017**, *7* (1), 3168.
(124) Lei, B.; Wang, N. Z.; Shang, C.; Meng, F. B.; Ma, L. K.; Luo, X. G.; Wu, T.; Sun, Z.; Wang, Y.; Jiang, Z.; Mao, B. H.; Liu, Z.; Yu, Y. J.; Zhang, Y. B.; Chen, X. H. Tuning Phase Transitions in FeSe Thin Flakes by Field-Effect Transistor with Solid Ion Conductor as the Gate Dielectric. *Phys. Rev. B* **2017**, *95* (2), 20503.
(125) Fujimoto, T.; Awaga, K. Electric-Double-Layer Field-Effect Transistors with Ionic Liquids. *Phys. Chem. Chem. Phys.* **2013**, *15* (23), 8983–9006.
(126) Lee, K. H.; Kang, M. S.; Zhang, S.; Gu, Y.; Lodge, T. P.; Frisbie, C. D. "Cut and Stick" Rubbery Ion Gels as High Capacitance Gate Dielectrics. *Adv. Mater.* **2012**, *24* (32), 4457–4462.
(127) He, Y.; Boswell, P. G.; Bühlmann, P.; Lodge, T. P. Ion Gels by Self-Assembly of a Triblock Copolymer in an Ionic Liquid *J. Phys. Chem. B* **2007**, *111* (18), 4645–4652.
(128) Cho, J. H.; Lee, J.; Xia, Y.; Kim, B.; He, Y.; Renn, M. J.; Lodge, T. P.; Daniel Frisbie, C. Printable Ion-Gel Gate Dielectrics for Low-Voltage Polymer Thin-Film Transistors on Plastic. *Nat. Mater.* **2008**, *7* (11), 900–906.
(129) Choi, J.-H.; Gu, Y.; Hong, K.; Xie, W.; Frisbie, C. D.; Lodge, T. P. High Capacitance, Photo-Patternable Ion Gel Gate Insulators Compatible with Vapor Deposition of Metal Gate Electrodes. *ACS Appl. Mater. Interfaces* **2014**, *6* (21), 19275–19281.
(130) Tang, B.; Schneiderman, D. K.; Zare Bidoky, F.; Frisbie, C. D.; Lodge, T. P. Printable, Degradable, and Biocompatible Ion Gels from a Renewable ABA Triblock Polyester and a Low Toxicity Ionic Liquid. *ACS Macro Lett.* **2017**, *6* (10), 1083–1088.
(131) Zare Bidoky, F.; Hyun, W. J.; Song, D.; Frisbie, C. D. Printed, 1 V Electrolyte-Gated Transistors Based on Poly(3-Hexylthiophene) Operating at >10 kHz on Plastic. *Appl. Phys. Lett.* **2018**, *113* (5), 53301.
(132) Mahajan, A.; Hyun, W. J.; Walker, S. B.; Rojas, G. A.; Choi, J.-H.; Lewis, J. A.; Francis, L. F.; Frisbie, C. D. A Self-Aligned Strategy for Printed Electronics: Exploiting Capillary Flow on Microstructured Plastic Surfaces. *Adv. Electron. Mater.* **2015**, *1* (9), 1500137.
(133) Zare Bidoky, F.; Frisbie, C. D. Parasitic Capacitance Effect on Dynamic Performance of Aerosol-Jet-Printed Sub 2 V Poly(3-Hexylthiophene) Electrolyte-Gated Transistors. *ACS Appl. Mater. Interfaces* **2016**, *8* (40), 27012–27017.
(134) Saito, Y.; Iwasa, Y. Ambipolar Insulator-to-Metal Transition in Black Phosphorus by Ionic-Liquid Gating. *ACS Nano* **2015**, *9* (3), 3192–3198.
(135) Shiogai, J.; Ito, Y.; Mitsuhashi, T.; Nojima, T.; Tsukazaki, A. Electric-Field-Induced

Superconductivity in Electrochemically Etched Ultrathin FeSe Films on $SrTiO_3$ and MgO. *Nat. Phys.* **2016**, *12* (1), 42–46.
(136) Ponomarev, E.; Pásztor, Á.; Waelchli, A.; Scarfato, A.; Ubrig, N.; Renner, C.; Morpurgo, A. F. Hole Transport in Exfoliated Monolayer MoS_2. *ACS Nano* **2018**, *12* (3), 2669–2676.
(137) Xie, W.; Frisbie, C. D. Organic Electrical Double Layer Transistors Based on Rubrene Single Crystals: Examining Transport at High Surface Charge Densities above 10^{13} cm^{-2}. *J. Phys. Chem. C* **2011**, *115* (29), 14360–14368.
(138) Xia, Y.; Cho, J. H.; Lee, J.; Ruden, P. P.; Frisbie, C. D. Comparison of the Mobility-Carrier Density Relation in Polymer and Single-Crystal Organic Transistors Employing Vacuum and Liquid Gate Dielectrics. *Adv. Mater.* **2009**, *21* (21), 2174–2179.
(139) White, S. P.; Dorfman, K. D.; Frisbie, C. D. Label-Free DNA Sensing Platform with Low-Voltage Electrolyte-Gated Transistors. *Anal. Chem.* **2015**, *87* (3), 1861–1866.
(140) Wang, Y.; Kim, C.-H.; Yoo, Y.; Johns, J. E.; Frisbie, C. D. Field Effect Modulation of Heterogeneous Charge Transfer Kinetics at Back-Gated Two-Dimensional MoS_2 Electrodes. *Nano Lett.* **2017**, *17* (12), 7586–7592.
(141) Wang, S.; Ha, M.; Manno, M.; Frisbie, C. D.; Leighton, C. Hopping Transport and the Hall Effect near the Insulator–metal Transition in Electrochemically Gated Poly(3-Hexylthiophene) Transistors. *Nat. Commun.* **2012**, *3*, 1210.
(142) Liang, Y.; Frisbie, C. D.; Chang, H.-C.; Ruden, P. P. Conducting Channel Formation and Annihilation in Organic Field-Effect Structures. *J. Appl. Phys.* **2009**, *105* (2), 24514.
(143) Ogawa, S.; Naijo, T.; Kimura, Y.; Ishii, H.; Niwano, M. Displacement Current Measurement as a Tool to Characterize Organic Field Effect Transistors. *Synth. Met.* **2005**, *153* (1–3), 253–256.
(144) Xie, W.; Wang, S.; Zhang, X.; Leighton, C.; Frisbie, C. D. High Conductance 2D Transport around the Hall Mobility Peak in Electrolyte-Gated Rubrene Crystals. *Phys. Rev. Lett.* **2014**, *113* (24), 246602.
(145) Ahn, C. H.; Triscone, J.-M.; Mannhart, J. Electric Field Effect in Correlated Oxide Systems. *Nature* **2003**, *424* (6952), 1015–1018.
(146) Shimotani, H.; Asanuma, H.; Tsukazaki, A.; Ohtomo, A.; Kawasaki, M.; Iwasa, Y. Insulator-to-Metal Transition in ZnO by Electric Double Layer Gating. *Appl. Phys. Lett.* **2007**, *91* (8), 82106.
(147) Xiang, P.-H.; Asanuma, S.; Yamada, H.; Inoue, I. H.; Sato, H.; Akoh, H.; Sawa, A.; Ueno, K.; Yuan, H.; Shimotani, H.; Kawasaki, M.; Iwasa, Y. Strain-Mediated Phase Control and Electrolyte-Gating of Electron-Doped Manganites. *Adv. Mater.* **2011**, *23* (48), 5822–5827.
(148) Nakano, M.; Shibuya, K.; Okuyama, D.; Hatano, T.; Ono, S.; Kawasaki, M.; Iwasa, Y.; Tokura, Y. Collective Bulk Carrier Delocalization Driven by Electrostatic Surface Charge Accumulation. *Nature* **2012**, *487* (7408), 459–462.
(149) Hatano, T.; Sheng, Z.; Nakamura, M.; Nakano, M.; Kawasaki, M.; Iwasa, Y.; Tokura, Y. Gate Control of Percolative Conduction in Strongly Correlated Manganite Films. *Adv. Mater.* **2014**, *26* (18), 2874–2877.
(150) Yi, H. T.; Gao, B.; Xie, W.; Cheong, S.-W.; Podzorov, V. Tuning the Metal-Insulator Crossover and Magnetism in $SrRuO_3$ by Ionic Gating. *Sci. Rep.* **2015**, *4*

(1), 6604.
(151) Scherwitzl, R.; Zubko, P.; Lezama, I. G.; Ono, S.; Morpurgo, A. F.; Catalan, G.; Triscone, J.-M. Electric-Field Control of the Metal-Insulator Transition in Ultrathin $NdNiO_3$ Films. *Adv. Mater.* **2010**, *22* (48), 5517–5520.
(152) Yoshida, M.; Zhang, Y.; Ye, J.; Suzuki, R.; Imai, Y.; Kimura, S.; Fujiwara, A.; Iwasa, Y. Controlling Charge-Density-Wave States in Nano-Thick Crystals of 1T-TaS_2. *Sci. Rep.* **2014**, *4*, 1–5.
(153) Ovchinnikov, D.; Gargiulo, F.; Allain, A.; Pasquier, D. J.; Dumcenco, D.; Ho, C.-H.; Yazyev, O. V.; Kis, A. Disorder Engineering and Conductivity Dome in ReS_2 with Electrolyte Gating. *Nat. Commun.* **2016**, *7*, 12391.
(154) Yuan, H.; Liu, H.; Shimotani, H.; Guo, H.; Chen, M.; Xue, Q.; Iwasa, Y. Liquid-Gated Ambipolar Transport in Ultrathin Films of a Topological Insulator Bi_2Te_3. *Nano Lett.* **2011**, *11* (7), 2601–2605.
(155) Schladt, T. D.; Graf, T.; Aetukuri, N. B.; Li, M.; Fantini, A.; Jiang, X.; Samant, M. G.; Parkin, S. S. P. Crystal-Facet-Dependent Metallization in Electrolyte-Gated Rutile TiO_2 Single Crystals. *ACS Nano* **2013**, *7* (9), 8074–8081.
(156) Ren, X.; Frisbie, C. D.; Leighton, C. Anomalous Cooling-Rate-Dependent Charge Transport in Electrolyte-Gated Rubrene Crystals. *J. Phys. Chem. Lett.* **2018**, *9* (17), 4828–4833.
(157) Bollinger, A. T.; Dubuis, G.; Yoon, J.; Pavuna, D.; Misewich, J.; Božović, I. Superconductor–insulator Transition in $La_{2-X}Sr_XCuO_4$ at the Pair Quantum Resistance. *Nature* **2011**, *472* (7344), 458–460.
(158) Leng, X.; Garcia-Barriocanal, J.; Bose, S.; Lee, Y.; Goldman, A. M. Electrostatic Control of the Evolution from a Superconducting Phase to an Insulating Phase in Ultrathin $YBa_2Cu_3O_{7-X}$ Films. *Phys. Rev. Lett.* **2011**, *107* (2), 27001.
(159) Ueno, K.; Nakamura, S.; Shimotani, H.; Yuan, H. T.; Kimura, N.; Nojima, T.; Aoki, H.; Iwasa, Y.; Kawasaki, M. Discovery of Superconductivity in $KTaO_3$ by Electrostatic Carrier Doping. *Nat. Nanotechnol.* **2011**, *6* (7), 408–412.
(160) Ye, J. T.; Inoue, S.; Kobayashi, K.; Kasahara, Y.; Yuan, H. T.; Shimotani, H.; Iwasa, Y. Liquid-Gated Interface Superconductivity on an Atomically Flat Film. *Nat. Mater.* **2010**, *9* (2), 125–128.
(161) Ye, J. T.; Zhang, Y. J.; Akashi, R.; Bahramy, M. S.; Arita, R.; Iwasa, Y. Superconducting Dome in a Gate-Tuned Band Insulator. *Science* **2012**, *338* (6111), 1193–1196.
(162) Jo, S.; Costanzo, D.; Berger, H.; Morpurgo, A. F. Electrostatically Induced Superconductivity at the Surface of WS_2. *Nano Lett.* **2015**, *15* (2), 1197–1202.
(163) Yu, Y.; Yang, F.; Lu, X. F.; Yan, Y. J.; Cho, Y.-H.; Ma, L.; Niu, X.; Kim, S.; Son, Y.-W.; Feng, D.; Li, S.; Cheong, S.-W.; Chen, X. H.; Zhang, Y. Gate-Tunable Phase Transitions in Thin Flakes of 1T-TaS_2. *Nat. Nanotechnol.* **2015**, *10* (3), 270–276.
(164) Costanzo, D.; Jo, S.; Berger, H.; Morpurgo, A. F. Gate-Induced Superconductivity in Atomically Thin MoS_2 Crystals. *Nat. Nanotechnol.* **2016**, *11* (4), 339–344.
(165) Yamada, Y.; Ueno, K.; Fukumura, T.; Yuan, H. T.; Shimotani, H.; Iwasa, Y.; Gu, L.; Tsukimoto, S.; Ikuhara, Y.; Kawasaki, M. Electrically Induced Ferromagnetism at Room Temperature in Cobalt-Doped Titanium Dioxide. *Science* **2011**, *332* (6033), 1065–1067.
(166) Shimamura, K.; Chiba, D.; Ono, S.; Fukami, S.; Ishiwata, N.; Kawaguchi, M.;

Kobayashi, K.; Ono, T. Electrical Control of Curie Temperature in Cobalt Using an Ionic Liquid Film. *Appl. Phys. Lett.* **2012**, *100* (12), 122402.
(167) Walter, J.; Wang, H.; Luo, B.; Frisbie, C. D.; Leighton, C. Electrostatic versus Electrochemical Doping and Control of Ferromagnetism in Ion-Gel-Gated Ultrathin $La_{0.5}Sr_{0.5}CoO_{3-\delta}$. *ACS Nano* **2016**, *10* (8), 7799–7810.
(168) Walter, J.; Charlton, T.; Ambaye, H.; Fitzsimmons, M. R.; Orth, P. P.; Fernandes, R. M.; Leighton, C. Giant Electrostatic Modification of Magnetism via Electrolyte-Gate-Induced Cluster Percolation in $La_{0.5}Sr_{0.5}CoO_{3-\delta}$. *Phys. Rev. Mater.* **2018**, *2* (11), 111406.
(169) Weisheit, M.; Fahler, S.; Marty, A.; Souche, Y.; Poinsignon, C.; Givord, D. Electric Field-Induced Modification of Magnetism in Thin-Film Ferromagnets. *Science* **2007**, *315* (5810), 349–351.
(170) Liang, L.; Chen, Q.; Lu, J.; Talsma, W.; Shan, J.; Blake, G. R.; Palstra, T. T. M.; Ye, J. Inducing Ferromagnetism and Kondo Effect in Platinum by Paramagnetic Ionic Gating. *Sci. Adv.* **2018**, *4* (4), eaar2030.
(171) Kang, M. S.; Lee, J.; Norris, D. J.; Frisbie, C. D. High Carrier Densities Achieved at Low Voltages in Ambipolar PbSe Nanocrystal Thin-Film Transistors. *Nano Lett.* **2009**, *9* (11), 3848–3852.
(172) Kang, M. S.; Sahu, A.; Norris, D. J.; Frisbie, C. D. Size- and Temperature-Dependent Charge Transport in PbSe Nanocrystal Thin Films. *Nano Lett.* **2011**, *11* (9), 3887–3892.
(173) Bisri, S. Z.; Piliego, C.; Yarema, M.; Heiss, W.; Loi, M. A. Low Driving Voltage and High Mobility Ambipolar Field-Effect Transistors with PbS Colloidal Nanocrystals. *Adv. Mater.* **2013**, *25* (31), 4309–4314.
(174) Braga, D.; Gutiérrez Lezama, I.; Berger, H.; Morpurgo, A. F. Quantitative Determination of the Band Gap of WS_2 with Ambipolar Ionic Liquid-Gated Transistors. *Nano Lett.* **2012**, *12* (10), 5218–5223.
(175) Zhang, Y.; Ye, J.; Matsuhashi, Y.; Iwasa, Y. Ambipolar MoS_2 Thin Flake Transistors. *Nano Lett.* **2012**, *12* (3), 1136–1140.
(176) Jo, S.; Ubrig, N.; Berger, H.; Kuzmenko, A. B.; Morpurgo, A. F. Mono- and Bilayer WS_2 Light-Emitting Transistors. *Nano Lett.* **2014**, *14* (4), 2019–2025.
(177) Yomogida, Y.; Pu, J.; Shimotani, H.; Ono, S.; Hotta, S.; Iwasa, Y.; Takenobu, T. Ambipolar Organic Single-Crystal Transistors Based on Ion Gels. *Adv. Mater.* **2012**, *24* (32), 4392–4397.
(178) Matsuki, K.; Sakanoue, T.; Yomogida, Y.; Hotta, S.; Takenobu, T. Light Emission from Organic Single Crystals Operated by Electrolyte Doping. *Jpn. J. Appl. Phys.* **2018**, *57* (3S2), 03EF02.
(179) Zaumseil, J.; Ho, X.; Guest, J. R.; Wiederrecht, G. P.; Rogers, J. A. Electroluminescence from Electrolyte-Gated Carbon Nanotube Field-Effect Transistors. *ACS Nano* **2009**, *3* (8), 2225–2234.
(180) Zhang, Y. J.; Oka, T.; Suzuki, R.; Ye, J. T.; Iwasa, Y. Electrically Switchable Chiral Light-Emitting Transistor. *Science* **2014**, *344* (6185), 725–728.
(181) Shimizu, S.; Bahramy, M. S.; Iizuka, T.; Ono, S.; Miwa, K.; Tokura, Y.; Iwasa, Y. Enhanced Thermopower in ZnO Two-Dimensional Electron Gas. *Proc. Natl. Acad. Sci.* **2016**, *113* (23), 6438–6443.
(182) Shimizu, S.; Ono, S.; Hatano, T.; Iwasa, Y.; Tokura, Y. Enhanced Cryogenic

Thermopower in $SrTiO_3$ by Ionic Gating. *Phys. Rev. B* **2015**, *92* (16), 165304.
(183) Takayanagi, R.; Fujii, T.; Asamitsu, A. Simultaneous Control of Thermoelectric Properties in P- and N-Type Materials by Electric Double-Layer Gating: New Design for Thermoelectric Device. *Appl. Phys. Express* **2015**, *8* (5), 51101.
(184) Yoshida, M.; Iizuka, T.; Saito, Y.; Onga, M.; Suzuki, R.; Zhang, Y.; Iwasa, Y.; Shimizu, S. Gate-Optimized Thermoelectric Power Factor in Ultrathin WSe_2 Single Crystals. *Nano Lett.* **2016**, *16* (3), 2061–2065.
(185) Yanagi, K.; Kanda, S.; Oshima, Y.; Kitamura, Y.; Kawai, H.; Yamamoto, T.; Takenobu, T.; Nakai, Y.; Maniwa, Y. Tuning of the Thermoelectric Properties of One-Dimensional Material Networks by Electric Double Layer Techniques Using Ionic Liquids. *Nano Lett.* **2014**, *14* (11), 6437–6442.
(186) Shimizu, S.; Iizuka, T.; Kanahashi, K.; Pu, J.; Yanagi, K.; Takenobu, T.; Iwasa, Y. Thermoelectric Detection of Multi-Subband Density of States in Semiconducting and Metallic Single-Walled Carbon Nanotubes. *Small* **2016**, *12* (25), 3388–3392.
(187) Wang, Y.; Xiao, J.; Zhu, H.; Li, Y.; Alsaid, Y.; Fong, K. Y.; Zhou, Y.; Wang, S.; Shi, W.; Wang, Y.; Zettl, A.; Reed, R. J.; Zhang, X. Structural Phase Transition in Monolayer $MoTe_2$ Driven by Electrostatic Doping. *Nature* **2017**, *550* (7677), 487–491.
(188) Wu, Y.; Chew, A. R.; Rojas, G. A.; Sini, G.; Haugstad, G.; Belianinov, A.; Kalinin, S. V.; Li, H.; Risko, C.; Brédas, J.-L.; Salleo, A.; Frisbie, C. D. Strain Effects on the Work Function of an Organic Semiconductor. *Nat. Commun.* **2016**, *7*, 10270.
(189) Wu, Y.; Ren, X.; McGarry, K. A.; Bruzek, M. J.; Douglas, C. J.; Frisbie, C. D. Scanning Kelvin Probe Microscopy Reveals Planar Defects Are Sources of Electronic Disorder in Organic Semiconductor Crystals. *Adv. Electron. Mater.* **2017**, *3* (7), 1–8.
(190) Hasegawa, T.; Takeya, J. Organic Field-Effect Transistors Using Single Crystals. *Sci. Technol. Adv. Mater.* **2009**, *10* (2), 24314.
(191) Machida, S.; Nakayama, Y.; Duhm, S.; Xin, Q.; Funakoshi, A.; Ogawa, N.; Kera, S.; Ueno, N.; Ishii, H. Highest-Occupied-Molecular-Orbital Band Dispersion of Rubrene Single Crystals as Observed by Angle-Resolved Ultraviolet Photoelectron Spectroscopy. *Phys. Rev. Lett.* **2010**, *104* (15), 156401.
(192) Jiang, Y.; Geng, H.; Shi, W.; Peng, Q.; Zheng, X.; Shuai, Z. Theoretical Prediction of Isotope E Ff Ects on Charge Transport in Organic Semiconductors. *J. Phys. Chem. Lett.* **2014**, *5*, 2267–2273.
(193) Munn, R. W.; Nicholson, J. R.; Siebrand, W.; Williams, D. F. Evidence for an Isotope Effect on Electron Drift Mobilities in Anthracene Crystals. *J. Chem. Phys.* **1970**, *52* (12), 6442.
(194) Munn, R. W.; Siebrand, W. Theory of Charge Carrier Transport in Aromatic Hydrocarbon Crystals. *J. Chem. Phys.* **1970**, *52* (12), 6391.
(195) Morel, D. L.; Hermann, A. M. Isotope Effect for Electron Mobility in Anthracene. *Phys. Lett.* **1971**, *36* (2), 101–102.
(196) Mey, W.; Sonnonstine, T. J.; Morel, D. L.; Hermann, A. M. Drift Mobility of Holes and Electrons in Perdeuterated Anthracene Single Crystals. *J. Chem. Phys.* **1973**, *58* (6), 2542.
(197) Schein, L. B.; McGhie, A. R. Band-Hopping Mobility Transition in Naphthalene and Deuterated Naphthalene. *Phys. Rev. B* **1979**, *20* (4), 1631–1639.

(198) Schein, L. B.; Warta, W.; McGhie, A.; Karl, N. Deuteration Effects on the Electron Mobility in the a Direction of Naphthalene. *Chem. Phys. Lett.* **1980**, *75* (2), 267–270.
(199) Schein, L. B.; Warta, W.; McGhie, A. R.; Karl, N. Mobilities of Electrons and Holes in Naphthalene and Perdeuterated Naphthalene. *Chem. Phys. Lett.* **1983**, *100* (1), 34–36.
(200) Jiang, Y.; Peng, Q.; Geng, H.; Ma, H.; Shuai, Z. Negative Isotope Effect for Charge Transport in Acenes and Derivatives – a Theoretical Conclusion. *Phys. Chem. Chem. Phys.* **2015**, *17* (5), 3273–3280.
(201) Jurchescu, O. D.; Meetsma, A.; Palstra, T. T. M. Low-Temperature Structure of Rubrene Single Crystals Grown by Vapor Transport. *Acta Crystallogr. Sect. B Struct. Sci.* **2006**, *62* (2), 330–334.
(202) Xie, W.; Prabhumirashi, P. L.; Nakayama, Y.; McGarry, K. A.; Geier, M. L.; Uragami, Y.; Mase, K.; Douglas, C. J.; Ishii, H.; Hersam, M. C.; Frisbie, C. D. Utilizing Carbon Nanotube Electrodes to Improve Charge Injection and Transport in Bis(trifluoromethyl)-Dimethyl-Rubrene Ambipolar Single Crystal Transistors. *ACS Nano* **2013**, *7* (11), 10245–10256.
(203) Buchaca-Domingo, E.; Vandewal, K.; Fei, Z.; Watkins, S. E.; Scholes, F. H.; Bannock, J. H.; De Mello, J. C.; Richter, L. J.; DeLongchamp, D. M.; Amassian, A.; Heeney, M.; Salleo, A.; Stingelin, N. Direct Correlation of Charge Transfer Absorption with Molecular Donor:acceptor Interfacial Area via Photothermal Deflection Spectroscopy. *J. Am. Chem. Soc.* **2015**, *137* (16), 5256–5259.
(204) Kronemeijer, A. J.; Pecunia, V.; Venkateshvaran, D.; Nikolka, M.; Sadhanala, A.; Moriarty, J.; Szumilo, M.; Sirringhaus, H. Two-Dimensional Carrier Distribution in Top-Gate Polymer Field-Effect Transistors: Correlation between Width of Density of Localized States and Urbach Energy. *Adv. Mater.* **2014**, *26* (5), 728–733.
(205) Hannewald, K.; Bobbert, P. A. Ab Initio Theory of Charge-Carrier Conduction in Ultrapure Organic Crystals. *Appl. Phys. Lett.* **2004**, *85* (9), 1535–1537.
(206) Vandewal, K.; Albrecht, S.; Hoke, E. T.; Graham, K. R.; Widmer, J.; Douglas, J. D.; Schubert, M.; Mateker, W. R.; Bloking, J. T.; Burkhard, G. F.; Sellinger1, A.; Fréchet, J. M. J.; Amassian, A.; Riede, M. K.; McGehee, M. D.; Neher, D.; Salleo, A. Efficient Charge Generation by Relaxed Charge-Transfer States at Organic Interfaces. *Nat. Mater.* **2013**, *13* (1), 63–68.
(207) Molinari, A. S.; Alves, H.; Chen, Z.; Facchetti, A.; Morpurgo, A. F. High Electron Mobility in Vacuum and Ambient for PDIF-CN_2 Single-Crystal Transistors. *J. Am. Chem. Soc.* **2009**, *131* (7), 2462–2463.
(208) Lee, J. Y.; Roth, S.; Park, Y. W. Anisotropic Field Effect Mobility in Single Crystal Pentacene. *Appl. Phys. Lett.* **2006**, *88* (25), 252106.
(209) McGarry, K. A.; Xie, W.; Sutton, C.; Risko, C.; Wu, Y.; Young, V. G.; Brédas, J. L.; Frisbie, C. D.; Douglas, C. J. Rubrene-Based Single-Crystal Organic Semiconductors: Synthesis, Electronic Structure, and Charge-Transport Properties. *Chem. Mater.* **2013**, *25* (11), 2254–2263.
(210) Chapman, B. D.; Checco, A.; Pindak, R.; Siegrist, T.; Kloc, C. Dislocations and Grain Boundaries in Semiconducting Rubrene Single-Crystals. *J. Cryst. Growth* **2006**, *290* (2), 479–484.
(211) Tello, M.; Chiesa, M.; Duffy, C. M.; Sirringhaus, H. Charge Trapping in Intergrain

Regions of Pentacene Thin Film Transistors. *Adv. Funct. Mater.* **2008**, *18* (24), 3907–3913.
(212) Yogev, S.; Matsubara, R.; Nakamura, M.; Rosenwaks, Y. Local Charge Accumulation and Trapping in Grain Boundaries of Pentacene Thin Film Transistors. *Org. Electron.* **2010**, *11* (11), 1729–1735.
(213) Naden, A. B.; Loos, J.; MacLaren, D. a. Structure–function Relations in diF-TES-ADT Blend Organic Field Effect Transistors Studied by Scanning Probe Microscopy. *J. Mater. Chem. C* **2014**, *2* (2), 245–255.
(214) Bolognesi, A.; Berliocchi, M.; Manenti, M.; Di Carlo, A.; Lugli, P.; Lmimouni, K.; Dufour, C. Effects of Grain Boundaries, Field-Dependent Mobility, and Interface Trap States on the Electrical Characteristics of Pentacene TFT. *IEEE Trans. Electron Devices* **2004**, *51* (12), 1997–2003.
(215) Rivnay, J.; Jimison, L. H.; Northrup, J. E.; Toney, M. F.; Noriega, R.; Lu, S.; Marks, T. J.; Facchetti, A.; Salleo, A. Large Modulation of Carrier Transport by Grain-Boundary Molecular Packing and Microstructure in Organic Thin Films. *Nat. Mater.* **2009**, *8* (12), 952–958.
(216) Robinson, P. M.; Scott, H. G. The Morphology of Anthracene Crystals. *J. Cryst. Growth* **1967**, *1* (4), 187–194.
(217) Corke, N. T.; Kawada, A. A.; Sherwood, J. N. Etching of Dislocations in Crystals of Aromatic Hydrocarbons. *Nature* **1967**, *213* (5071), 62–63.
(218) Pflaum, J.; Niemax, J.; Tripathi, A. K. Chemical and Structural Effects on the Electronic Transport in Organic Single Crystals. *Chem. Phys.* **2006**, *325* (1), 152–159.
(219) Benamara, M.; Zhang, X.; Skowronski, M.; Ruterana, P.; Nouet, G.; Sumakeris, J. J.; Paisley, M. J.; O'Loughline, M. J. Structure of the Carrot Defect in 4H-SiC Epitaxial Layers. *J. Cryst. Growth* **2005**, *86*, 21905.
(220) Sangwal, K.; Owczarek, I. On the Formation of Etch Grooves at Impurity Striations and Growth Sector Boundaries in Crystals Grown from Solutions. *J. Cryst. Growth* **1993**, *129* (3–4), 640–652.
(221) Dimassi, W.; Bouaïcha, M.; Nouri, H.; Boujmil, M. F.; Ben Nasrallah, S.; Bessaïs, B. Grooving of Grain Boundaries in Multicrystalline Silicon: Effect on Solar Cell Performance. *Nucl. Instruments Methods Phys. Res. Sect. B* **2006**, *253* (1–2), 260–263.
(222) Takimiya, K.; Shinamura, S.; Osaka, I.; Miyazaki, E. Thienoacene-Based Organic Semiconductors. *Adv. Mater.* **2011**, *23* (38), 4347–4370.
(223) Li, H.; Tee, B. C.-K.; Cha, J. J.; Cui, Y.; Chung, J. W.; Lee, S. Y.; Bao, Z. High-Mobility Field-Effect Transistors from Large-Area Solution-Grown Aligned C60 Single Crystals. *J. Am. Chem. Soc.* **2012**, *134* (5), 2760–2765.
(224) He, T.; Stolte, M.; Burschka, C.; Hansen, N. H.; Musiol, T.; Kälblein, D.; Pflaum, J.; Tao, X.; Brill, J.; Würthner, F. Single-Crystal Field-Effect Transistors of New Cl_2-NDI Polymorph Processed by Sublimation in Air. *Nat. Commun.* **2015**, *6*, 5954.
(225) Palermo, V.; Palma, M.; Samori, P. Electronic Characterization of Organic Thin Films by Kelvin Probe Force Microscopy. *Adv. Mater.* **2006**, *18* (2), 145–164.
(226) Ono, S.; Miwa, K.; Seki, S.; Takeya, J. A Comparative Study of Organic Single-Crystal Transistors Gated with Various Ionic-Liquid Electrolytes. *Appl. Phys. Lett.* **2009**, *94* (6), 10–13.

(227) Ono, S.; Minder, N.; Chen, Z.; Facchetti, A.; Morpurgo, A. F. High-Performance N-Type Organic Field-Effect Transistors with Ionic Liquid Gates. *Appl. Phys. Lett.* **2010**, *97* (14), 143307.
(228) Xie, W.; Liu, F.; Shi, S.; Ruden, P. P.; Frisbie, C. D. Charge Density Dependent Two-Channel Conduction in Organic Electric Double Layer Transistors (EDLTs). *Adv. Mater.* **2014**, *26* (16), 2527–2532.
(229) Lee, B.; Chen, Y.; Fu, D.; Yi, H. T.; Czelen, K.; Najafov, H.; Podzorov, V. Trap Healing and Ultralow-Noise Hall Effect at the Surface of Organic Semiconductors. *Nat. Mater.* **2013**, *12* (12), 1125–1129.
(230) Naber, R. C. G.; Tanase, C.; Blom, P. W. M.; Gelinck, G. H.; Marsman, A. W.; Touwslager, F. J.; Setayesh, S.; de Leeuw, D. M. High-Performance Solution-Processed Polymer Ferroelectric Field-Effect Transistors. *Nat. Mater.* **2005**, *4* (3), 243–248.
(231) Sianesi, D.; Zamboni, V.; Fontanelli, R.; Binaghi, M. Perfluoropolyethers: Their Physical Properties and Behaviour at High and Low Temperatures. *Wear* **1971**, *18* (2), 85–100.
(232) Goldman, A. M. Electrostatic Gating of Ultrathin Films. *Annu. Rev. Mater. Res.* **2014**, *44* (1), 45–63.
(233) Bisri, S. Z.; Shimizu, S.; Nakano, M.; Iwasa, Y. Endeavor of Iontronics: From Fundamentals to Applications of Ion-Controlled Electronics. *Adv. Mater.* **2017**, *29* (25), 1607054.
(234) Walter, J.; Yu, G.; Yu, B.; Grutter, A.; Kirby, B.; Borchers, J.; Zhang, Z.; Zhou, H.; Birol, T.; Greven, M.; et al. Ion-Gel-Gating-Induced Oxygen Vacancy Formation in Epitaxial $La_{0.5}Sr_{0.5}CoO_{3-\delta}$ Films from in Operando X-Ray and Neutron Scattering. *Phys. Rev. Mater.* **2017**, *1* (7), 71403.
(235) Haddon, R. C. Electronic Structure, Conductivity and Superconductivity of Alkali Metal Doped C60. *Acc. Chem. Res.* **1992**, *25* (3), 127–133.
(236) Mitsuhashi, R.; Suzuki, Y.; Yamanari, Y.; Mitamura, H.; Kambe, T.; Ikeda, N.; Okamoto, H.; Fujiwara, A.; Yamaji, M.; Kawasaki, N.; Maniwa, Y.; Kubozono, Y. Superconductivity in Alkali-Metal-Doped Picene. *Nature* **2010**, *464* (7285), 76–79.
(237) Cohen, M. J.; Coleman, L. B.; Garito, A. F.; Heeger, A. J. Electrical Conductivity of Tetrathiofulvalinium Tetracyanoquinodimethan (TTF) (TCNQ). *Phys. Rev. B* **1974**, *10* (4), 1298–1307.
(238) Jérome, D.; Mazaud, A.; Ribault, M.; Bechgaard, K. Superconductivity in a Synthetic Organic Conductor $(TMTSF)_2PF_6$. *J. Phys. Lettres* **1980**, *41* (4), 95–98.
(239) Shimotani, H.; Asanuma, H.; Takeya, J.; Iwasa, Y. Electrolyte-Gated Charge Accumulation in Organic Single Crystals. *Appl. Phys. Lett.* **2006**, *89* (20), 8–11.
(240) Atallah, T. L.; Gustafsson, M. V.; Schmidt, E.; Frisbie, C. D.; Zhu, X.-Y. Charge Saturation and Intrinsic Doping in Electrolyte-Gated Organic Semiconductors. *J. Phys. Chem. Lett.* **2015**, *6* (23), 4840–4844.
(241) Xia, Y.; Xie, W.; Ruden, P. P.; Frisbie, C. D. Carrier Localization on Surfaces of Organic Semiconductors Gated with Electrolytes. *Phys. Rev. Lett.* **2010**, *105* (3), 36802.
(242) Sato, T.; Kagawa, F.; Kobayashi, K.; Miyagawa, K.; Kanoda, K.; Kumai, R.; Murakami, Y.; Tokura, Y. Emergence of Nonequilibrium Charge Dynamics in a Charge-Cluster Glass. *Phys. Rev. B* **2014**, *89* (12), 121102.

(243) Paulsen, B. D.; Frisbie, C. D. Dependence of Conductivity on Charge Density and Electrochemical Potential in Polymer Semiconductors Gated with Ionic Liquids. *J. Phys. Chem. C* **2012**, *116* (4), 3132–3141.
(244) Zabrodskii, A. G. The Coulomb Gap: The View of an Experimenter. *Philos. Mag. Part B* **2001**, *81* (9), 1131–1151.
(245) Uhl, B.; Cremer, T.; Roos, M.; Maier, F.; Steinrück, H.-P.; Behm, R. J. At the Ionic Liquid|metal Interface: Structure Formation and Temperature Dependent Behavior of an Ionic Liquid Adlayer on Au(111). *Phys. Chem. Chem. Phys.* **2013**, *15* (40), 17295.
(246) Shimakawa, K. Multiphonon Hopping of Electrons on Defect Clusters in Amorphous Germanium. *Phys. Rev. B* **1989**, *39* (17), 12933–12936.
(247) Wienkes, L. R.; Blackwell, C.; Hutchinson, T.; Kakalios, J. Conduction Mechanisms in Doped Mixed-Phase Hydrogenated Amorphous/nanocrystalline Silicon Thin Films. *J. Appl. Phys.* **2013**, *113* (23), 233707.
(248) Kagawa, F.; Sato, T.; Miyagawa, K.; Kanoda, K.; Tokura, Y.; Kobayashi, K.; Kumai, R.; Murakami, Y. Charge-Cluster Glass in an Organic Conductor. *Nat. Phys.* **2013**, *9* (7), 419–422.
(249) Sato, T.; Kagawa, F.; Kobayashi, K.; Ueda, A.; Mori, H.; Miyagawa, K.; Kanoda, K.; Kumai, R.; Murakami, Y.; Tokura, Y. Systematic Variations in the Charge-Glass-Forming Ability of Geometrically Frustrated θ-(BEDT-TTF)$_2$X Organic Conductors. *J. Phys. Soc. Japan* **2014**, *83* (8), 83602.
(250) Mahmoudian, S.; Rademaker, L.; Ralko, A.; Fratini, S.; Dobrosavljević, V. Glassy Dynamics in Geometrically Frustrated Coulomb Liquids without Disorder. *Phys. Rev. Lett.* **2015**, *115* (2), 25701.
(251) Devlin, R. C.; Krick, A. L.; Sichel-Tissot, R. J.; Xie, Y. J.; May, S. J. Electronic Transport and Conduction Mechanism Transition in $La_{1/3}Sr_{2/3}FeO_3$ Thin Films. *J. Appl. Phys.* **2014**, *115* (23), 233704.
(252) Zimmermann, M. v; Vigliante, A.; Niemöller, T.; Ichikawa, N.; Frello, T.; Madsen, J.; Wochner, P.; Uchida, S.; Andersen, N. H.; Tranquada, J. M.; Gibbs, D.; Schneider J. R. Hard–X-Ray Diffraction Study of Charge Stripe Order in $La_{1.48}Nd_{0.4}Sr_{0.12}CuO_4$. *Europhys. Lett.* **1998**, *41* (6), 629–634.
(253) Fink, J.; Schierle, E.; Weschke, E.; Geck, J.; Hawthorn, D.; Soltwisch, V.; Wadati, H.; Wu, H.-H.; Dürr, H. A.; Wizent, N.; Büchner, B.; Sawatzky, G. A. Charge Ordering in $La_{1.8-x}Eu_{0.2}Sr_xCuO_4$ Studied Studied by Resonant Soft X-Ray Diffraction. *Phys. Rev. B* **2009**, *79* (10), 100502.
(254) Blackburn, E.; Chang, J.; Hücker, M.; Holmes, A. T.; Christensen, N. B.; Liang, R.; Bonn, D. A.; Hardy, W. N.; Rütt, U.; Gutowski, O.; Zimmermann, M. V.; Forgan, E. M.; Hayden, S. M. X-Ray Diffraction Observations of a Charge-Density-Wave Order in Superconducting Ortho-II $YBa_2Cu_3O_{6.54}$. *Phys. Rev. Lett.* **2013**, *110* (13), 137004.
(255) da Silva Neto, E. H.; Yu, B.; Minola, M.; Sutarto, R.; Schierle, E.; Boschini, F.; Zonno, M.; Bluschke, M.; Higgins, J.; Li, Y.; Yu, G.; Weschke, E.; He, F.; Le Tacon, M.; Greene, R. L.; Greven, M.; Sawatzky, G. A.; Keimer, B.; Damascelli, A. Doping-Dependent Charge Order Correlations in Electron-Doped Cuprates. *Sci. Adv.* **2016**, *2* (8), e1600782.
(256) Okuyama, D.; Nakano, M.; Takeshita, S.; Ohsumi, H.; Tardif, S.; Shibuya, K.;

Hatano, T.; Yumoto, H.; Koyama, T.; Ohashi, H.; Takata, M.; Kawasaki, M.; Arima, T.; Tokura, Y. Iwasa, Y. Gate-Tunable Gigantic Lattice Deformation in VO_2. *Appl. Phys. Lett.* **2014**, *104* (2), 23507.

(257) Dubuis, G.; Yacoby, Y.; Zhou, H.; He, X.; Bollinger, A. T.; Pavuna, D.; Pindak, R.; Božović, I. Oxygen Displacement in Cuprates under Ionic Liquid Field-Effect Gating. *Sci. Rep.* **2016**, *6* (1), 32378.

(258) Leng, X.; Pereiro, J.; Strle, J.; Dubuis, G.; Bollinger, A. T.; Gozar, A.; Wu, J.; Litombe, N.; Panagopoulos, C.; Pavuna, D.; Božović, I. Insulator to Metal Transition in WO_3 Induced by Electrolyte Gating. *npj Quantum Mater.* **2017**, *2* (1), 35.

(259) Lu, N.; Zhang, P.; Zhang, Q.; Qiao, R.; He, Q.; Li, H.-B.; Wang, Y.; Guo, J.; Zhang, D.; Duan, Z.; Li, Z.; Wang, M.; Yang, S.; Yan, M.; Arenholz, E.; Zhou, S.; Yang, W.; Gu, L.; Nan, C.; Wu, J.; Tokura, Y.; Yu, P. Electric-Field Control of Tri-State Phase Transformation with a Selective Dual-Ion Switch. *Nature* **2017**, *546* (7656), 124–128.

(260) Dong, Y.; Xu, H.; Luo, Z.; Zhou, H.; Fong, D. D.; Wu, W.; Gao, C. Effect of Gate Voltage Polarity on the Ionic Liquid Gating Behavior of $NdNiO_3/NdGaO_3$ Heterostructures. *APL Mater.* **2017**, *5* (5), 51101.

(261) Perez-Muñoz, A. M.; Schio, P.; Poloni, R.; Fernandez-Martinez, A.; Rivera-Calzada, A.; Cezar, J. C.; Salas-Colera, E.; Castro, G. R.; Kinney, J.; Leon, C.; Santamaria, J.; Garcia-Barriocanal, J.; Goldman, A. M. In Operando Evidence of Deoxygenation in Ionic Liquid Gating of $YBa_2Cu_3O_{7-X}$. *Proc. Natl. Acad. Sci.* **2017**, *114* (2), 215–220.

(262) Wang, W.; Kang, D.; Dai, W.; Tai, Y.-C. Reliable Deposition of Ultra-Thin Parylene. In *2016 IEEE 29th International Conference on Micro Electro Mechanical Systems (MEMS)*; IEEE, 2016; Vol. 2016–Febru, pp 462–464.

(263) Gallagher, P.; Lee, M.; Petach, T. A.; Stanwyck, S. W.; Williams, J. R.; Watanabe, K.; Taniguchi, T.; Goldhaber-Gordon, D. A High-Mobility Electronic System at an Electrolyte-Gated Oxide Surface. *Nat. Commun.* **2015**, *6* (1), 6437.

(264) Xi, X.; Berger, H.; Forró, L.; Shan, J.; Mak, K. F. Gate Tuning of Electronic Phase Transitions in Two-Dimensional $NbSe_2$. *Phys. Rev. Lett.* **2016**, *117* (10), 106801.

(265) Li, L. J.; O'Farrell, E. C. T.; Loh, K. P.; Eda, G.; Özyilmaz, B.; Castro Neto, A. H. Controlling Many-Body States by the Electric-Field Effect in a Two-Dimensional Material. *Nature* **2016**, *529* (7585), 185–189.

(266) Petach, T. A.; Reich, K. V.; Zhang, X.; Watanabe, K.; Taniguchi, T.; Shklovskii, B. I.; Goldhaber-Gordon, D. Disorder from the Bulk Ionic Liquid in Electric Double Layer Transistors. *ACS Nano* **2017**, *11* (8), 8395–8400.

Appendix

A1 Supporting information for Chapter 5

A1.1 Structural and vibrational analysis

Temperature	123(2) K
Wavelength	1.54178 Å
Crystal system	Orthorhombic
Space group	Cmca
a	26.8188(14) Å
b	7.1626(4) Å
c	14.2278(8) Å
α	90°
β	90°
γ	90°
Volume	2733.1(3) $Å^3$
Z	4

Table A1.1 Crystal data for vapor-grown ^{13}C-rubrene single crystals. The crystal structure of rubrene is not changed after ^{13}C-substitution.

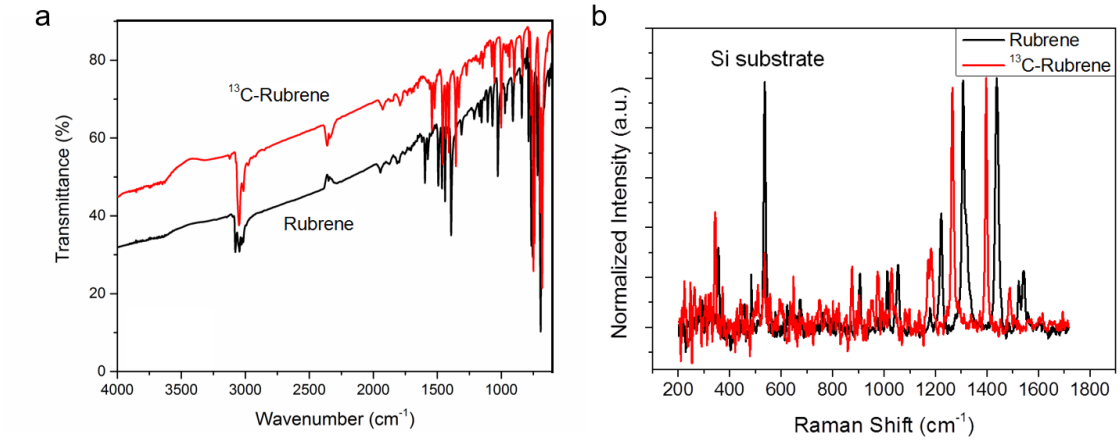

Figure A1.1 (a) IR and (b) Raman spectra of native rubrene and ^{13}C-rubrene. The spectra demonstrate that ^{13}C-substitution leads to a red-shift for all the vibrational modes in rubrene.

A1.2 Calculations of the confidence intervals on the mean values of mobility

To find the confidence intervals on the mean values of mobility, t-test is employed based on the full statistics of mobility. The confidence interval can be represented as $\bar{\mu} \pm t\sigma/\sqrt{n}$, where $\bar{\mu}$ is the mean, t is a parameter which depends on the sample size and the confidence level and can be found in the t-table, σ is the standard deviation, and n is the sample size. It should be noted that the correct t values sit in the row of $N = n - 1$ in the t-table, where N is the degree of freedom. The results are summarized in the following tables.

	$\bar{\mu}$ ($cm^2V^{-1}s^{-1}$)	σ ($cm^2V^{-1}s^{-1}$)	n
rubrene	14.59	2.37	74
^{13}C-rubrene	12.57	2.23	74

Table A1.2 Statistical data of mobility.

confidence level	**90%**	**95%**	**97.5%**	**99%**
t **(*N* = 73)**	1.6660	1.9930	2.2886	2.6449
$t\sigma/\sqrt{n}$ **for rubrene ($cm^2V^{-1}s^{-1}$)**	0.46	0.55	0.63	0.73
$t\sigma/\sqrt{n}$ **for ^{13}C-rubrene ($cm^2V^{-1}s^{-1}$)**	0.43	0.52	0.59	0.69
confidence interval for rubrene ($cm^2V^{-1}s^{-1}$)	(14.13, 15.05)	(14.04, 15.14)	(13.96, 15.22)	(13.86, 15.32)
confidence interval for ^{13}C-rubrene ($cm^2V^{-1}s^{-1}$)	(12.14, 13.00)	(12.05, 13.09)	(11.98, 13.16)	(11.88, 13.26)

Table A1.3 Confidence intervals on the mean values of mobility.

A2 Supporting information for Chapter 6

A2.1 Histogram of the surface potential differences

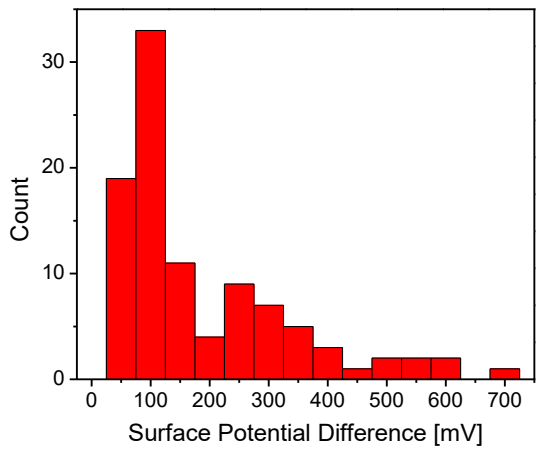

Figure A2.1 Histogram of the average surface potential differences between the dark and bright stripes measured in 100 FM-rubrene samples. The distribution shows a large tail with the surface potential difference goes towards up to 700 mV. The mean surface potential difference is ~100 mV.

A2.2 More XRD data of FM-rubrene and rubrene crystals

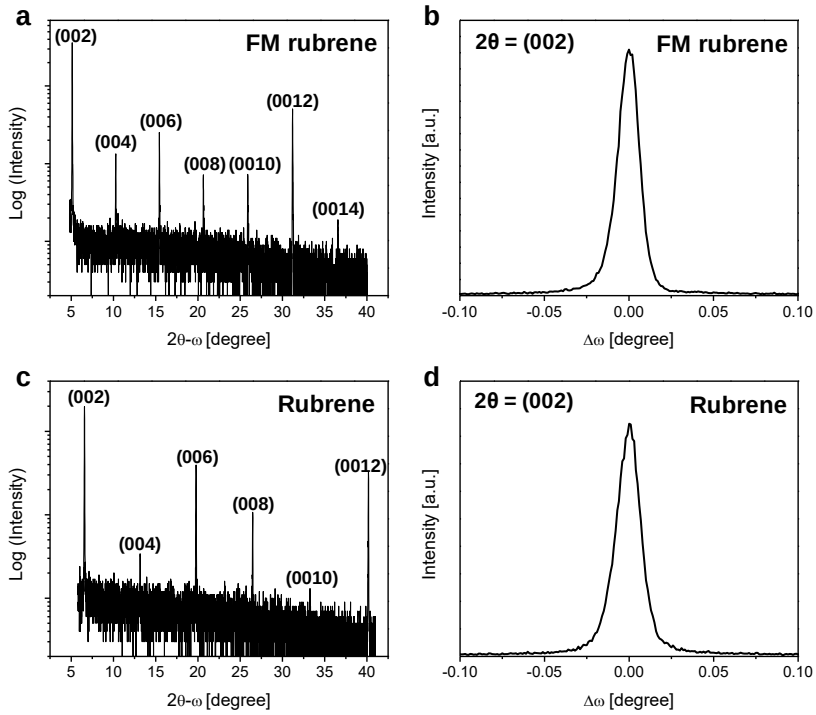

Figure A2.2 Out-of-plane XRD of FM-rubrene and rubrene single crystals. (a) Typical wide-angle out-of-plane 2θ–ω diffraction pattern (coupled scan) for FM-rubrene crystal. A series of narrow and high intensity peaks are observed, corresponding to the family of (002) planes. (b) Out-of-plane ω-scan pattern (rocking curve) of FM-rubrene when 2θ is fixed at 5.13°, the Bragg diffraction angle of (002) plane. The full-width-at-half-maximum (FWHM) of the rocking curve is around 0.016°. (c) Typical wide-angle out-of-plane 2θ–ω diffraction pattern (coupled scan) for rubrene crystal. A series of narrow and high intensity peaks are observed, corresponding to the family of (002) planes. (d) Out-of-plane ω-scan pattern (rocking curve) of rubrene when 2θ is fixed at 6.58°, the Bragg diffraction angle of (002) plane. The full-width-at-half-maximum (FWHM) in the rocking curve, known as the mosaicity spread, is only 0.018°.

Plane	**h**	**k**	**l**	**d/Å**	**2θ/degree**	**Multiplicity**
(020)	0	2	0	3.6251	24.5365	2
(021)	0	2	1	3.5095	25.3577	4
(004)	0	0	4	3.5028	25.4071	2
(022)	0	2	2	3.2196	27.6848	4

Table A2.1 FM-rubrene in-plane diffraction peaks. Diffraction of (002) plane was chosen for the scan measurement because its d-spacing, and thus the 2θ value is distinct from other planes. This could ensure that the observed peaks in the ϕ scan are all from (022).

T/K	283	333	383	433	483
Crystal Structure	Orthorhombic	Orthorhombic	Orthorhombic	Orthorhombic	Orthorhombic
a/Å	26.9113	26.9470	26.9777	26.9838	27.0233
b/Å	7.1900	7.2037	7.2163	7.2261	7.2344
c/Å	14.4248	14.4922	14.5586	14.6213	14.6853
α	90.0000	90.0000	90.0000	90.0000	90.0000
β	90.0000	90.0000	90.0000	90.0000	90.0000
γ	90.0000	90.0000	90.0000	90.0000	90.0000
V/Å^3	2791.082	2813.187	2834.271	2850.961	2870.919

Table A2.2 Unit cell parameters of rubrene as a function of temperature. Unlike FM-rubrene, the crystal structure of rubrene retains as temperature changes.

A2.3 Analysis of the strain associated with the solid-solid phase transition

For FM-rubrene crystals, there is an orthorhombic to triclinic phase transition between 333 K and 383 K. At 333 K, the orthorhombic lattice constants are a = 34.2709 Å, b = 7.2797 Å, c = 14.1173 Å, $\alpha = \beta = \gamma = 90°$; at 383 K, the triclinic lattice parameters are a = 17.4039 Å, b = 7.3439 Å, c = 14.1270 Å, α = 89.2403°, β = 87.7138°, γ = 78.0939°. At first glance one would think a and γ change a lot after the phase transition. However, as shown in Figure A2.3, the a axis in the triclinic lattice is actually along the [110] direction of the orthorhombic lattice. The corresponding changes thus should be from 17.5178 Å to 17.4039 Å for a, and from 78.0077° to 78.0939° for γ. Therefore, the phase transition does not affect the molecular packing very much, only "tilting" the unit cell. The largest change in the lattice parameters is the change of β, which corresponds to a shear strain of 4% (estimated from $\varepsilon = \tan[90° - 87.7138°]$). Such a tremendous strain may explain the origin of planar defects. For example, although this shear strain lies in the a-c plane, it can be decomposed into a component along the [011] direction that may be partially released by the formation of stacking faults.

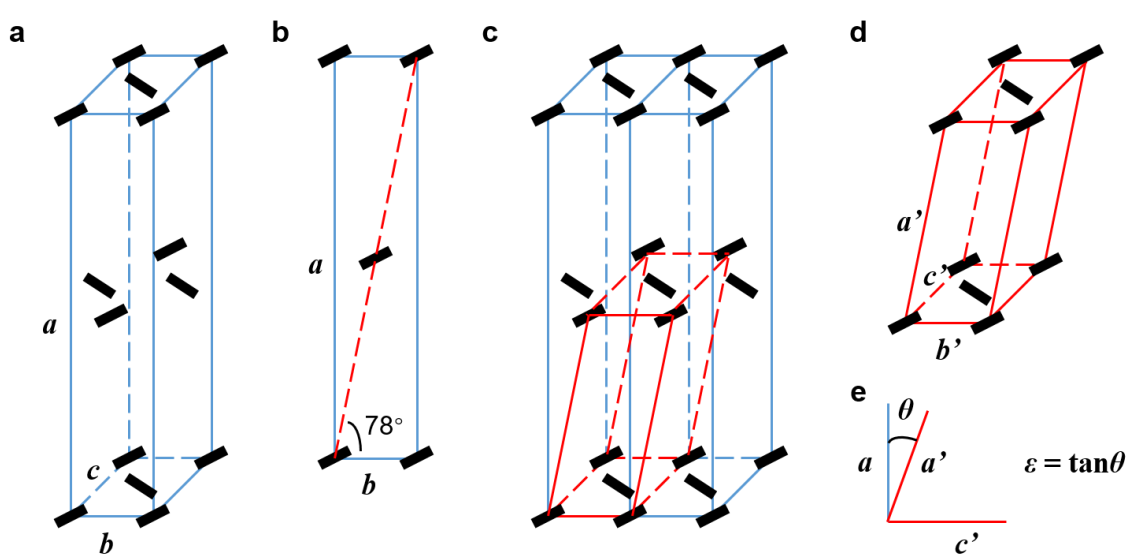

Figure A2.3 Schematics of the orthorhombic to triclinic phase transition. (a) The orthorhombic unit cell of FM-rubrene. Each black rectangle represents an FM-rubrene molecule. (b) The *a-b* plane of the orthorhombic unit cell. The angle between [110] and [010] is 78°, which is very close to the value of γ in the triclinic unit cell. (c) The orientational relationship between the orthorhombic and the triclinic unit cell. After phase transition, the red parallelepiped becomes the new unit cell. (d) the triclinic unit cell of FM-rubrene. Note that the *c* axis is no longer perpendicular to the *a-b* plane. (e) Schematic of the shear strain caused by the change of β.

A2.4 SKPM images of more organic semiconductors

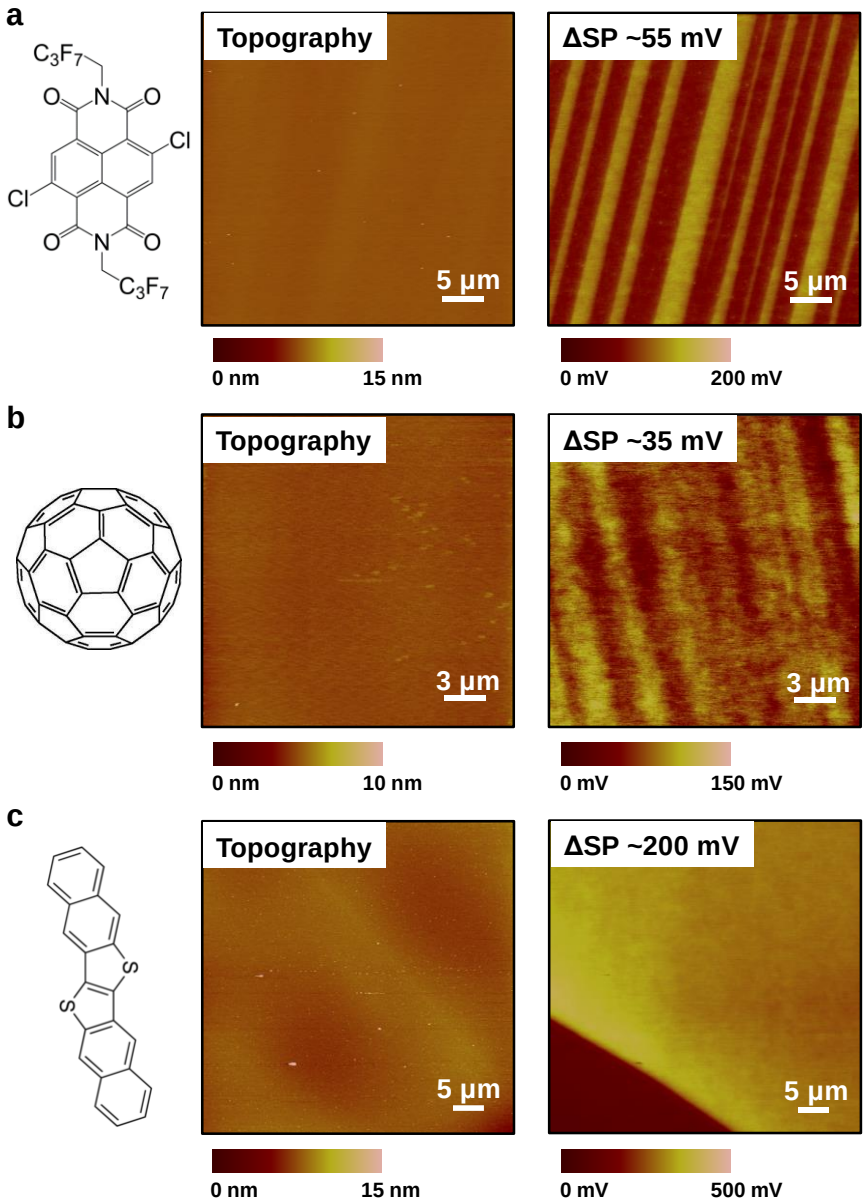

Figure A2.4 Surface potential stripes observed in single crystals of other organic materials. (a) Topography and corresponding surface potential maps of a naphthalene diimide derivative (Cl_2-NDI) single crystal. Parallel surface potential stripes similar to that observed in FM-rubrene crystals are observed. The average potential difference is ~55 mV. Note that <10% of the crystals investigated exhibited this phenomenon. (b) Topography and corresponding surface potential maps of a buckminsterfullerene (C60) single crystal. Parallel surface potential stripes similar to that observed in FM-rubrene crystals are also observed. The average potential difference is ~35 mV. Also, <10% of the crystals investigated exhibited this phenomenon. (c) Topography and corresponding surface potential maps of a dinaphtho[2,3-b:2,3-f]thieno[3,2-b]thiophene (DNTT) single crystal. Very wide surface potential stripes are observed and the potential difference is ~200 mV. About 50% of the crystals investigated showed this phenomenon.

A3 Supporting information for Chapter 7

A3.1 Estimating the dielectric constant of PFPE

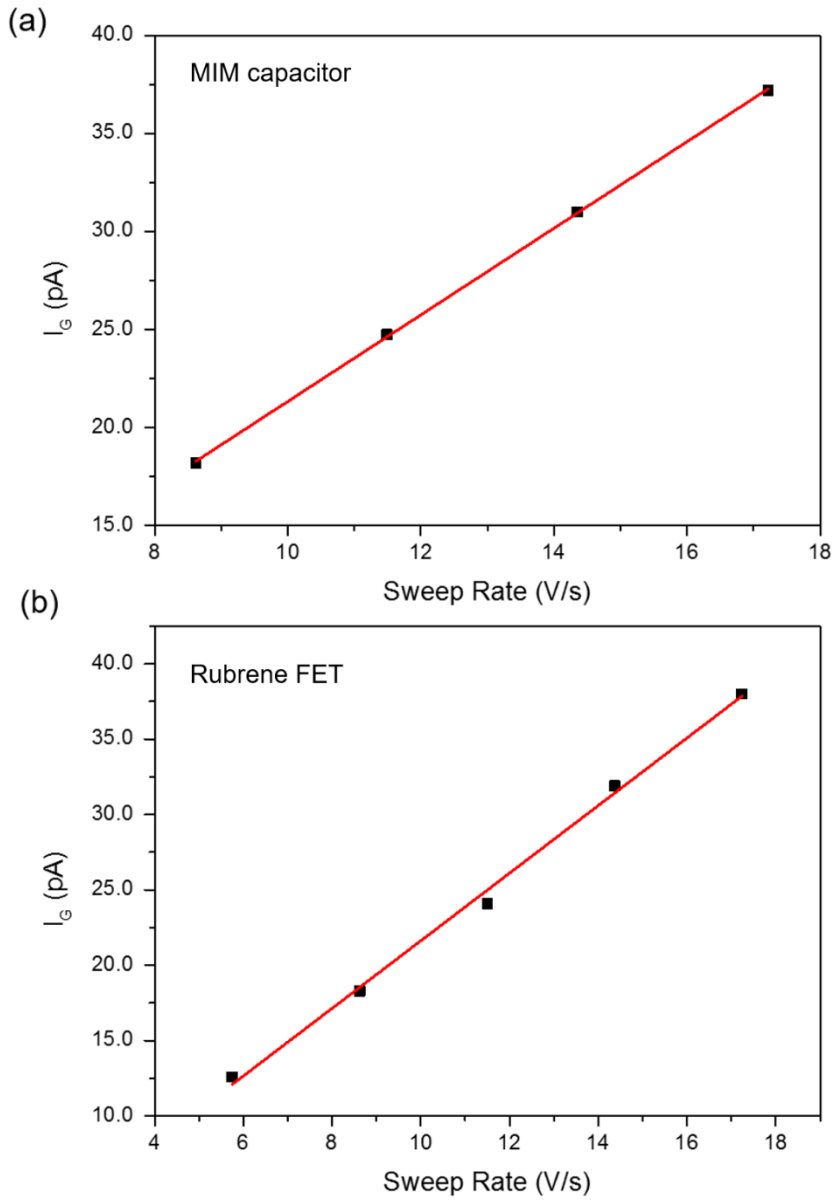

Figure A3.1 Gate displacement current as a function of sweep rate for a PFPE MIM capacitor (a) and a PFPE-gated rubrene FET (b). For the FET, the values of current are taken from the plateau regions on the left of the peaks in the reverse sweep in Figure 7.2b. The slope is the total capacitance of the devices. The calculated specific capacitances are respectively 0.71 nF/cm^2 for (a) and 0.74 nF/cm^2 for (b), which corresponds to a dielectric

constant of 4 (the air-gap capacitance is 0.18 nF/cm^2 for a 5 μm gap). Device dimensions: (a) L = 500 μm, W = 620 μm; (b) L = 500 μm, W = 600 μm.

A3.2 Low-temperature measurements of PFPE-gated rubrene transistors

To further confirm the relationship between the transfer curve hysteresis and the DCM peaks, we carried out low temperature measurements on PFPE-gated rubrene FETs. As shown in Figure A3.2a, when the temperature is reduced to 280 K, the positions of the two peaks are shifted to more negative and positive voltages respectively. Correspondingly, the hysteresis in the transfer curve also becomes larger at 280 K (Figure A3.2b). This is consistent with a larger barrier to dipole reversal in the pinned/anisotropic paraelectric picture.

If the temperature is below the freezing point of PFPE (~240 K), the liquid loses its flow characteristics and the shape of the DCM curve changes significantly. First, the peaks are absent, and the hysteresis becomes negligible in the transfer curve; second, there is no sign of charge injection and extraction in the DCM curve, which now looks like what we would expect from an MIM capacitor. The high conductance in the rubrene channel comes from the "frozen" dipoles aligned at the PFPE/rubrene interface, because the temperature is below the freezing point of PFPE. In this case, the charge carrier density in the channel is so high that the device cannot be turned off, which is demonstrated by the high off-current at 210 K in Figure A3.2b. Additionally, the shape of the DCM curve at 210 K can be tuned by applying a gate bias. If a positive bias is held during cooling (V_G = 30 V), instead of exhibiting a box-shaped DCM curve, the device behaves like a transistor with a

conventional dielectric because there is no dipole-induced charge in the channel (rubrene conducts only for hole accumulation), exhibiting a clear turn-on and turn-off (Figure A3.3).

Based on all the data shown above, a direct relationship can be built between the hysteresis in the transfer curves and the peaks in the DCM curves and can be explained by the response of the dipoles to the applied gate electric field. The origin of this dipolar response is more subtle, and is discussed in the manuscript.

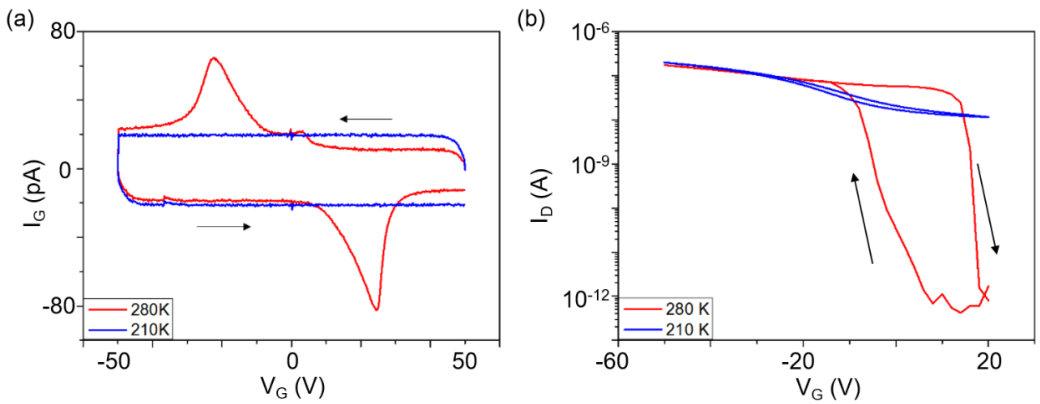

Figure A3.2 (a) Temperature-dependence of the displacement currents for a PFPE-gated FET. (b) Corresponding transfer curves at the same temperatures. The relationship between the hysteresis and the peaks is further confirmed. At 280 K, the distance between the two peaks in the displacement current becomes larger, and a larger hysteresis also appears in the transfer curve. At 210 K, no peak is observed in the displacement current, so the hysteresis in the transfer curve also becomes negligible. Device dimensions: L = 500 μm, W = 390 μm.

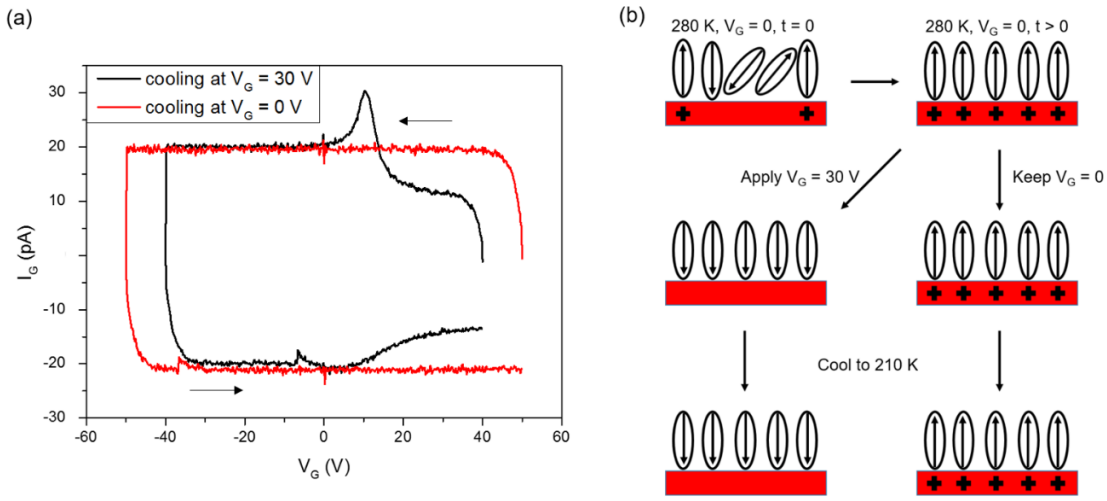

Figure A3.3 (a) Displacement currents at 210 K of a PFPE-gated FET with different cooling conditions. If a positive bias is held during cooling (V_G = 30 V), the shape of the curve is close to what we would expect from a conventional dielectric device; however, if there is no applied gate bias during cooling, the obtained box-shaped curve is close to what we expect from a metal-insulator-metal structure. (b) The influence of gate voltage on the schematic arrangement of dipoles during cooling. If V_G = 30 V is held, there is no surface charge accumulation at the rubrene/PFPE interface. Device dimensions: L = 500 μm, W = 390 μm.

A3.3 An example of a PFPE-gated DNTT single crystal transistor

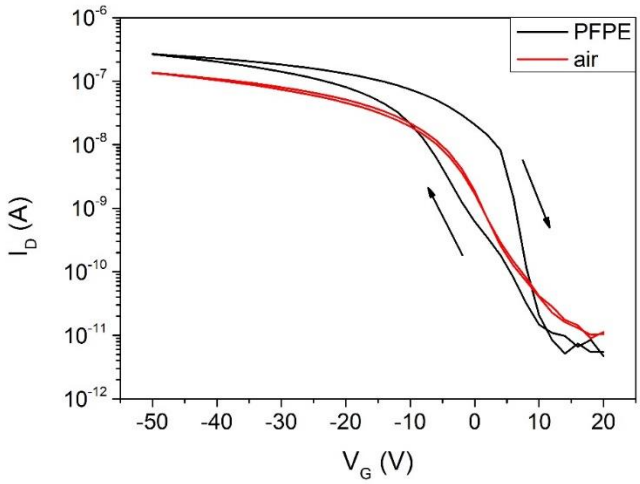

Figure A3.4 Transfer curves of a DNTT single crystal transistor with different dielectrics: air (red) and PFPE (black). A large hysteresis again appears in the transfer curve of PFPE-gated device. Device dimensions: L = 50 μm, W = 675 μm.

A3.4 An example of the Hall effect at 240 K

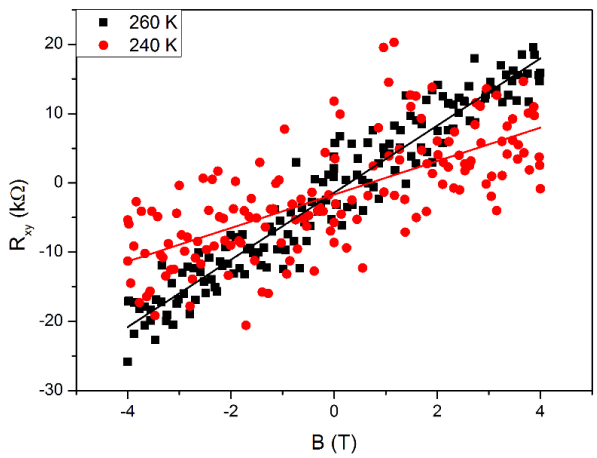

Figure A3.5 Hall measurements of a PFPE-gated FET at 260 K and 240 K. The slope of the fitted line at 260 K is 4.85 kΩ/T with R^2 = 0.93, while for data at 240 K the slope is 2.41 kΩ/T with R^2 = 0.48. At 240 K the noise level is much higher, and the slope becomes smaller. Device dimensions: ΔL = 250 μm, W = 220 μm.

A4 Supporting information for Chapter 8

A4.1 Typical transfer curve and induced charge density in a rubrene EGT

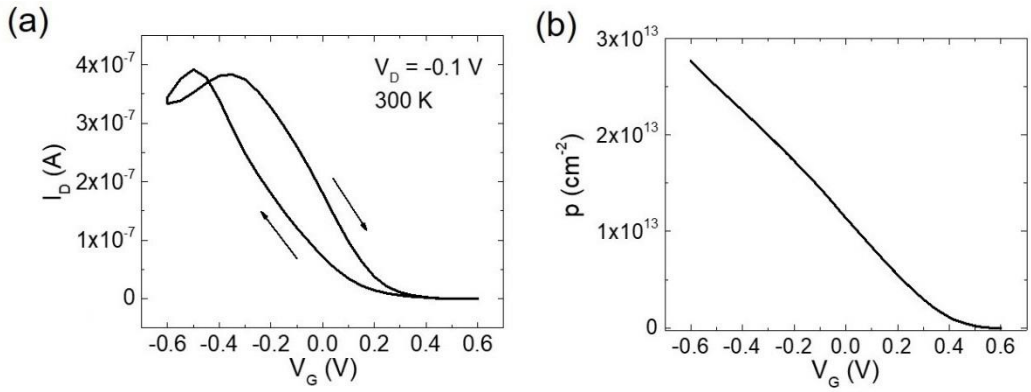

Figure A4.1 (a) Typical 300 K transfer curve for a rubrene EGT at a sweep rate of 50 mV/s. Device dimensions: L = 300 μm, W = 340 μm. (b) V_G-dependent hole density for the same device, as determined from gate displacement current measurements.

A4.2 Verification of temperature dependence from Zabrodskii plots

To describe *R-T* characteristics, a reduced activation energy (W) as a logarithmic derivative of $R(T)$ can be defined as:

$$W = -\frac{d(\ln R)}{d(\ln T)}$$

If *R(T)* follows a thermally-activated *T*-dependence of the form $R \propto \exp(T_0/T)^n$, the reduced activation energy then becomes:

$$\ln W = A - n \ln T$$

where A is a constant. The values of n are then determined from the slopes of Zabrodskii plots, i.e., plots of $\ln W$-$\ln T$.

If *R(T)* follows a power law *T* dependence, on the other hand, of the form $R \propto T^{-m}$, then *W* becomes a constant (*W* = *m*), such that ln*W*-ln*T* plots should have zero slope.

In the context of the above, consider the data shown in Figure A4.2 below. For V_G = -0.5 V, -1 V, and -1.5 V, reasonable adherence to thermally-activated behavior is observed, *i.e.*, the ln*W*-ln*T* plots are reasonably close to straight lines with clearly negative slopes in the low *T* limit. For the other 3 curves, however, at V_G = -2 V, -2.5 V and -3 V, zero slope is observed over a significant *T* range, evidencing power-law behavior. These conclusions are supported by Arrhenius fitting and log-log fitting as in Figure 8.1 in the main article. Note that at higher temperatures, negative values of ln*W* are obtained in Figure A4.2, evidencing non-exponential, weak temperature dependence, with positive temperature coefficient of resistance.

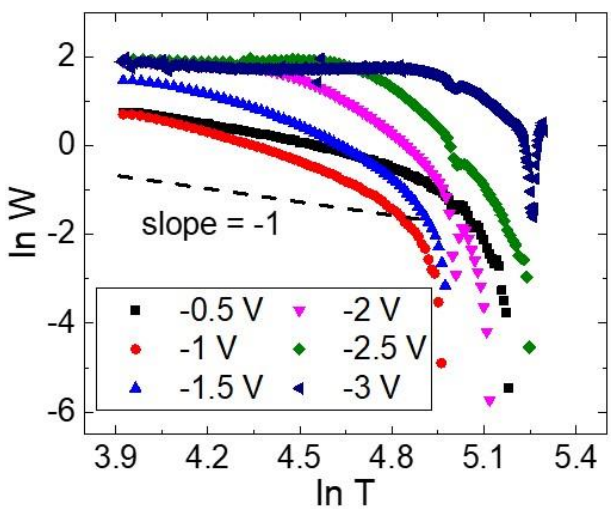

Figure A4.2 ln*W*-ln*T* plots for the data shown in Figure 8.1d.

A4.3 Differential scanning calorimetry (DSC)

Differential scanning calorimetry measurements were carried out using a TA Instruments Q1000 DSC with liquid nitrogen cooling capability. A sample of 5–10 mg was contained in a hermetically sealed aluminum pan. Data were acquired during cooling, on the first cooling and heating cycle performed, at 1 K/min and 10 K/min.

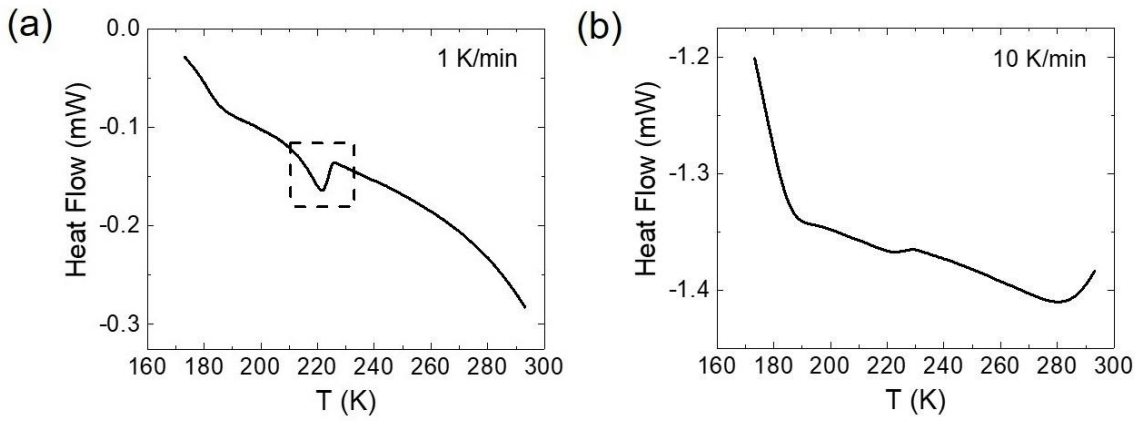

Figure A4.3 DSC data on [P14][FAP] taken during cooling at different cooling rates: (a) 1 K/min and (b) 10 K/min. A crystallization peak is observed at 1 K/min, but it does not show up at 10 K/min.

A4.4 Freezing point of [P14][FAP] and fast quenching across the freezing point

The following transport experiment was also used to determine the freezing point of [P14][FAP]. A negative V_G (-2.5 V) was first applied at 240 K, then a device was cooled to 200 K and V_G was changed to 0 at 200 K. No change in resistance was observed after changing V_G since the IL was frozen and the charge carriers were "locked" in the channel by frozen ions. Next, the device was slowly warmed up at 1 K/min, and *R-T* was monitored (Figure A4.4a). A sharp increase in resistance was observed at ~215 K, suggesting that the

IL ions became mobile (i.e., the IL melted) and the charge density in the channel was significantly reduced (Figure A4.4a).

An additional *R-T* curve was also obtained by fast quenching across the freezing point followed by slow cooling (Figure A4.4b). After collecting *R-T* data at cooling rates of 1 K/min (line A) and 10 K/min (line B), we quenched the device from 240 K to 200 K at 10 K/min, and then changed the cooling rate to 1 K/min (line C). Clearly, line B and line C overlap, demonstrating that changing the cooling rate does not make a difference when the ions in the IL are no longer mobile.

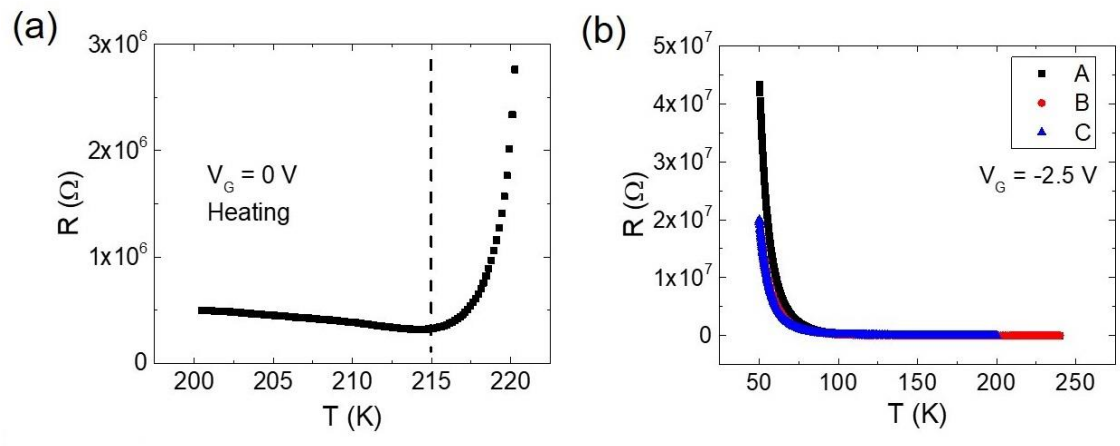

Figure A4.4 (a) *R-T* data taken during heating (1 K/min) after changing V_G from -2.5 V to 0 V at 200 K. An increase in resistance upon heating across ~215 K represents the melting of IL. (b) *R-T* data of the same device taken at different cooling conditions: 1 K/min from 240 K to 50 K (A), 10 K/min from 240 K to 50 K (B), 10 K/min from 240 K to 200 K and then 1 K/min to 50 K (C). Line B and line C match very well.

*A4.5 Changing the cooling rate across T**

First, *R-T* data at 1 K/min and 10 K/min were collected and the ratio R_{slow}/R_{fast} was plotted as a function of *T* (Figure 8.4 in the main article). Based on such data, the

temperature T^* is defined. The following measurements were then performed at $T \leq 200$ K, i.e., with the IL in the solid state. The device was first quenched from 200 K to a desired temperature (180 K, 120 K, or 70 K) at 10 K/min, and then the cooling rate was changed to 1 K/min while the *R-T* relationship was recorded (Figure A4.5). The 3 curves in Figure A4.5 overlap with each other, indicating that, once cooled below the IL freezing point, cooling rate across T^* has little influence on *R-T*.

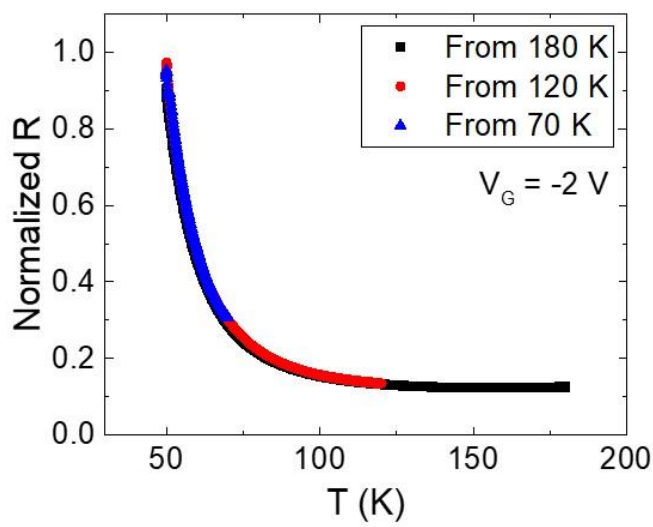

Figure A4.5 Slow-cooling resistance normalized by R_{fast} (50 K) for the same device in Figure 8.4 after quenching from 200 K to different start temperatures: 180 K, 120 K, and 70 K. The 3 curves overlap very well.